Dissociation Dynamics of Molecules Subject to Intense Ultrashort Laser Pulses

A THESIS

submitted by

ARNAB SEN

for the award of the degree

of

DOCTOR OF PHILOSOPHY

DEPARTMENT OF PHYSICS
INDIAN INSTITUTE OF SCIENCE EDUCATION AND RESEARCH - PUNE

November 2021

QUOTATIONS

Imagination is more important than knowledge. For knowledge is limited, whereas imagination embraces the entire world, stimulating progress, giving birth to evolution.

ALBERT EINSTEIN

DEDICATION

To my mother and the memory of my father

DECLARATION

I, **Arnab Sen**, declare that this written submission entitled **Dissociation Dynamics of Molecules Subject to Intense Ultrashort Laser Pulses** represents my idea in my own words and where others' ideas have been included; I have adequately cited and referenced the original sources. I also declare that I have adhered to all principles of academic honesty and integrity and have not misrepresented or fabricated or falsified any idea/data/fact/source in my submission. I understand that violation of the above will be cause for disciplinary action by the Institute and can also evoke penal action from the sources which have thus not been properly cited or from whom proper permission has not been taken when needed. The work reported in this thesis is the original work done by me under the guidance of Prof. Bhas Bapat and Dr. Vandana Sharma (IIT-Hyderabad).

Place: Pune

Date: November 2021

Arnab Sen

Dept. of Physics
IISER Pune, 411008

THESIS CERTIFICATE

This is to certify that the thesis titled **Dissociation Dynamics of Molecules Subject to Intense Ultrashort Laser Pulses**, submitted by **Arnab Sen**, to the Indian Institute of Science Education and Research Pune, for the award of the degree of **Doctor of Philosophy**, is a bona fide record of the research work done by him under our supervision. The contents of this thesis, in full or in parts, have not been submitted to any other Institute or University for the award of any degree or diploma.

02-11-2021

Place: Pune

Date: November 2021

Prof. Bhas Bapat
Thesis Supervisor
Professor
Dept. of Physics
IISER Pune, 411008

Dr. Vandana Sharma
Thesis Co-Supervisor
Associate Professor
Dept. of Physics
IIT Hyderabad, 502285

ACKNOWLEDGEMENTS

In this span of twenty-seven years of my life, I have come to meet many people. The moments spent with each one of them may not be great but each of them has helped me to grow as a person up to this point. I hereby want to thank them all for sharing moments with me. However, a few of them definitely needs a special mention.

I want to thank my school teacher Shibaji Chakrabarty, private tutor Swapan Roy and Asit Pahari for motivating me to do research in physics. In my B.Sc. days, the guidance from Prof. Rajshekhar Bhattyachrya and Prof. Partha Ghosh was invaluable and I am grateful to them for their support.

During the course of this Ph.D. program, I got a chance to work under the supervision of Prof. Bhas Bapat. I would like to express my heartful gratitude to him for his guidance and support. I had spent many times discussing with him, which motivated me to do better physics every day. I sincerely thank him for his neverending support and encouragement. I am also grateful to him for allowing me to carry out research work independently.

I am deeply thankful to Dr. Vandana Sharma for allowing me to work in her lab for more than three years. I had a great research experience there and it gave me enough confidence to do an experiment independently. I am also grateful to her for her valuable advice and help during the course of my Ph.D.

I would also like to thank Prof. M. Krishnamurthy for allowing me to stay in TIFR-Hyderabad, and allowed me to use his lab freely for almost three years. His critical reviews helped me to improve my scientific mind. I had cherished all the discussions with him, which increased my understanding and motivated me to do better.

I would like to express my deepest gratitude to Dr. Ram Gopal. This thesis would

have remained unfinished without his immense support and guidance. He taught me every single thing in the lab. His support during the experiment was very crucial and without him, my learning would have remained incomplete. I had spent a great time discussing physics with him.

My friends from different part of my life have helped to come out from darkest times and they showed me rays of light in the darkest hours. I am deeply thankful to Arnab, Sourav, Sandip for their supports. My friends from TIFR-Hyderabad, SouvikDa, SanketDa, AnganaDi, BhanuDa, Debobarata, Vineeth, Abhisek, Gourav, Ratul, and Sonali had shared my frustrations and joys. I had enjoyed our weekend outings the most. I will always cherish the moments spent with them. I am also thankful to my friends from IISER, Rajesh, Projjwal, Shuvendu, BaniDa, AnweshiDa, SuddhoDa, Arijeet, Sumit, and Deepak for sharing many precious moments and providing me a homely atmosphere. I will always remember our evening walks on the campus with Rajesh, AnweshiDa, Arijeet, and SuddhoDa. I would also like to thank AnweshiDa and Arijeet for making weekend nights musical with the songs of Rabindranath Tagore. Lastly, I would also thank Sunandita for her support and for holding my hand in my deepest sorrow.

However, the story remains incomplete without the support of my parents. Their blessings and love will always remain as lifelines to get out from all the hardships. I would like to express my heartful gratitude to my mother for her love and support after the loss of my father.

ABSTRACT

The probing time for sampling the internal dynamics of a molecular system should be comparable to the time-scale associated with the internal motion in a molecule, which ranges from femtoseconds (fs) to picoseconds (ps). Recent development in laser technology make it possible to probe a molecular system with intense and ultrashort laser pulses with large bandwidth.

In the presence of intense ($\sim$ 10-100 TW/cm^2) and ultrashort ($\sim$25 fs) laser field a molecule may go through ionization and eventually dissociates into various ionic and neutral fragments. Several transient electronic processes plays an key role in the molecular dissociation dynamics in the presence of intense, ultrashort laser field. One of the possible ways to understand the dissociation dynamics of the molecular system through various complex electronic processes is by capturing the velocity spread and the angular distribution of the ionic fragments with respect to the polarization axis of the laser field.

The main objective of this work is to understand the influence of the electronic processes in the dissociation dynamics. Two different aspects of the electronic processes have been addressed here by using a Velocity Map Imaging (VMI) technique along with detailed quantum chemistry calculations.

TABLE OF CONTENTS

Page

ACKNOWLEDGEMENTS i

ABSTRACT iii

LIST OF TABLES vii

LIST OF FIGURES xiii

CHAPTER 1: INTRODUCTION 1

1.1 Probing Molecular Systems 1

1.2 Laser-Molecule Interaction 2

1.3 Development of Ion Imaging Techniques 5

1.4 Focus of This Thesis 6

CHAPTER 2: MOLECULES IN EXTERNAL LASER FIELDS 8

2.1 Molecular Structure 8

2.1.1 The Born-Oppenheimer Approximation: For Diatomic Molecules 8

2.1.2 Vibrational and Rotational Dynamics of Diatomic Molecules 12

2.1.3 Electronic Structure of Diatomic Molecules 15

2.2 Ionization of Molecules in Intense Laser Field 20

2.2.1 Keldysh Parameter 20

2.2.2 Multi-photon Ionization 22

2.2.3 Tunneling Ionization 25

2.3 Dissociation in Intense Laser Field 30

2.3.1 Floquet Picture 31

2.3.2 Bond Softening and Bond Hardening 35

2.4 Laser Induced Rotational Dynamics 36

2.5 Experimental Strategy 38

Table of Contents (continued) **Page**

2.6 Summary 40

CHAPTER 3: EXPERIMENTAL DETAILS: VELOCITY MAP ION IMAGING TECHNIQUE 41

3.1 Overview of the Ion Imaging Technique 41

3.2 Velocity Map Ion Imaging Techinque 43

3.2.1 Electrostatic Lensing 43

3.2.2 Detection Technique 48

3.2.3 Conversion Methods 55

3.2.4 Calibration Technique 58

3.3 Summary 62

CHAPTER 4: HINDERED ALIGNMENT IN ULTRASHORT, INTENSE LASER-INDUCED FRAGMENTATION OF O_2^+ MOLECULAR ION . . . 64

4.1 Introduction 64

4.2 Experimental Details 66

4.3 Identification of Fragmentation Pathways 67

4.4 Effect of Peak Intensity Variation of The Laser Pulse 74

4.4.1 For 800 nm 74

4.4.2 For 400 nm 76

4.5 Post Ionization Alignment 76

4.6 Polarizability Calculation 81

4.7 Rotation and alignment of the transient molecular ion 88

4.8 Discussion 90

4.9 Summary 93

CHAPTER 5: DISSOCIATION DYNAMICS OF CH_3I IN INTENSE ULTRASHORT LASER FIELDS 95

5.1 Introduction 95

5.2 Experimental Details 97

5.3 Time-of-Flight Spectrum 99

5.4 Identification of Fragmentation Pathways 103

5.5 Time-Evolution of The Intermediate States 114
5.5.1 Photon Induced Orbital Coupling 114
5.5.2 Classical Model 115
5.6 Discussion 119
5.7 Summary 123
CHAPTER 6: SUMMARY AND FUTURE OUTLOOK. 124
6.1 Summary of The Present Work 124
6.2 Future Outlook 127
LIST OF PUBLICATIONS. 144

LIST OF TABLES

Table	Title	Page
3.1	The typical performace and the characteristic of a $\sim$ 40 mm MCP detector is listed here.	49
3.2	The schematic of the event list storing the time and position information of detected ion species arising from each event.	53
4.1	Dipole selection rules with few simple examples	69
5.1	The possible dissociation pathways and the corresponding values of the peak KE obtained from the fits, and the Kinetic Energy Release (KER), defined as the sum of energy of the fragments. Our data is compared with that from previous studies by Zhang *et al.*(110) and Liu *et al.*(111)	107

LIST OF FIGURES

Figure	Title	Page
2.1	The schematic diagram of a diatomic molecule AB is shown with the associated coordinate system. The nuclei A and B are at $\overrightarrow{R}_A$ and $\vec{R}_B$ with respect to the center of mass O. The position vectors of the electrons are highlighted as $\vec{r}_1, \vec{r}_2, \vec{r}_3$ in the center of mass frame.	9
2.2	The general form of the potential of a stable bound electronic state of a diatomic molecule	11
2.3	Vibrational levels of a diatomic molecule. The red dashed line shows the parabolic approximation with respect to the equilibrium internuclear separation.	14
2.4	A schematic representation of the coordinate system for hydrogen molecular ion H_2^+.	16
2.5	The potential energy curves of the H_2^+ molecular ion obtained by using the simple trial LCAO-MO wavefunctions for variational method . .	18
2.6	The electronic configuration of O_2 along with the orbital structures .	19
2.7	Schematic 1-D diagram showing the distorted atomic potential in the presence of an electric field for three different ionization mechanisms (a) multi-photon ionization, (b) tunneling ionization and (c) over-the-barrier ionization. The blue curves shows the field free atomic potential and the dashed curves represents the distorted potential in the presence of the external electric field with the red solid line showing the potential due to the laser field	21
2.8	(a)The potential energy curves ('*diabatic*' curves) of photon dressed $1\sigma_g$ and $1\sigma_u$ states are shown. The rectangles marked with X_1, X_2 and X_3 highlight the curve crossings. Based on dipole selection rule only X_2 and X_3 crossings are feasible. The horizontal lines depicts the field free vibrational energy levels. (b) The photon dressed '*diabatic*' and '*adiabatic*' curves for field strength $F_0 = 0.01$ a.u. are shown. . . .	33

3.1 (a)Two dissociation events and the associated pair of ionic fragments A^{p+} and B^{q+} are shown in velocity space. (b) Adding up a large number of events a spherical surface pattern is observed, which is known as *Newton sphere*. The *Newton sphere* of B^{q+} is shown here and it represents a typical $\cos^2\theta$ distribution with respect to the polarization axis. 42

3.2 The schematic of various ion-imaging configurations (a) single acceleration configuration, (b) Willy-McLaren configuration, (c) velocity map configuration and (d) velocity map configuration with einzel lens using several electrodes: Repeller (R), Extractor (E) and Ground (G) are shown. Most spectrometers have a field free drift region after G electrode but is not shown here. 43

3.3 Simulated ion trajectories of charged particles with initial velocity components $(0, \pm v_y, \pm v_z)$ for the velocity map configuration shows the ion focusing on the planar detector. 46

3.4 Simultated ion trajectorices of charged particles with initial velocity components $(0, \pm v_y, \pm v_z)$ for the velocity map configuration for a wide source about (a) ~ 4 mm along y-axis and (b) ~ 0.4 mm along z-axis. Under this biasing condition of 645 V/478 V ions are mapped within ± 0.05 mm and ± 0.025 mm due to vertical spread of ~ 4 mm and horizontal spread of ~ 0.4 mm respectively. 47

3.5 (a) and (b): Schematic representation of secondary electron formation inside a micro-channel and through a stacked MCP. (c) Encoding the position of ion hit (red dot) using a delay line anode system. (d) Actual MCP+DLD detector system. 50

3.6 The complete data acquisition scheme. 52

3.7 Schematic of the experimental set up used to study photo-induced molecular fragmentation processes using velocity map imaging technique. 54

3.8 The time of flight and postion spectrum of the fragmented I^+ ions are shown in (a) and (c) respectively. The time window to obatin the central slice of the *Newton spheres* is highlighted with red solid lines. Similarly CH_3^+ ions are shown in (b) and (d) respectively. 56

3.9 Time sliced velocity map images of (a) I^+ and (b) CH_3^+ 57

3.10 Plot of the radius of the impacting ions on the detector as a function of the energy fitted using a third order quadratic function. (a) for $V_E, V_R \approx 478$ V, 645 V with coefficients $a = 0.00309$, $b = 0.00547$ and $c = 7.62337E-5$. (b) for $V_E, V_R \approx 2250$ V, 3000 V with coefficients $a = 0.01004$, $b = 0.02605$ and $c = 2.78529E-4$ for calibrating the images of I^+ and CH_3^+ fragments. 59

3.11 Coincidence map of CH_3^+ and I^+ ions arising from Coulomb explosion events. 60

3.12 The difference between the arrival times of the forward and backward emitted ions in the time of flight spectrum simulated for various initial energies of I^+ ions is calculated for two spectrometer configurations. The flight time difference for operation with lensing fields (ΔT_L) is compared against flight time difference for operation with a homogeneous, lensless fields (ΔT_{NL}). The estimated slope from the linear fitting is $\sim$ 0.9 61

3.13 The kinetic energy distribution of (a) I^+ and (b) CH_3^+ ions obtained from the time sliced velocity maps are shown in black. The kinetic energy distribution obtained from the time of flight spectrum of the ions arising in pairs from Coulomb expolsion are shown in red. 61

4.1 The time sliced velocity map of O^+ ions emerging from the dissociation of O_2^+ ions in the presence of moderately intense laser field of wavelength (a) 800 nm and (b) 400 nm. 68

4.2 Possible dissociation channels leading to higher kinetic energy relase via the (a) $X^2\Pi_g$ and (b) $a^4\Pi_u$ state in the presence of 800 nm pulses. 70

4.3 Possible dissociation pathway for the higher kinetic energy fragments through $a^4\Pi_u$ state in the presence of 400 nm, 35 fs pulses. 71

4.4 Possible dissociation pathways for low energy fragments through (a) $a^4\Pi_u$ and (b) $b^4\Sigma_g^-$ parent ion states in the presence of 800nm laser pulse. 72

4.5 Same as Figure-4.6 for 400nm laser pulse. 73

4.6 Time sliced velocity map images of O^+ ions in the plane of the laser polarization for 800 nm, 25 fs pulses at (a)$2I_0$, (b) $3I_0$, and (c) $4I_0$. The corresponding KER distribution, obtained by azimuthal integration over these images is plotted in the right panel. 75

4.7 Same as Figure-4.6, but for 400 nm, 35 fs pulses at (a) I_0, (b) $2I_0$, and (c) $3I_0$. 77

4.8 The angular distribution (w.r.t. the laser polarization axis) of the high energy ions 25 fs, 800 nm pulses of intensities at (a) $2I_0$, (b) $3I_0$, and (c) $4I_0$. The Black histograms are experimental data. The red dashed curve indicates the expected angular distributions based on MO-ADK theory. The vertical dashed line placed at the peak position of the angular distribution obtatined at $2I_0$ to highlight the shift in angular distribution with increasing peak intensity of the laser pulse. Same for 400 nm, 35 fs pulses at intensities (d) I_0, (e) $2I_0$, and (f) $3I_0$. 78

4.9 (a) Potential energy curves calculated using two different basis sets. Blue curves: Dunning and Hay type basis set. Red curves: correlation consistent triple valance zeta basis set. Black circles: obtained from work of Gilmore*et.al*(99). (b) Calculated dipole polarizability ($\alpha_{||}$) along the molecular axis using finite difference method with external field value $\pm$0.002a.u. using two different basis sets. Black dashed line: dipole polarizability ($\alpha_{||}$) calculated by M.A.Buldakov*et.al*(100). 84

4.10 (a) Potential energies for the O_2^+ molecular ion for doublet and quartet states using Dunning type and correlation consistent augmented triple zeta valance type basis set. The zero of the energy axis is taken as the $v = 0$ level of the $X^2\Pi_g$ ground state of O_2^+ ion. (b) Same potential energy curves in the presence of electric field $F = 0.002$ a.u. along the molecular axis. 84

4.11 Calculated polarizabilities ($\alpha_\perp$ and $\alpha_{||}$) of the (a) $a^4\Pi_u$ and (b) $1^4\Sigma_g{}^+$ states which participate in the proposed dissociative ionization pathway. 85

4.12 Dominant electronic configuration diagram of $1^4\Sigma_g$ state. 86

4.13 (a) The change in squared configuration interaction coefficient for the bonding and anti-bonding configuration at external electric field $F =$ 0.002 a.u. (b) Potential energy curve of $1^4\Sigma_g$ state in the presence and absence of the electric field applied parallel to the molecular axis. . 87

4.14 Schematic of the dissociation of O_2^+. In the presence of 25 fs 800 nm pulses, the value of $\alpha_{||}$ for the $a^4\pi_u$ state (brown curve) is positive, resulting in a strong aligning torque. The shaded areas denote the cycle-averaged, quasi-static field of the laser pulse. When the ion makes a transition to the negative polarizability state (green curve) at $R \sim$ 3.2 a.u. ($t \sim 13$ fs), the torque due to the weak trailing pulse (blue shaded) is insufficient to counter the alignment. 89

4.15 For 35 fs 400 nm laser pulses, the molecular ion created in the $a^4\Pi_u$ state crosses over to the $1^4\Sigma_g$ dressed state, which has a negative value of $\alpha_{||}$. The ion crosses over to the state with $\alpha_{||} < 0$ earlier in time ($t \sim 7$ fs or at $R = 2.8$ a.u.). There is sufficient remnant laser intensity (blue shaded region) at this time, which coupled with the negative polarisability, will hinder the alignment. 90

4.16 The angular distribution (w.r.t. the laser polarization axis) of the high energy ions is shown for (a) $2I_0$, (b) $3I_0$ and (c) $4I_0$. Black histograms are experimental data. The blue solid curve is from our model that includes molecular tunneling and torque due to the laser. The same for 35 fs, 400 nm pulses of intensities (d) I_0 (e) $2I_0$ and (f)$3I_0$. 91

5.1 The time of flight spectrum at a pulse duration of ∼25 fs with peak intensity 5×10^{12} W/cm^2 with the main fragments highlighted and their peaks shown in an expanded form. 100

5.2 Same as Figure-5.1 at a pulse duration of ∼1500 fs with peak intensity 5×10^{12} W/cm^2 100

5.3 Coincidence plot of the CH_n^+ ions and I^+ ions for (a) ∼ 25fs and (b) ∼ 1500fs 102

5.4 (top) The measured absolute yields of the parent molecular ion CH_3I^+, CH_n^+, I^+ and I^{2+} ions, derived from the area under the corresponding peaks. (bottom) The absolute yields of CH_n^+ ions coming in coincidence with I^+ (bottom) with the increasing pulse duration obtained by summing the counts in the islands in photoion-photoion coincidence. 103

5.5 A two-dimensional contour map of the ion time-of-flight spectrum (normalized with respect to the total counts) as a function of grating position offset. The offset is with respect to grating position for the shortest laser pulses. Negative offsets introduce negative chirps into the laser pulse and vice-versa. 104

5.6 Velocity Map Images of (a) CH_3^+ and (b) I^+ ions at the shortest pulse duration. The color scale for ion counts is logarithmic. The laser polarization axis (red arrow) is vertical. Semicircles identify different dissociation and CE channels. 104

5.7 The kinetic energy distribution (black histogram) of (a) CH_3^+ with multiple Gaussian fits (dashed blue and solid red curves) shown for a peak intensity of ∼ 5 TW/cm^2 with pulse duration ∼25 fs. The same for I^+ ions is shown in (b) 105

5.8 (a) The Velocity Map Images of I^{2+} ions at pulse duration ∼ 150 fs with peak intensity ∼ 5 TW/cm^2 and the corresponding kinetic energy distribution (b) (black histogram) with multiple Gaussian fits are shown in dashed blue and solid red curves. 108

5.9 Time sliced velocity map images of [left panel] CH_3^+ and [right panel] I^+ ions recorded at different laser pulse durations. 109

5.10 The kinetic energy distribution of [left panel] CH_3^+ and [right panel] I^+ ions obtained at different pulse durations from the associated time sliced velocity map images. The dashed vertical lines are placed to highlight the peak shift with increasing pulse-duration. 110

5.11 The normalized KE distribution of the de-hydrogenated ions (a) CH_3^+, (b) CH_2^+, (c) CH^+, (d) C^+ with respect to the total CH_n^+ counts coming in coincidence with the I^+ observed for the longest pulse duration in the photoion-photoion coincidence plot. The corresponding mean values of the distribution are highlighted in the plots with a dashed vertical line. 112

5.12 Time sliced velocity map images of [left panel] I^{2+} and [right panel] the kinetic energy distribution associated with time sliced velocity map images recorded at different laser pulse durations. The dashed vertical line is placed to highlight the peak shift with increasing pulse-duration. 113

5.13 The energy of the HOMO $2e$ and HOMO-1 $3a_1$ orbitals of the mono-cationic Methyl Iodide obtained from MCSCF calculation. The orbital structres of $2e$ and $3a_1$ orbitals are shown in the right panel. 115

5.14 (a) and (b) show a schematic of the dissociative wavepacket dynamics over $\widetilde{A}$-state along the C-I axis. In the case shown on the left, the short pulse prevents any coupling at later times, while in the case shown on the right, the extended pulse permits one photon orbital coupling at 3.9Å. 116

5.15 The relative yield of de-hydrogenated methyl ionic fragments (a) CH_3^+, (b) CH_2^+, (c) CH^+, (d) C^+ in coincidence with the I^+ ions with respect to the total ion yield as a function of pulse duration. The calculated ionization probability as a function of pulse duration, based on a semi-classical model accounting for enhanced ionization due to a resonant coupling at an inter-nuclear separation of $\sim$3.9 Å, is shown as a red solid line. The shaded region shows the range of values of the ionization probability corresponding to different single ionization instants within $\pm$ 10% of the laser peak. 117

5.16 The relative yield of the total I^+ and CH_n^+ ionic fragments with respect to the total ion yield as a function of pulse duration. The calculated ionization probability as a function of pulse duration, based on a semi-classical model accounting for enhanced ionization due photo induced multi-orbital coupling is shown as a red solid line. The shaded region shows the range of values of the ionization probability corresponding to different single ionization instants within $\pm$ 10% of the laser peak. 118

CHAPTER 1

INTRODUCTION

1.1 Probing Molecular Systems

The smallest chemical unit of matter is a molecule, which defines the chemical properties of matter. A molecule consists of atoms held together due to chemical bonds by electron sharing between the closely spaced atoms to form a molecule.

The length scale associated with the atom is quite small as compared to the world seen by the naked eye. The size of atoms is roughly in the order of $\sim$ 1 angstrom (Å), which is one ten-billionth of a meter. The dimension of the molecules usually ranges from few angstroms to tens of angstroms. The simplest molecules, formed by two atoms either with similar chemical properties to form a homo-nuclear diatomic molecule or with atoms of different characteristics to form a hetero-nuclear diatomic molecule.

Atoms in a molecule are not stationary and they exhibit various dynamics under external perturbation. The diatomic molecule has six degrees of freedom associated with translational, vibrational, and rotational motion. The time-scale associated with vibrational, and rotational motion ranges between femtosecond (fs) to picosecond (ps) regime, which is roughly one-millionth of one billionth, of a second. The internal dynamics of the molecule get complicated for bigger molecules due to their complex geometric structure. Such internal dynamics play an important role in many chemical reactions like structural rearrangement, which is very common in large organic molecules. The first rearrangement reaction was observed in bis(triphenylmethyl)peroxide-1 to the tetraphenylethane-2(1).

In general, the motion of the nuclei is much slower than the electrons due to the huge mass difference (The ratio of the electronic mass to the nuclear mass lies between $\sim 10^{-3}$-10^{-5}) and hence the nuclear and electronic motions are usually decoupled.

However, during the dissociation or dissociative ionization processes, the electronic and vibrational degrees of freedom are coupled and it has a strong influence on the fragmentation dynamics of the molecules which happens on an ultrashort time scale.

The challenge is to get a suitable probe or the perturbation that allows us to sample such ultrafast processes to understand ultrafast electronic processes happening during dissociation. The probe needs to be shorter than the vibrational and rotational time scale of the molecular system, i.e. of the order of fs to ps regime. In recent times the advancement in the generation of ultrashort laser pulses(2) with a broad bandwidth allowed scientists to investigate the molecular dynamics happening in the fs to ps time scales(3; 4). The interaction of molecules with intense ultrashort laser pulse opens up a fascinating area of research. We, therefore, look into some basic aspects of the basic laser-molecule interaction mechanism at the beginning of the thesis.

1.2 Laser-Molecule Interaction

The interaction of light with the matter was an area of interest to many scientists during the late 19th century. The effect of the interaction of light with electrolytic cells was one of the pioneering experiments in this area of research performed by Alexandre Edmond Becquerel in 1839. In later years several great minds were involved in various experiments to study the electron emission from matter in the presence of electromagnetic radiation. The classical electromagnetic theory suggested the intensity of electromagnetic radiation defines the energy of the emitted electrons from the matter. However, the experiments performed by Lenard in 1902 indicated that the energy of the emitted electrons depends upon the frequency of the light. In 1900, Max Planck concluded from the experiments on black-body radiation that the electromagnetic wave carries energy in discrete energy packets(5). Albert Einstein took this idea to next level and proposed, the energy carried by each packet is proportional to the frequency of the light to explain the data observed from the photoelectric effect by Lenard(6). Each packet carries '$h\nu$' amount of energy, where ν is the frequency of the electromagnetic radiation and h is known as Planck constant. A single-photon with a certain threshold frequency can eject

an electron from the surface of a metal and the maximum kinetic energy, taken away by the electron is

$$KE_{max} = h\nu - W$$

where W is the work function of the metal, which defines the minimum energy needed to eject an electron from the metal surface. The threshold frequency required to initiate the photoelectric effect can be determined from the above equation, and it can be expressed in a mathematical form as $\nu_0 = W/h$.

Classically, for the plane wave, the average intensity of the laser pulse is proportional to the amplitude squared of the oscillating electric field. Einstein's model of the photoelectric effect is valid under the 'weak field' approximation, where the electric field associated with the incident light intensity remains very low compared to the Coulomb field within atoms or molecules. For modern lasers which deliver intense ($\sim$ 10^{12} - 10^{15} W/cm^2) ultrashort pulses indicate a high photon flux and the associated electric field becomes comparable to the Coulomb field within atoms or molecules. Under this strong external perturbation various new phenomena, such as the multiphoton(7), tunnel(8), and over the barrier ionization(9) kick in. The ionized molecules go through complex dynamical processes. The coupled response of the electronic and the nuclear dynamics lead to several complex phenomena (10; 11) and has been observed even for the simplest molecular system like H_2^+/D_2^+. The dissociation dynamics of the simplest molecule is well understood after the several years of hard work both in the theoretical and experimental department. In recent times, scientists have tried to understand the complex dynamical behaviour for multi-electronic systems based on the previous understanding of the simplest molecular system.

Now the question is how one can track the transient electronic processes during the dissociation of the molecule? Multi-electron dissociative ionization of a molecule in the presence of energetic photons can be written in the following manner:

$$AB + h\nu \longrightarrow AB^{n+} + n.e^- \longrightarrow A^{p+} + B^{q+}$$

where the sample molecule AB, interacts with a single photon $h\nu$ of the laser pulse

and forms AB^{n+} by removing n electrons after the ionization. The newly formed molecular ion AB^{n+} eventually dissociates into several ionic fragments. To understand the involved mechanisms in the laser-molecule interaction, the products of the reaction and their kinematic properties, and the probabilities of different outcomes are needed to be measured. In the following section, different experimental techniques are discussed thoroughly.

In absorption spectroscopy(12; 13), the optical absorption of the laser pulse is measured as a function of the wavelength after the laser-molecule interaction. However, this technique is limited to study the bound electronic states of the molecule. The transient absorption spectroscopy(14; 15) is next-generation absorption spectroscopy, where the absorbance of a certain wavelength is detected as a function of time to study the dynamic behaviour of the molecule going through dissociation. In a proper experiment, one of the laser pulses is used to excite the molecular system, and another pulse is used to measure the absorbance of the system after a time delay and the time delay is varied over a certain range to get the absorbance as a function of time in a fs to ps regime. This information provides time-resolved relaxation dynamics of the excited states of the molecules.

The other possible way to understand the photon-induced ionization and dissociation dynamics of the molecules is by detecting the ejected electrons or the dissociated ions as they carry significant information of the participating electronic states in the dissociation. Over the recent years, with advances in the charged particle optics and detection technology several new experimental techniques have emerged. Photoelectron spectroscopy with femtosecond time resolution based on the electron detection mechanism can identify the very short-lived electronic states(16; 17). Another very fascinating way to understand the change in the molecular structure is by the laser-induced electron diffraction method(18; 19; 20). In this technique, loosely bound electrons in the molecule rescatter from the molecular core in the presence of the laser field and eventually forms an interference pattern, which carries the information about the structural dynamics of the molecule. Similarly, the detection of the ionic fragments can help to understand the dissociation dynamics of the molecules(21; 22; 23; 24; 25; 26; 27). The

development of the ion imaging technique(28; 29; 30; 31) plays the key role to decipher the correlation between the transient electronic processes and the dissociation dynamics in the presence of intense laser field is the primary theme of this thesis.

1.3 Development of Ion Imaging Techniques

What kind of information is required from the ion detection method to understand the fragmentation dynamics of the molecules? First is the kinetic energy distribution of the fragmented ions, which is directly associated with the internal energy of the transient states of molecule. With a guiding electric field and a charged particle detector(28; 29) with a proper signal processing unit(30; 31), the time of flight of the ionic fragments can be obtained with respect to a start signal taken from the photodiode signal of the laser pulse for a single event. From the temporal distribution of the ionic fragments, the kinetic energy can be estimated. To get a better energy resolution a small aperture is placed before the ion detector to detect ionic fragments ejected along the time of flight axis, which in principle allows only one momentum component with respect to the polarization axis. The angular dependence of the fragmentation dynamics with respect to the polarization axis can also be mapped by changing the direction of the polarization axis of the laser pulse with respect to the time of flight axis. For simultaneous detection of all the momentum components the position of the ion splat on the detector is required. The rapid development of the various kind of position-sensitive detectors such as charged coupled device camera (CCD)(32), wedge and strip detector (WSD)(33), and delay line anode detector (DLD)(28; 29) make the detection of three momentum component (p_x, p_y, p_z) of the fragmented ions possible. This advancement in ion detection opens up a new direction, Momentum spectroscopy, which was first introduced in ion-atom collisions in 1992 by Ali *et. al*(24).

Along with the kinetic energy distribution, the angular information is also required mostly for the photon-induced dissociation processes, as it provides valuable information about the orbital structure and the transition dipole moment associated with the participating electronic states during fragmentation. After development of the Momentum

spectroscopy(24; 25; 26), the estimation of the angular direction of each ionic fragment with respect to the polarization axis of the laser pulse becomes a lot easier. The simultaneous detection of kinetic energy and the angular distribution of the ionic fragments are most desirable and that is possible through the ion imaging technique. In contrast to the Momentum spectroscopy, the ion imaging technique gives the complete information (kinetic energy and angular distribution) only from the position spectrum obtained in the 2D position-sensitive detector. Complete 3D information can be retraced using several conversion methods. In the past 30 years, ion imaging methods has developed rapidly in several aspects. Velocity Map Imaging (VMI) is the most developed variant of the ion imaging method introduced by David Chandler and Paul Houston in 1987(34). This primitive model of VMI spectrometer has been further modified by André T. J. B. Eppink and David H. Parker(23; 35). The specialty of the VMI is with the help of electrostatic lensing all the ionic fragments with the same initial velocity vectors are mapped onto the same point on the position-sensitive detector. Using this special kind of ion imaging spectrometer we have obtained insights into the dissociation dynamics of small polyatomic molecules under the intense ultrashort laser field.

1.4 Focus of This Thesis

In the presence of intense ($\sim 10^{12}$ - 10^{15} W/cm^2) and ultrashort ($\sim$25 fs) laser pulse the molecular system goes through an ionization process which can occur via different ionization mechanism such as multiphoton ionization, tunnel ionization, over the barrier ionization, electron rescattering or through enhanced ionization depending upon the intensity of the laser field. For NIR laser pulses in the intensity regime between $\sim$ 10^{12} - 10^{14} W/cm^2, multiphoton ionization and the tunnel ionization are most probable. In recent time several theoretical works associated with the photoionization mechanism of the molecule are properly developed for simple molecular systems. Most of the theories(36; 37; 38) suggest the ionization probability of the molecule depends upon two factors, firstly, the alignment of the molecule with respect to the laser polarization axis, and secondly, the symmetry of the highest occupied molecular orbital (HOMO)

of the molecular system. After the ionization, the newly formed molecular ion usually dissociates into several ionic and neutral fragments. Molecules ionizing at the peak of the laser pulse can interact strongly with the trail of the laser pulse during dissociation, and it could lead to various electronic processes like charge redistribution(39; 40; 41), orbital rearrangement(42). Such transient electronic processes influence the dynamics of a molecule in the presence of the trailling part of the laser pulse. The redistribution of charges in the presence of the laser field purely depends upon the polarizability of the electronic state participating in the dissociation. It will induce a dipole moment over the molecular ion in the presence of the laser field, which affects the rotational dynamics of the molecular ion abruptly. Furthermore, during the dissociation, the molecular orbitals rearrange with increasing bond length causes partial charge localization over some specific nuclei in the presence of the laser field which could lead to sequential ionization.

In this thesis work, I have mainly focused on the various kind of molecular dynamics influenced by the transient electronic processes in the presence of the laser field. Using an indigenously developed Velocity Map Imaging spectrometer various aspect of the molecular dissociation dynamics showing the traces of the transient electronic processes has been studied for two different molecular systems.

The thesis has been organized in the following manner. After starting from the introductory chapter, in chapter 2 the physics of the molecular system and the details of the laser-molecule interaction has been discussed for better understanding. Chapter 3 presents the details of the experimental technique used for this specific study along with the data acquisition and calibration methods. Chapters 4 and 5 contain the experimental results observed for two different molecular systems. Finally, in chapter 6, I have summarised the entire work and highlighted the prospects.

CHAPTER 2

MOLECULES IN EXTERNAL LASER FIELDS

2.1 Molecular Structure

In this chapter, the basics of molecular structure and the physics of laser-molecule interaction will be discussed in detail. The general description of the molecular structure of diatomic molecules along with electronic and nuclear dynamics will lay the background for the laser-molecule interaction. This chapter will provide the physical insights to understand the experimental results shown in the following chapters.

2.1.1 The Born-Oppenheimer Approximation: For Diatomic Molecules

Let us consider a diatomic molecular system AB having nuclei A and B with masses m_A and m_B respectively. In the center of mass frame the position vector of the nuclei A and B are denoted as $\vec{R}_A$ and $\vec{R}_B$ respectively, so that internuclear separation will be written as $\vec{R} = \vec{R}_A - \vec{R}_B$. The position coordinates of the N electrons in this molecular system are represented as $\vec{r}_1$, $\vec{r}_2$, $\vec{r}_3$, ...,$\vec{r}_N$ in the center of mass frame of A and B. The time-independent Schrödinger equation of this molecular system can be written as :

$$[T+V]|\psi(\vec{R},\vec{r}_1,\vec{r}_2...,\vec{r}_N)\rangle = E|\psi(\vec{R},\vec{r}_1,\vec{r}_2...,\vec{r}_N)\rangle \tag{2.1}$$

where T is the total kinetic energy operator, and V is the total potential energy operator of the entire molecular system. This problem becomes much more complicated than the atomic system due to the presence of coupled nuclear and electronic motion. However, the coupled wavefunction could be decoupled by the use of separation of variables under some simple approximations. As the mass of the electrons are much smaller

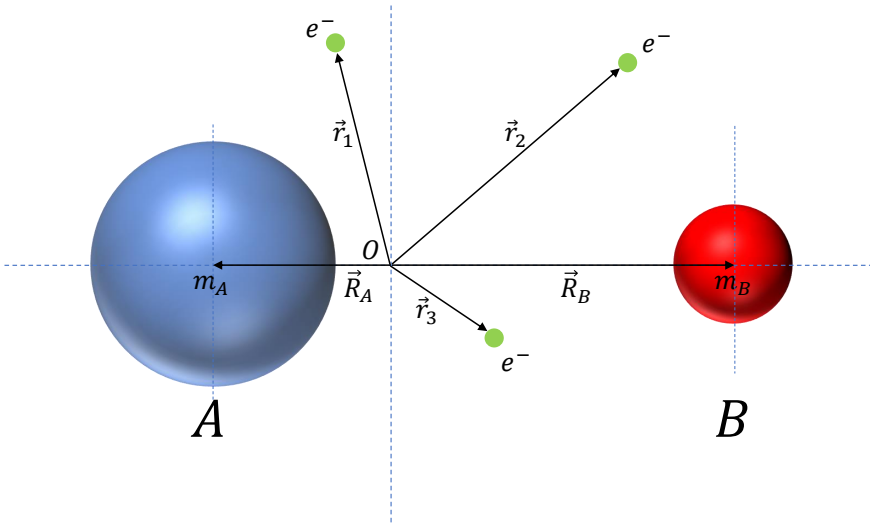

Fig. 2.1: The schematic diagram of a diatomic molecule AB is shown with the associated coordinate system. The nuclei A and B are at $\vec{R}_A$ and $\vec{R}_B$ with respect to the center of mass O. The position vectors of the electrons are highlighted as $\vec{r}_1, \vec{r}_2, \vec{r}_3$ in the center of mass frame.

than the nuclei in the molecular system (In general the ratio of the electronic mass to the nuclear mass lies between $\sim 10^{-3}$-10^{-5}), the motion of the nuclei is much slower than the electrons. Hence, one can assume the nuclei is stationary as compared with the electronic motion. Based on this assumption the coupled electronic wavefunction could be decoupled into electronic and nuclear part. This approximation is known as *Born-Oppenheimer approximation*(43; 44; 45). Hence, the total kinetic energy operator can be written as the sum of the kinetic energy operator associated with the nuclei $\hat{T}_N$ and the the kinetic energy operator for electrons $\hat{T}_e$, i.e,: $\hat{T} = \hat{T}_N + \hat{T}_e$. The $\hat{T}_N$ and $\hat{T}_e$ can be represented explicitly as

$$\hat{T}_N = -\frac{\hbar^2}{2\mu}\nabla_R^2 \tag{2.2}$$

and

$$\hat{T}_e = -\sum_{i=1}^{N}\frac{\hbar^2}{2m_e}\nabla_{r_i}^2 \tag{2.3}$$

where the μ is the reduced mass of A and B:

$$\mu = \frac{m_A m_B}{m_A + m_B}. \tag{2.4}$$

The potential energy of the system can be written as the sum of the three Coulombic interactions: a) interaction between the two nuclei with electronic charges $Z_A e$ and $Z_B e$, b) interaction between the electrons and the nuclei, and c) electron-electron interaction.

$$V(\vec{R}, \vec{r}_1, \vec{r}_2 ..., \vec{r}_N) = V_{N-N}(\vec{R}) + V_{N-e}(\vec{R}, \vec{r}_1, \vec{r}_2 ... \vec{r}_N) + V_{e-e}(\vec{r}_1, \vec{r}_2 ... \vec{r}_N) \tag{2.5}$$

where,

$$V_{N-N}(\vec{R}) = \frac{Z_A Z_B e^2}{|\vec{R}|} \tag{2.6}$$

$$V_{N-e}(\vec{R}, \vec{r}_i) = -\sum_{i=1}^{N} \frac{Z_A e^2}{|\vec{r}_i - \vec{R_A}|} - \sum_{i=1}^{N} \frac{Z_B e^2}{|\vec{r}_i - \vec{R_B}|} \tag{2.7}$$

$$V_{e-e}(\vec{r}_i) = \frac{1}{2} \times \sum_{i \neq j}^{N} \frac{e^2}{|\vec{r}_i - \vec{r}_j|} \tag{2.8}$$

The time independent Schrödinger equation for the electrons assuming stationary nuclei with the internuclear separation $\overrightarrow{R}$ can be expressed as :

$$[\hat{T}_e + \hat{V}] |\phi_k(\vec{R}, \vec{r}_1, \vec{r}_2 ..., \vec{r}_N)\rangle = E_k(\vec{R}) |\phi_k(\vec{R}, \vec{r}_1, \vec{r}_2 ..., \vec{r}_N)\rangle \tag{2.9}$$

This equation is known as the *electronic wave equation*. The eigenfunctions ϕ_k and the eigenvalues E_k in the above equation has a parametric dependence on the internuclear separation R, which is assumed to be fixed during the calculations. The electronic eigenfunctions ϕ_k forms a complete basis set at each internuclear separation $\vec{R}$, i.e.

$$\langle \phi_l | \phi_k \rangle = \delta_{lk} \tag{2.10}$$

The eigenfunctions for the molecule can be written in the following manner due to the completeness of the electronic eigenfunction :

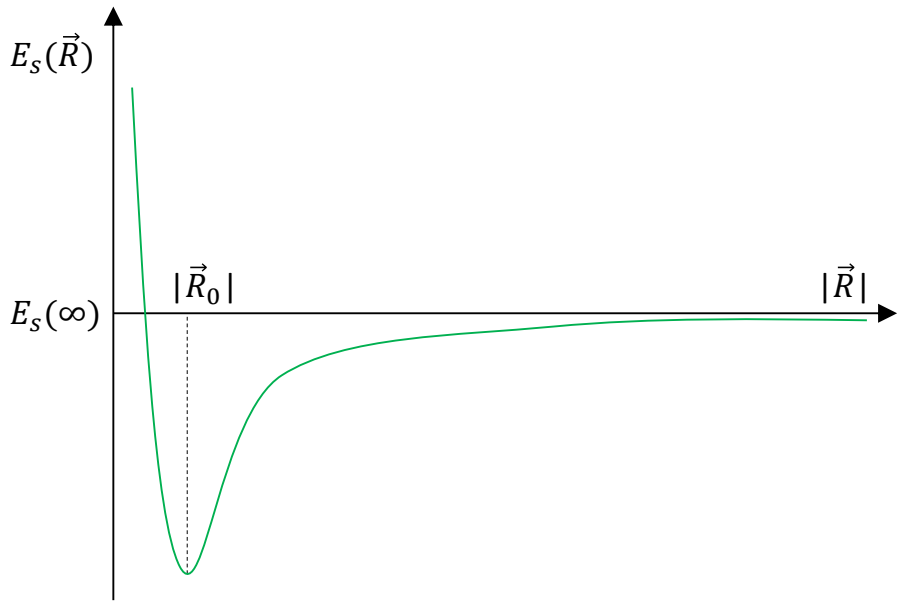

Fig. 2.2: The general form of the potential of a stable bound electronic state of a diatomic molecule

$$|\psi(\vec{R},\vec{r}_1,\overrightarrow{r}_2...,\vec{r}_N)\rangle = \sum F_k(\vec{R})|\phi_k(\vec{R},\vec{r}_1,\vec{r}_2...,\vec{r}_N)\rangle \tag{2.11}$$

The expansion coefficients $F_k(\vec{R})$ are the nuclear eigenfunction for the specific electronic state k. The *nuclear wave equation* can be determined by putting the molecular eigenfunction $|\psi(\vec{R},\vec{r}_1,\vec{r}_2...,\vec{r}_N)\rangle$ in the time-independent Schrödinger equation and projecting it over the $\langle\phi_s|$ basis. Using the orthonormality condition the new electron-nuclei coupled equation can be expressed as :

$$\sum \left[\langle\phi_s|[T_N]F_k(\vec{R})|\phi_k(\vec{R},\vec{r}_1,\vec{r}_2...,\vec{r}_N)\rangle\right] + \left[E_s(\vec{R}) - E\right]F_s(\vec{R}) = 0 \tag{2.12}$$

The operator $\hat{T}_N$ acts on $F_k\ (\vec{R})\ |\phi_k(\vec{R},\vec{r}_1,\vec{r}_2...,\vec{r}_N)\rangle$ and gives :

$$[\hat{T}_N]F_k(\vec{R})|\phi_k(\vec{R},\vec{r}_1,\vec{r}_2...,\vec{r}_N)\rangle = -\frac{\hbar^2}{2\mu}\left[F_k(\nabla_R^2\phi_k) + 2(\nabla_R F_k.\nabla_R\phi_k) + (\nabla_R^2 F_k)|\phi_k\rangle\right] \tag{2.13}$$

The variation of $|\nabla_R\phi_k|$ is significantly smaller than the $|\nabla_R F_k|$ as the electronic

eigenfunction varies slowly with respect to the nuclear coordinate system. The $|\nabla_R \phi_k|$ term can be neglected by using the *Born Oppenheimer approximation*. As a result of this, the abovementioned coupled equation can be written as in the following :

$$\left[-\frac{\hbar^2}{2\mu}\nabla_R^2 + E_s(\vec{R}) - E\right] F_s(\vec{R}) = 0 \tag{2.14}$$

The above equation is known as *uncoupled nuclear wave equation*, in which the $E_s(\vec{R})$ works as the potential.

For any electronic state the $E_s(\overrightarrow{R})$ is dominated by the Coulombic interaction between the two nuclei A and B as $\vec{R} \to 0$, however, at $\vec{R} \to \infty$, $E_s(\vec{R})$ tends to a constant value $E_s(\infty)$ which is the energy of the two isolated nuclei. For a stable bound electronic state $E_s(\vec{R})$ shows a minimum at some internuclear separation $(\vec{R}_0)$. Figure-2.2 represents the general form of the electronic potential of a stable bound electronic state of a diatomic molecular system.

2.1.2 Vibrational and Rotational Dynamics of Diatomic Molecules

Let us return to the *uncoupled nuclear wave equation*, which leads to vibrational and rotational motion of a diatomic molecular system. The function $F_s(\vec{R})$ depends upon the product of the radial and angular function which depends upon the polar angle Θ and Φ of the vector $\vec{R}$. The angular function is an eigenfunction of the total orbital angular momentum of the system $\vec{J}^2$ and the z-component of it J_z. The corresponding eigenfunction is represented with the spherical harmonic function $Y_{J,M_J}(\Theta,\Phi)$.

For a special condition with zero total orbital angular momentum the energy of the system does not depend upon M_J and hence the energy level shows $(2J+1)$-fold degeneracy. However, the energy of the system depends upon the *quantum number* J and a newly introduced *quantum number* v, which is associated with the vibrational motion of the diatomic molecular system. So, for s-th electronic state the nuclear eigenfunction $F_s(\vec{R})$ can be written as (45):

$$F_s(\vec{R}) = \frac{1}{R} F_{v,J}(\vec{R}) Y_{J,M_J}(\Theta,\Phi) \tag{2.15}$$

Substituting the above function into the *uncoupled nuclear wave equation*, we obtain a radial equation:

$$\left[-\frac{\hbar^2}{2\mu} \left(\frac{d^2}{dR^2} - \frac{J(J+1)}{R^2} \right) + E_s(\vec{R}) - E_{s,v,J} \right] F_{v,J}(\vec{R}) = 0 \tag{2.16}$$

For a stable bound electronic potential $E_s(\vec{R})$ the nuclear motion happens over a small region near the equilibrium position $(\vec{R}_0)$. The Taylor series expansion of the $E_s(\vec{R})$ about the minimum is required to solve the above equation analytically. On the other side $E_{s,v,J}$ can be approximated as the sum of the vibrational, rotational and electronic energy at the equilibrium internuclear separation, i.e.

$$E_{s,v,J} = E_v + E_J + E_s(\vec{R}_0) \tag{2.17}$$

The Taylor series expansion of $E_s(\vec{R})$ around $\vec{R}_0$ is :

$$E_s(\vec{R}) = E_s(\vec{R}_0) + (\vec{R} - \vec{R}_0) \frac{dE_s}{dR}|_{\vec{R}=\vec{R}_0} + \frac{1}{2}(\vec{R} - \vec{R}_0)^2 \frac{d^2E_s}{dR^2}|_{\vec{R}=\vec{R}_0} + ... \tag{2.18}$$

As $E_s(\vec{R})$ has a minima at $\vec{R}_0$, so that $\frac{dE_s}{dR} = 0$. Approximately, $E_s(\vec{R})$ can be written as a parabolic function by neglecting the fourth and the higher order terms. Hence,

$$E_s(\vec{R}) = E_s(\vec{R}_0) + \frac{1}{2} k (\vec{R} - \vec{R}_0)^2 \tag{2.19}$$

similarly, the rotational energy E_J can be written as following manner at the equilibrium position $\vec{R}_0$:

$$E_J(\vec{R}_0) = \frac{\hbar^2}{2\mu R_0^2} J(J+1) \tag{2.20}$$

Now the radial equation become the eigenvalue equation of the E_v :

$$\left[-\frac{\hbar^2}{2\mu} \frac{d^2}{dR^2} + \frac{1}{2} k (\vec{R} - \vec{R}_0)^2 - E_v \right] \psi_v = 0 \tag{2.21}$$

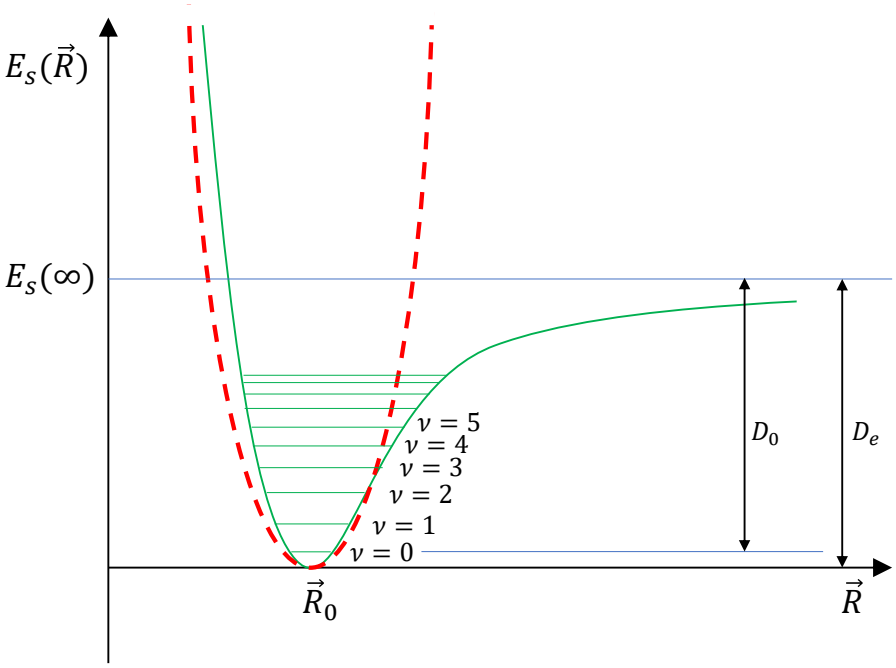

Fig. 2.3: Vibrational levels of a diatomic molecule. The red dashed line shows the parabolic approximation with respect to the equilibrium internuclear separation.

The above equation corresponds to *simple harmonic motion* with the force constant k. The eigenvalues E_ν can be written as

$$E_\nu = \hbar\omega_0(\nu + \frac{1}{2}) \tag{2.22}$$

However, a better representation of the potential energy $E_s(\vec{R})$ can be obtained by imposing an empirical potential function $V(\vec{R})$ proposed by P.M. Morse, i.e. $E_s(\vec{R}) = E_s(\infty) + V(\vec{R})$. The functional form of $V(\vec{R})$ is :

$$V(\vec{R}) = D_e\left[\exp^{-2\alpha(\vec{R}-\vec{R}_0)} - 2\exp^{-\alpha(\vec{R}-\vec{R}_0)}\right] \tag{2.23}$$

where $\vec{R}_0$, D_e and α are constants (45). The functional form of $V(\vec{R})$ suggests that it is attractive at large internuclear separation and has a minima at $\vec{R}$ with value $-D_e$, so that $D_e = E_s(\infty) - E_s(\vec{R}_0)$. The $V(\vec{R})$ can be expanded in powers of $(\vec{R} - \vec{R}_0)$:

$$V(\vec{R}) = D_e\left[-1 + \alpha^2(\vec{R}-\vec{R}_0)^2 + ...\right] \tag{2.24}$$

and comparing it with the approximated $E_s(\vec{R})$ value, we obtain :

$$D_e\alpha^2 = \frac{1}{2}k \tag{2.25}$$

The lower energy levels for Morse potential can be accurately expressed as :

$$E_v = \hbar\omega_0\left[(v+\frac{1}{2}) - \beta(v+\frac{1}{2})^2\right] \tag{2.26}$$

where β is a very small number ($\beta << 1$). The β term is usually expressed as *anharmonicity constant*, which is given as :

$$\beta\omega_0 = \frac{\hbar\omega_0^2}{4D_e} \tag{2.27}$$

The dissociation energy D_0 of the diatomic molecule is usually represented in terms of D_e and ω_0, i.e. $D_0 = D_e - \hbar\omega_0/2$.

2.1.3 Electronic Structure of Diatomic Molecules

Till now we have discussed how to solve the *nuclear wave equation* of the molecular system to understand the nuclear motion. However, the contribution of the *electronic* part is also required to understand the whole molecular system.

Let us consider the simplest diatomic molecular system, H_2^+, which is made up of two protons and an electron. The *electronic wave equation* of H_2^+ can be written in the following manner :

$$\left[-\frac{\hbar^2}{2\mu}\nabla^2_{\vec{R}} - \frac{e^2}{|\vec{r}_A|} - \frac{e^2}{|\vec{r}_B|} + \frac{e^2}{|\vec{R}|} - E_s\right]|\phi_s\rangle = 0 \tag{2.28}$$

where $\vec{r}_A$, $\vec{r}_B$ and $\vec{R}$ depends upon each other like $\vec{r}_A = \vec{r} + \vec{R}/2$ and $\vec{r}_B = \vec{r} - \vec{R}/2$ (see Figure-2.4). This equation can be solved by several approximations to obtain a more general solution to extend it to other molecular systems. At larger internuclear separation this single electron gets attached to any one of the protons either A or B. So, the

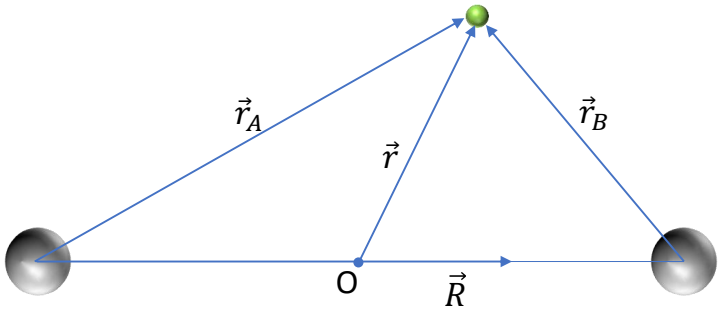

Fig. 2.4: A schematic representation of the coordinate system for hydrogen molecular ion H_2^+.

overall wavefunction can be written as a superposition of the two atomic orbitals :

$$|\phi_s(\vec{R};\vec{r})\rangle = N\,[|\psi_{1s}(A)\rangle \pm |\psi_{1s}(B)\rangle] \tag{2.29}$$

where $\psi_{1s}(A)$ and $\psi_{1s}(B)$ is the ground state wave function for atomic hydrogen and N is the normalization factor. The approximated molecular orbital obtained from the superposition of atomic orbitals is known as *linear combination of atomic orbital-molecular orbital* or LCAO-MO.

The atomic eigenfunctions can be simultaneous eigenfunction of H, $\vec{L}^2$ and L_z. Hence, both the orbital quantum number L and M_L are conserved. However, for di-atomic molecular system the *Hamiltonian* does not commute with $\vec{L}^2$ as the internuclear axis specifies a particular direction in space but commutes with L_z. The electronic eigenfunction $|\phi_s(\vec{R};\vec{r})\rangle$ can be expressed as the simultaneous eigenfunction of H and L_z. So that :

$$L_z|\phi_s(\vec{R};\vec{r})\rangle = M_L\hbar|\phi_s(\vec{R};\vec{r})\rangle \tag{2.30}$$

$$L_z|\phi_s(\vec{R};\vec{r})\rangle = \pm\Lambda\hbar|\phi_s(\vec{R};\vec{r})\rangle \tag{2.31}$$

where $\Lambda = 0, 1, 2, 3, ...$ Molecular spectroscopic notations are introduced by analogy with the atomic notations and the notations corresponding to $\Lambda = 0, 1, 2, 3, ...$ are $\Sigma, \Pi, \Delta, \Phi$ respectively. For the individual electrons lower case symbols are used, like $\sigma, \pi, \delta, \phi$ etc. The molecular orbitals can also be characterized depending upon the symmetry property of the orbitals. For homonuclear diatomic molecules, there exists a center of symmetry at the mid-point of nuclei A and B. Considering the midpoint of the internuclear separation as the origin of the coordinates, the *Hamiltonian* remains invariant under the inversion of the coordinates of the electrons with respect to the origin. The molecular orbital wavefunction symmetric with respect to the plane passing through the center of symmetry is called '*gerade*'. On the other hand, the asymmetric molecular orbital wavefunctions are known as '*ungerade*' orbitals. Additional symmetry property can be introduced by considering the plane containing the internuclear axis for Σ state. Molecular wavefunction with symmetric reflection with respect to this plane is denoted as '$+$' and the asymmetric ones are represented as '$-$'. The electronic state of the molecular systems are represented as a term symbol :

$$^{2S+1}\Lambda_{g/u}^{(+/-)} \tag{2.32}$$

Here, 'S' is the total electronic spin quantum number and the multiplicity is denoted as '$2S$+1'.

The LCAO-MO wavefunctions for the hydrogen molecular ion are characterised on the basis of the orbital symmetry, $N[|\psi_{1s}(A)\rangle + |\psi_{1s}(B)\rangle]$ shows the σ_g character and the $N[|\psi_{1s}(A)\rangle - |\psi_{1s}(B)\rangle]$ shows the σ_u character. The LCAO approximation is valid only at larger internuclear separation, however, it can be used as a trial function to obtain the eigenvalues and the eigenfunctions using the variational approach :

$$E_{g,u}(\vec{R}) = \frac{\langle \phi_s(\vec{R};\vec{r})|H|\phi_s(\vec{R};\vec{r})\rangle}{\langle \phi_s(\vec{R};\vec{r})||\phi_s(\vec{R};\vec{r})\rangle} \tag{2.33}$$

For the fixed internuclear separation $|\overrightarrow{R}| = R$ the expression of the $E_{g,u}(\vec{R})$ looks like(44; 45):

$$E_{g,u}(\vec{R}) = E_{1s} + \frac{1}{R}\frac{(1+R)\exp^{-2R} \pm (1-\frac{2}{3}R^2)\exp^{-R}}{1 \pm (1+R+\frac{1}{3}R^2)\exp^{-R}} \tag{2.34}$$

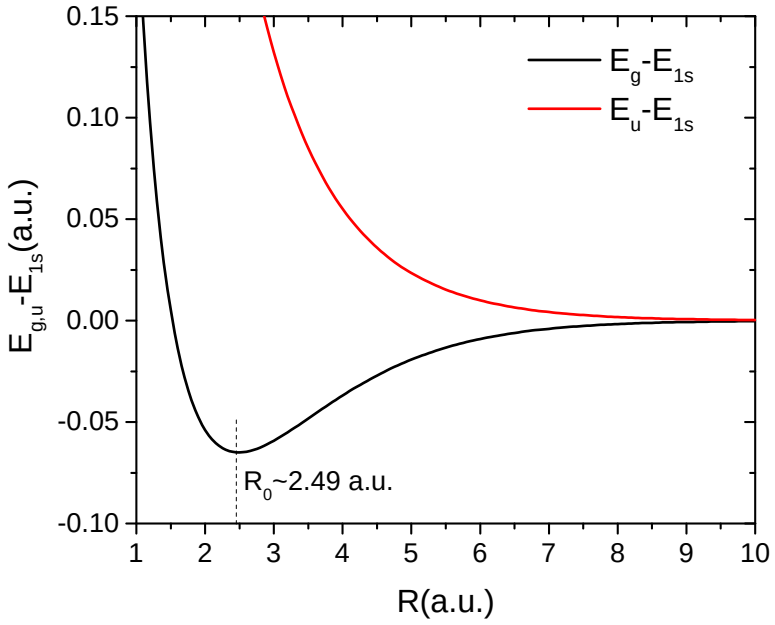

Fig. 2.5: The potential energy curves of the H_2^+ molecular ion obtained by using the simple trial LCAO-MO wavefunctions for variational method

The eigenvalues $E_{g,u}(\vec{R})$ depends upon the internuclear separation R and the functions $E_g(\vec{R}) - E_{1s}$ and $E_u(\vec{R}) - E_{1s}$ are plotted together in Figure-2.5. The orbital $|\phi_s(\vec{R};\vec{r})\rangle_g$ exhibits a minima at $R_0 = 2.49$a.u. and it leads to a stable bound state. It is usually termed as *bonding* molecular orbital and for this particular case of hydrogen molecular ion it represents the ground state and termed as $1\sigma_g$. However, $|\phi_s(\vec{R};\vec{r})\rangle_u$ has no minima over the entire range of internuclear separation and this repulsive $|\phi_s(\vec{R};\vec{r})\rangle_u$ state is known as *antibonding* orbital. For the present scenario this *antibonding* orbital is termed as $1\sigma_u$ orbital.

The probability density of the electron over the molecule can be obtained from $-e^2|_{g,u}\langle\phi_s(\vec{R};\vec{r})|\phi_s(\vec{R};\vec{r})\rangle_{g,u}|$ and it can be visualised as a pictorial representation called molecular orbital structure. For multi-electron molecular systems the orbital structure of the outermost orbital plays an significant role in the ionization process. The molecular orbital structures of a homonuclear oxygen molecule are shown in the Figure-2.6.

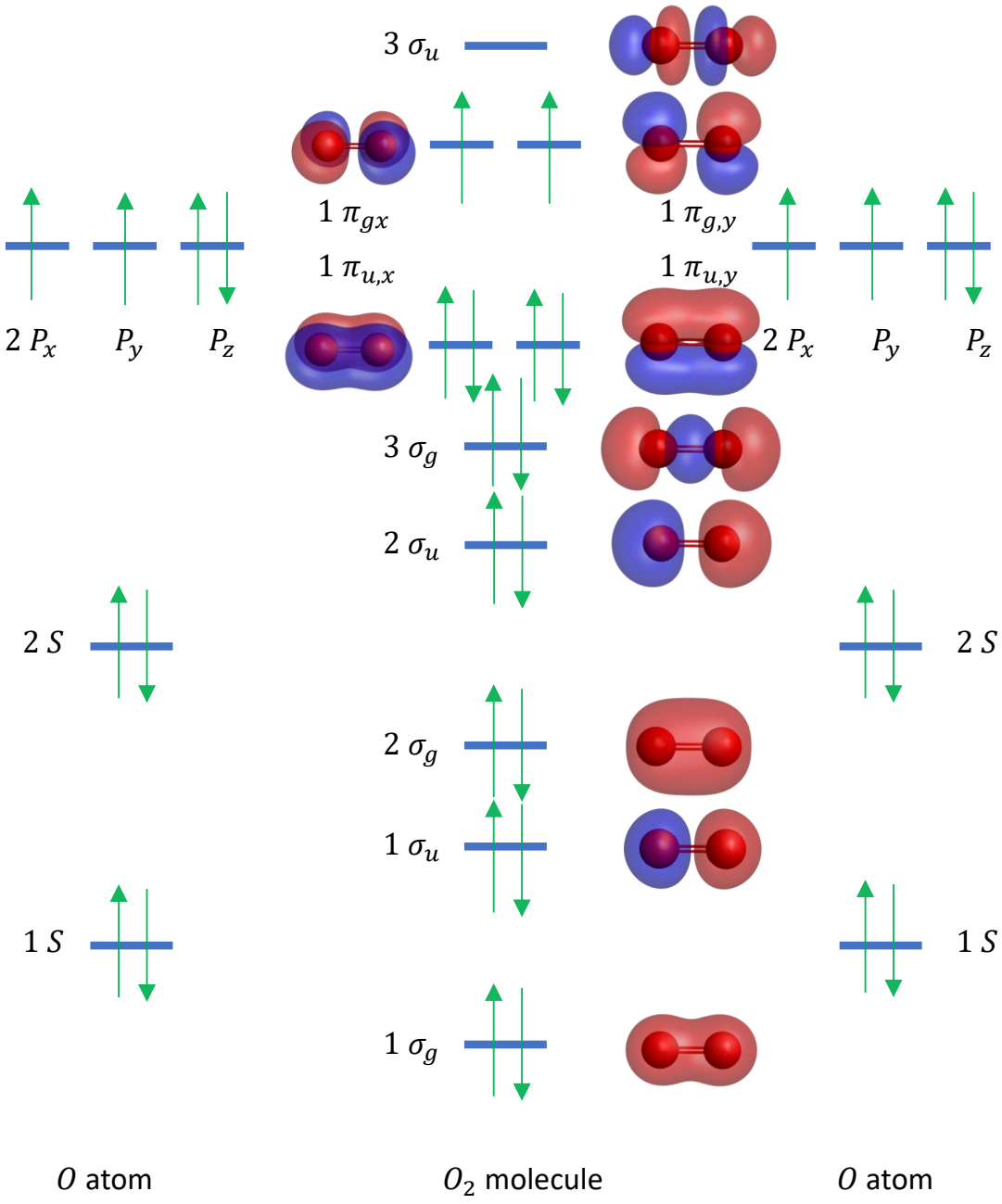

Fig. 2.6: The electronic configuration of O_2 along with the orbital structures

2.2 Ionization of Molecules in Intense Laser Field

The interaction of laser field with the atoms and molecules has been well studied both in theory and experiments(46; 47). In general atoms and molecules goes through ionization due to the interaction with the laser field. The ionization takes place after absorbing a photon with energy $h\nu$ greater than the ionization potential I_p of the atom or molecule and the excess energy is carried away by the ejected electron. For photon energy, $h\nu \ll I_p$ the ionization process occurs through different mechanisms, such as multi-photon ionization, tunneling ionization, and over the barrier ionization depending upon the wavelength and intensity of the laser pulse. In the year of 1964, Keldysh introduced an adiabatic parameter to distinguish the perturbative multi-photon ionization regime and the non-perturbative regime, which includes both the tunneling ionization and over the barrier ionization(48).

2.2.1 Keldysh Parameter

In the non-perturbative regime the oscillating electric field distorts the atomic potential significantly and if the electric field changes very slowly with respect to the electronic time scale, so it experiences a slow variation in the distorted potential barrier, which allows electrons to escape the barrier by tunneling. With the increasing field strength the possibility of the over the barrier ionization increases. Figure-2.7 shows the schematic diagram of the distorted atomic potential in the oscillating electric field. The dimensionless Keldysh parameter is defined as the ratio of the classical time taken by the electron to tunnel through the distorted potential barrier to the half time of the laser optical cycle, so that :

$$\gamma = \frac{\text{tunneling time}}{\text{half of the laser period}} = \frac{\tau}{\frac{1}{2}T} \tag{2.35}$$

The classical time taken by the electron to pass through the potential barrier can be expressed as

$$\tau = \frac{\text{tunneling width}}{\text{tunneling velocity}} \tag{2.36}$$

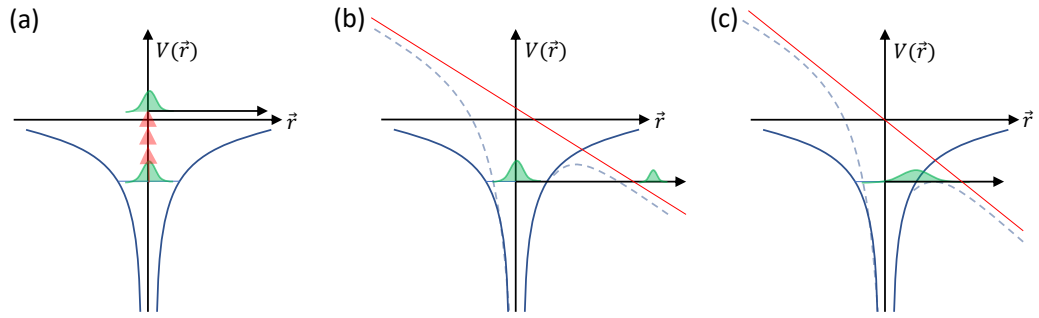

Fig. 2.7: Schematic 1-D diagram showing the distorted atomic potential in the presence of an electric field for three different ionization mechanisms (a) multi-photon ionization, (b) tunneling ionization and (c) over-the-barrier ionization. The blue curves shows the field free atomic potential and the dashed curves represents the distorted potential in the presence of the external electric field with the red solid line showing the potential due to the laser field .

This ratio indicates how quickly the potential barrier oscillates in comparison to the electron to tunnel ionization. In the Coulombic potential the electron is assumed to oscillate with kinetic energy equal to the binding energy E_b in the absense of the external field. The average velocity is written as (49):

$$\langle v_{avg} \rangle = \sqrt{\frac{2E_b}{m_e}} \tag{2.37}$$

where m_e is the mass of the electron. In the presence of the external field the electron with $\langle v_{avg} \rangle$ velocity will pass the potential barrier with width x, i.e.

$$x = \frac{E_b}{|e|F} \tag{2.38}$$

here, e is the one electronic charge and F is the peak field strength. From these above two equations the tunneling time can be estimated easily and it is represented as :

$$\tau = \frac{x}{\langle v_{avg} \rangle} = \frac{1}{|e|F} \sqrt{\frac{E_b m_e}{2}} \tag{2.39}$$

The tunneling ionization is possible only when the classical tunneling time τ is less than the half time of the optical cycle of the laser field. Now, the Keldysh parameter can be written as :

$$\gamma = \frac{\omega \sqrt{2 m_e E_b}}{|e|F} = \sqrt{\frac{I_p}{2U_p}} \tag{2.40}$$

where $I_p (= E_b)$ is the ionization potential and U_p is the ponderomotive enrgy, i.e. the average kinetic energy of the electron gained in the oscillatory electric field of the laser pulse. The ponderomotive energy can be written in a simplified manner in terms of intensity and the wavelength of the laser pulse, i.e. :

$$U_p = \frac{e^2 F^2}{4 m_e \omega^2} \sim 9.33 \times 10^{-14} I(W/cm^2) \lambda^2 (\mu m) \tag{2.41}$$

The Keldysh parameter can be estimated easily if both the intensity and the wavelength of the laser field is known along with the ionization potential of the atoms or molecules. The Keldysh parameter permits a simple distinction between tunnel ionization and multiphoton processes. The tunnel ionization is dominant only when $\gamma \ll 1$(50). However, for $\gamma \gg 1$ multiphoton ionization process is dominant. At $\gamma \sim 1$ both the tunneling and multiphoton processes contributes in the ionization. In the follwing subsections the multiphoton ionization and tunneling ionization mechanisms are discussed in details.

2.2.2 Multi-photon Ionization

In the previous section we have discussed, the multiphoton ionization process is dominant only when the $\gamma \gg 1$. For most of the atoms and molecules the required intensity for near infrared laser field remains below $\sim 10^{12}$ W/cm^2.

Let us do a quantum mechanical treatment for single electron atomic or molecular system interacting with a electromagnetic field(51; 52). The time evolution of the system

can estimated by solving the following time-dependent Schrödinger equation :

$$i\frac{\delta}{\delta t}|\Psi(\vec{r},t)\rangle = \hat{H}|\Psi(\vec{r},t)\rangle = (\hat{H}_0 + \hat{H}_{int})|\Psi(\vec{r},t)\rangle \tag{2.42}$$

The above equation can be solved by taking time-dependent perturbative approach only if the interaction term is weak. For that purpose a parameter λ is introduced to denote the order of the perturbation. So that,

$$i\frac{\delta}{\delta t}|\Psi(\vec{r},t)\rangle = (\hat{H}_0 + \lambda\hat{H}_{int})|\Psi(\vec{r},t)\rangle \tag{2.43}$$

The eigenfunctions $|\psi_k(\vec{r})\rangle$ of the *Hamiltonian* $\hat{H}_0$ are not the eigenfunctions of the exact *Hamiltonian* of the system in the presence of the oscillating electric field. Now the full trial solution of the *Hamiltonian* can be expanded with the time-dependent expansion coefficient $c_k(t)$:

$$|\Psi(\vec{r},t)\rangle = \sum_k c_k(t)|\psi_k(\vec{r})\rangle \exp^{-iE_k t} \tag{2.44}$$

Putting back this equation in the above Schrödinger equation, we obtained a coupled differential equation :

$$\frac{\delta c_b(t)}{\delta t} = \frac{1}{i}\sum_k \lambda c_k(t)\langle\psi_b(\vec{r})|\hat{H}_{int}|\psi_k(\vec{r})\rangle \exp^{i(E_b-E_k)t} \tag{2.45}$$

In the time-dependent perturbative approach the coefficients c_k are expanded in powers of the λ :

$$c_k(t) = c_k^{(0)}(t) + \lambda c_k^{(1)}(t) + \lambda^2 c_k^{(2)}(t) + \lambda^3 c_k^{(3)}(t) + ... \tag{2.46}$$

Inserting this expanded $c_k(t)$ in the above coupled equation and the solution of each orders are obtained by integrating in time in iterative manner. At the starting time $t = 0$ the system is considered to be in the initial state $|\psi_a(\vec{r})\rangle$ and it should be confirmed by the zeroth order term in the expansion series of $c_k(t)$. So that,

$$c_k^{(0)}(t) = \delta_{ka} \tag{2.47}$$

The higher order terms can be expressed as the following manner :

$$c_k^{(1)}(t) = \frac{1}{i}\int_0^t dt' \langle \psi_b(\vec{r})|\hat{H}_{int}(t')|\psi_a(\vec{r})\rangle \exp^{i(E_b-E_a)t'} \tag{2.48}$$

$$\begin{aligned} c_k^{(2)}(t) =& \frac{1}{i^2}\sum_k \int_0^t dt' \int_0^{t'} dt'' \langle \psi_b(\vec{r})|\hat{H}_{int}(t')|\psi_k(\vec{r})\rangle \langle \psi_k(\vec{r})|\hat{H}_{int}(t'')|\psi_a(\vec{r})\rangle \\ & \times \exp^{i(E_b-E_k)t'} \exp^{i(E_k-E_a)t''} \end{aligned} \tag{2.49}$$

These equations shows single and double interaction with the electromagnetic field causing the transition from initial $|\psi_a(\vec{r})\rangle$ state to final $|\psi_a(\vec{r})\rangle$ state.
The interaction term in the *Hamiltonian* due to the interaction with the electromagnetic field can be written as

$$\hat{H}_{int} = -\frac{\vec{p}\cdot\vec{A}}{c} \tag{2.50}$$

where $\vec{p}$ is the momentum operator and the $\overrightarrow{A}$ is the vector potential of the electromagnetic field under Coulomb gauge condition with $\nabla\cdot\vec{A} = 0$. The vector potential $\vec{A}$ can be written as :

$$\vec{A}(\vec{r},t) = A_0\hat{n}(\exp^{i(\vec{k}.\vec{r}-\omega t)} + \exp^{i(\vec{k}.\vec{r}+\omega t)}) \tag{2.51}$$

with the unit vector $\hat{n}$, showing the polarization axis and the wavevector $\vec{k}$. If the wavelength λ is greater than the dimension of the atomic or molecular system $\vec{k}.\vec{r} \ll 1$, dipole approximation $\exp^{i\vec{k}.\vec{r}} \sim 1$ can be applied. So that, the interaction term of the *Hamiltonian* can be written as $\hat{H}_{int} = -\vec{d}\cdot\vec{\varepsilon}$, here $\vec{d}$ indicates the dipole moment.
The transition rate from initial $|\psi_a(\vec{r})\rangle$ state to final $|\psi_b(\vec{r})\rangle$ state could be estimated from the square of the expansion coefficients after simplifying it with the approximated interaction term of the *Hamiltonian* for a duration τ. So that,

$$R_{a\to b}^{(n)} = \frac{|c_b^{(n)}(t)|^2}{\tau} \tag{2.52}$$

It can be simplified further and in terms of intensity ($I_0 \propto \varepsilon^2$) and the transition rate for the first and the second order processes are expressed as :

$$R_{a\to b}^{(1)} \propto I_0 |\langle \psi_b(\vec{r})|d|\psi_a(\vec{r})\rangle|^2 \delta(E_b - E_a - \omega) \tag{2.53}$$

$$R^{(2)}_{a\to b} \propto I_0^2 \langle \psi_b(\vec{r})|d|\psi_k(\vec{r})\rangle \langle \psi_k(\vec{r})|d|\psi_a(\vec{r})\rangle \delta(E_b - E_a - 2\omega) \tag{2.54}$$

and it can be extended to n-th order and the transition rate for the n-th order process will look like :

$$\begin{aligned} R^{(n)}_{a\to b} \propto & I_0^n \langle \psi_b(\vec{r})|d|\psi_k(\vec{r})\rangle \langle \psi_k(\vec{r})|d|\psi_{k'}(\vec{r})\rangle ... \langle \psi_{k^n}(\vec{r})|d|\psi_a(\vec{r})\rangle \\ & \times \delta(E_b - E_a - n\omega) \end{aligned} \tag{2.55}$$

In the case of more than one photon absorption process the electron is excited from the initial $|\psi_a(\vec{r})\rangle$ to an virtual intermediate state $|\psi_k(\vec{r})\rangle$ by one photon absorption and in each successive steps one photon are absorbed untill it reaches the final $|\psi_b(\vec{r})\rangle$ state(53). In general these virtual $|\psi_k(\vec{r})\rangle$ states are not the eigenfunction of the unperturbed *Hamiltonian*. The lifetime of these virtual states are usually very short and it can be esitmated from the Heisenberg's uncertainity principle. It indicates that two successive photon absorption should occur within the lifetime of these virtual intermediate states. So that the high spatial and temporal photon density in the vicinity of the atomic or molecular system will increase the chances of the multi-photon absorption. This derivation also holds for the transition between the bound state $|\psi_a(\vec{r})\rangle$ and the continuum(51). It suggests this derivation is valid for the multi-photon ionization processes.

2.2.3 Tunneling Ionization

The tunneling ionization method is dominant for high intensity ($\sim 10^{14}$ W/cm^2) regime for the near infrared laser field. In this intensity and wavelength regime the time period of the optical cycle of the laser field is greater than the tunneling time and it can be treated with a quasi-classical approach. Landau and Lifshitz had given the generalised form of the ionization rate of the ground state hydrogen atom as a function of the strength of the static electric field, and it is written as(54) :

$$\Gamma(F) = \frac{4}{F} \exp^{-\frac{2}{3F}} \tag{2.56}$$

however, it is only valid for the field strength smaller than the Coulomb field associated with the atom. The ionization rate of complex atoms or atomic ions from arbitary electronic states via quasi-classical approach was esitimated by Ammosov, Delone and Krainov, which is known as ADK theory(55). For the molecular system the ADK model is extended further by Tong *et al.*(36), which is called MO-ADK theory.

ADK Theory

The ADK theory is based upon several approximations. Firstly, in contrast to the multi-photon ionization the intermediate states have no significance in the tunneling ionization, where only the initial states and the final states of the electons are considered. The second assumption is to assume the external electric field of the laser pulse as a static one during tunneling, however, for oscillating field, the static field F can be substituted by $F.\cos(\omega t)$ and integrating it over the complete optical cycle,T. As a result, the ionization rate from an arbitrary state of the simplest atomic system, i.e. hydrogen atom in the static electric field can be written as :

$$\Gamma_{static}(F) = |C_{n,l}|^2 f(l,m) E_b \left(2\frac{F_0}{F}\right)^{2n-|m|-1} \exp^{-\frac{2}{3}\frac{F_0}{F}} \tag{2.57}$$

where, E_b is the binding energy of the hydrogen atom, l is the orbital angular momentum, m is the projection of l along the direction of the electric field. Also, $F_0 = (2E_b)^{3/2}$ and $\left(2\frac{F_0}{F}\right)^{2n}$ shows the long range Coulomb field. On the other side, $C_{n,l}$ and $f(l,m)$ defines the initial atomic states. The functional form of $C_{n,l}$ and $f(l,m)$:

$$f(l,m) = \frac{(2l+1)(l+|m|)!}{2^{|m|}|m|!(l-|m|)!} \tag{2.58}$$

$$|C(n,l)|^2 = \frac{2^{2n}}{n(n+l)!(n-l-1)!} \tag{2.59}$$

Ammosov, Delone and Krainov extended this by introducing an effective principal quantum number n^* instead of the principal quantum number n of the hydrogen atom. The effective principal quantum number n^* is written as $n^* = Z/\sqrt{2E_b}$, where Z is the screened charge of the nucleus seen by the active electron. Similarly, the orbital mo-

mentum l is replaced by the effective orbital momentum l^*, where

$$l^* = \begin{cases} 0 & \text{for } l \ll n^* - 1 \\ n^* - 1 & \text{otherwise} \end{cases} \tag{2.60}$$

For simplicity, the asymptotic Stirling formula is used for $n^* \gg 1$ and $|C(n,l)|^2$ can be written as :

$$|C(n,l)|^2 = \frac{1}{2\pi n^*} \left(\frac{4\zeta^2}{n^{*2} - l^{*2}} \right)^{n^*} \left(\frac{n^* - l^*}{n^* + l^*} \right)^{l^* + \frac{1}{2}} \tag{2.61}$$

where ζ is the Euler's number. Putting $|C(n,l)|^2$, back into the ionization rate function of the hydrogen atom, the ionization rate for larger atomic system looks like :

$$\Gamma_{static}(F) = \frac{F}{8\pi Z} f(l,m) \left(\frac{4\zeta^2}{n^{*2} - l^{*2}} \right)^{n^*} \left(\frac{n^* - l^*}{n^* + l^*} \right)^{l^* + \frac{1}{2}} \times \left(\frac{2Z^3}{n^{*3} F} \right)^{2n^* - |m|} \exp^{-\frac{2Z^3}{3n^{*3} F}} \tag{2.62}$$

This modified ionization rate is applicable for complex electronic structures. The ionization rate is maximum when $|m| = 0$, however, the ionization rate is smaller for other values of $|m|$. Now using the assumption $|m| = 0$ and $l^* = n^* - 1$, the ionization rate can be represented as :

$$\Gamma^{m=0}_{static}(F) = \frac{\zeta}{2\pi} \frac{Z^2(2l+1)}{n^{*3}\sqrt{(2n^* - 1)}} \left(\frac{4\zeta Z^3}{(2n^* - l) n^{*3} F} \right)^{2n^* - 1} \exp^{-\frac{2Z^3}{3n^{*3} F}} \tag{2.63}$$

Now, for the oscillating electric field the ionization rate can be estimated by replacing the static electric field $\vec{F}$ by the linearly polarized oscillating electric field expressed as $\vec{F}(t) = F \times \cos(\omega t)\hat{n}$, where $\hat{n}$ deontes the direction of the polarization axis. Under the adiabatic approximation the ionization rate for the linearly polarized oscillating electric field Γ_{LP} can be written as (56):

$$\Gamma_{LP}(\varepsilon) = \frac{1}{\pi} \int_{-\pi/2}^{\pi/2} \Gamma(t) d(\omega t) \tag{2.64}$$

The $\Gamma(t)$ can be obtained by replacing the static electric field into the oscillating one. Now the exponential part in the $\Gamma(t)$ has a term $1/\cos(\omega t)$, which indicates the ionization rate is maximum when $\cos(\omega t) \sim 1$. To approximate the rapidly changing ex-

ponential term $1/\cos(\omega t)$ is expanded by Taylor series expansion and taking only the dominant term the $\Gamma(t)$ can be expressed as :

$$\Gamma(t) \sim \Gamma_{static} \exp^{-\frac{F_0}{3F}(\omega t)^2} \tag{2.65}$$

Integrating $\Gamma(t)$ over the one optical cycle, we have obtained the ionization rate in linearly polarized oscillating electric field is expressed as :

$$\Gamma_{LP}(F) = \sqrt{\left(\frac{3F}{\pi F_0}\right)}\Gamma_{static} \tag{2.66}$$

As $F \ll F_0$, the ionization rate in the presence of the linearly polarized oscillating electric field is always less than the ionization rates estimated for the static electric field.

MO-ADK Theory

The ADK theory of tunneling ionisation shows a reasonable match with the experimental data of multi-electronic atomic system. Several studies had indicated that ionization processes do not differ much for atoms and molecules. However, for various molecular systems the ionization rates are found to be suppressed in comparison with other atomic systems having similar range of ionization potential, I_p. Hence, for molecular systems ADK theory needs to be modified accordingly. Tong *et al.*(36) have introduced a modified wavefunction for the molecular system and this modification helps to predict the ionization rate for most of the molecular systems.

The electronic wavefunction of a diatomic molecule is represented as a sum of the linear combination of the atomic orbitals in the asymptotic region. These LCAO-MO wavefunctions are written as :

$$\Psi^{\lambda}(\vec{r}) = \sum_{l} C_{l,\lambda} F_l(r) Y_{l,\lambda}(\hat{r}) \tag{2.67}$$

where, l is the angular momentum and λ is the projection of it along the internuclear axis. $Y_{l,\lambda}(\hat{r})$ is the spherical harmonics for different l and λ values. The coefficients

$C_{l,\lambda}$ depends upon l and λ and are normalized such that the asymptotic form of the $F_{l,\lambda}$ can be written in the following manner :

$$F_l(r) = r^{(Z_c/\kappa)-1} \exp^{-\kappa r} \tag{2.68}$$

here, Z_c is the effective Coulomb charge and $\kappa = \sqrt{2I_p}$ as I_p is the ionization potential for a specefic valence orbital. These coefficients can be estimated by using various methods like : the Hartree-Fock method(57), Density Functional Theory(58) etc.

For a special case assuming the molecule is aligned along the static external electric field, during ionization the valance electron is ejected along the field. The corresponding spherical harmonics can be written as :

$$Y_{l,\lambda}(\hat{r}) \sim Q(l,\lambda) \frac{\sin^{|\lambda|}\theta}{2^{|\lambda|}|\lambda|!} \frac{\exp^{i\lambda\phi}}{\sqrt{2\pi}} \tag{2.69}$$

where,

$$Q(l,\lambda) = (-1)^{\lambda} \sqrt{\frac{(2l+1)(l+|\lambda|)!}{2(l-|\lambda|)!}} \tag{2.70}$$

Now putting the functional forms of the spherical harmonics in the LCAO-MO wavefunction, we get :

$$\Psi^{\lambda}(r,\theta,\phi) = \sum_l C_{l,\lambda} Q(l,\lambda) r^{(Z_c/\kappa)-1} \exp^{-\kappa r} \frac{\sin^{|\lambda|}\theta}{2^{|\lambda|}|\lambda|!} \frac{\exp^{i\lambda\phi}}{\sqrt{2\pi}} \tag{2.71}$$

Now the final expression of the ionization rate for the molecules aligned to the external field can be written as the following :

$$W_{static}^{MO-ADK}(F,\theta=0) = \frac{B^2(\lambda)}{2^{|\lambda|}|\lambda|!} \frac{1}{\kappa^{2Z_c/\kappa-1}} \left(\frac{2\kappa^3}{F}\right)^{\frac{2Z_c}{\kappa}-|\lambda|-1} \exp^{-\frac{2\kappa^3}{3F}} \tag{2.72}$$

where, $B(\lambda)$ represents $\sum_{l\geq\lambda} C_{l,\lambda} Q(l,\lambda)$ and $B^2(\lambda)$ defines electron density in the tunneling region along the direction of the static electric field. For example, the valence shell of N_2 molecule has σ symmetry and it suggests $\lambda = 0$, however, for O_2 molecule valence orbital has π symmetry and it suggests $\lambda = 1$. For $\lambda = 0$ condition, electron density is larger along the molecular axis and hence the ionization rate will be large if

the molecule is aligned along the electric field. In contrast, for O_2 molecule as $\lambda = 1$, the electron density vanishes along the molecular axis hence the ionization rate drops to zero for the aligned molecule.

However, if the molecular axis makes an angle θ with the electric field then the term $B(\lambda)$ will change due to the rotation of angle θ and can be estimated by(59) :

$$B(\lambda') = \sum_{l \geq \lambda} C_{l,\lambda} Q(l,\lambda') D^{l}_{\lambda,\lambda'}(0,\theta,0) \tag{2.73}$$

$D^{l}_{\lambda,\lambda'}(0,\theta,0)$ defines the rotation matrix with the Euler angles $(0,\theta,0)$. Using Wigner's angular function $D^{l}_{\lambda,\lambda'}(\theta)$ term can be rewritten as (60):

$$D^{l}_{\lambda,\lambda'}(\theta) = \sum_{j} (-1)^{j} \frac{\sqrt{(l+\lambda)!(l-\lambda)!(l+\lambda')!(l-\lambda')!}}{(l-\lambda'-j)!(l+\lambda-j)!\,j!(j+\lambda'-\lambda)!} \times \left(\cos\frac{\theta}{2}\right)^{2l+\lambda-\lambda'-2j} \left(\sin\frac{\theta}{2}\right)^{2j+\lambda'-\lambda} \tag{2.74}$$

Finally, the ionization rate for static electric field ε can be written as :

$$W^{MO-ADK}_{static}(F,\theta) = \frac{B^2(\lambda')}{2^{|\lambda'|}|\lambda'|!} \frac{1}{\kappa^{2Z_c/\kappa-1}} \left(\frac{2\kappa^3}{F}\right)^{\frac{2Z_c}{\kappa}-|\lambda'|-1} \exp^{-\frac{2\kappa^3}{3F}} \tag{2.75}$$

And similar to the ADK theory the ionization rate of the molecules obtained for the static electric field can be extended to determine the ionization rate for low-frequency linearly polarized oscillating electric field can be written as :

$$W_{LP}(F,\theta) = \sqrt{\left(\frac{3F_{max}}{\pi\kappa^3}\right)} W_{static}(F_{max},\theta) \tag{2.76}$$

Here, F_{max} denotes the peak value of the electric field observed in the optical cycle and $\sqrt{\left(\frac{3F_{max}}{\pi\kappa^3}\right)}$ indicates the average ionization rate over one optical cycle.

2.3 Dissociation in Intense Laser Field

In the presence of the intense laser field molecular system goes through ionization and creates vibrational wavepackets over some excited electronic state. If the excited elec-

tronic state is repulsive in nature, then the newly formed molecular ion eventually dissociates into several ionic and neutral fragments. Even if the excited electronic state is bound, the dissociation can take place through photon induced coupling with a repulsive state in the presence of the laser field.

Hydrogen molecular ion is the simplest system to study the dissociation mechanism in the presence of the laser field due to the availability of only two low-lying electronic states. The vibrational wavepackets created over the bound electronic state $1\sigma_g$ can dissociates thorugh photon coupled repulsive $1\sigma_u$ state. The dissociation process can be understood from several theoretical approach like Floquet or molecular 'dressed' state formalism, and time-dependent approach. The Floquet picture of the molecular dissociation in the intense laser field is discussed in details in the following section :

2.3.1 Floquet Picture

The time-dependent Schrödinger equation of a molecular system can be written in the following manner :

$$i\frac{\delta}{\delta t}|\Psi(\vec{r},\vec{R},t)\rangle = \hat{H}(\vec{r},\vec{R},t)|\Psi(\vec{r},\vec{R},t)\rangle \tag{2.77}$$

with electronic coordinates $\vec{r}$ and nuclear coordinate $\vec{R}$. The *Hamiltonian* $\hat{H}(\vec{r},\vec{R},t)$ can be separated into time-independent field free *Hamiltonian* $\hat{H}(\vec{r},\vec{R})$ and time-dependent interaction term $V(\vec{r},t)$:

$$\hat{H}(\vec{r},\vec{R},t) = \hat{H}(\vec{r},\vec{R}) + V(\vec{r},t) \tag{2.78}$$

In the presence of the linearly polarized oscillating electric field $\vec{F}(t) = F_0 \times \cos(\omega t)\hat{n}$, the interaction term can be simplified as (61; 62; 63; 64):

$$V(\vec{r},t) = -e\vec{r}.\vec{F}(t) = \frac{eF_0 z}{2}\left(\exp^{i\omega t} + \exp^{-i\omega t}\right) = V_- \exp^{i\omega t} + V + \exp^{-i\omega t} \tag{2.79}$$

assuming the dipole moment $e\vec{r}$ is exactly aligned along the oscillating electric field. The time-dependency of the *Hamiltonian* comes from the interaction term and in the

presence of the oscillating electric field the *Hamiltonian* shows a periodic behaviour $\hat{H}(t) = \hat{H}(t+T)$ with time period $T = 2\pi/\omega$. Here, introducing the Floquet theorem, the guess solution of the *Hamiltonian* can be expressed as :

$$|\Psi(\vec{r},\vec{R},t)\rangle = \exp^{iEt/\hbar} |F'(\vec{r},\vec{R},t)\rangle \tag{2.80}$$

where, E is the quasi-energy. The functional form $F'(\vec{r},\vec{R},t)$ is periodic in nature with periodicity T, so that it can be expanded in a form of Fourier series :

$$|F'(\vec{r},\vec{R},t)\rangle = \sum_{n=-\infty}^{n=+\infty} \exp^{-in\omega t} |F'_n(\vec{r},\vec{R})\rangle \tag{2.81}$$

and now the guess solution can be written as :

$$|\Psi(\vec{r},\vec{R},t)\rangle = \exp^{iEt/\hbar} \sum_{n=-\infty}^{n=+\infty} \exp^{-in\omega t} |F'_n(\vec{r},\vec{R})\rangle \tag{2.82}$$

which is also valid for quasi-energies E, $E \pm \hbar\omega$, $E \pm 2\hbar\omega$,..,$E \pm n\hbar\omega$. Putting this solution back in the time-dependent Schrödinger equation and doing further simplification, the time-dependent Schrödinger equation can be expressed as a set of time-independent differential equations, where the adjacent Fourier components are coupled together :

$$\left[E + n\hbar\omega - H_0(\vec{r},\vec{R})\right] |F'_n(\vec{r},\vec{R})\rangle = V_+ |F'_{n-1}(\vec{r},\vec{R})\rangle + V_- |F'_{n+1}(\vec{r},\vec{R})\rangle \tag{2.83}$$

The wavefunctions $|F'_n(\vec{r},\vec{R})\rangle$ serves as the eigenfunctions of field free *Hamiltonian* H_0 with a phase factor $\exp^{-in\omega t}$, which is termed as 'n'-photon dressed electronic state. Here, $V_\pm$ denotes the one photon coupling between the dressed electronic states. However, the coupling between the electronic states are only allowed for different symmetry according to the dipole selection rules.

For, simplest molecular system H_2^+, $|F'_n(\vec{r},\vec{R})\rangle$ can be replaced by eigenfunctions of $1\sigma_g$ and $1\sigma_u$ electronic states. The 'n'-photon dressed eigenfunctions of $1\sigma_g$ and $1\sigma_u$ electronic states can be represented as $|\phi_s(\vec{r},\vec{R})\rangle_{g,n}$ and $|\phi_s(\vec{r},\vec{R})\rangle_{u,n}$ respectively. In Figure-2.8a, 'dressed' states of hydrogen molecular ion are illustrated. These new potential energy curves are termed as *diabatic* potential curves. The above equation can

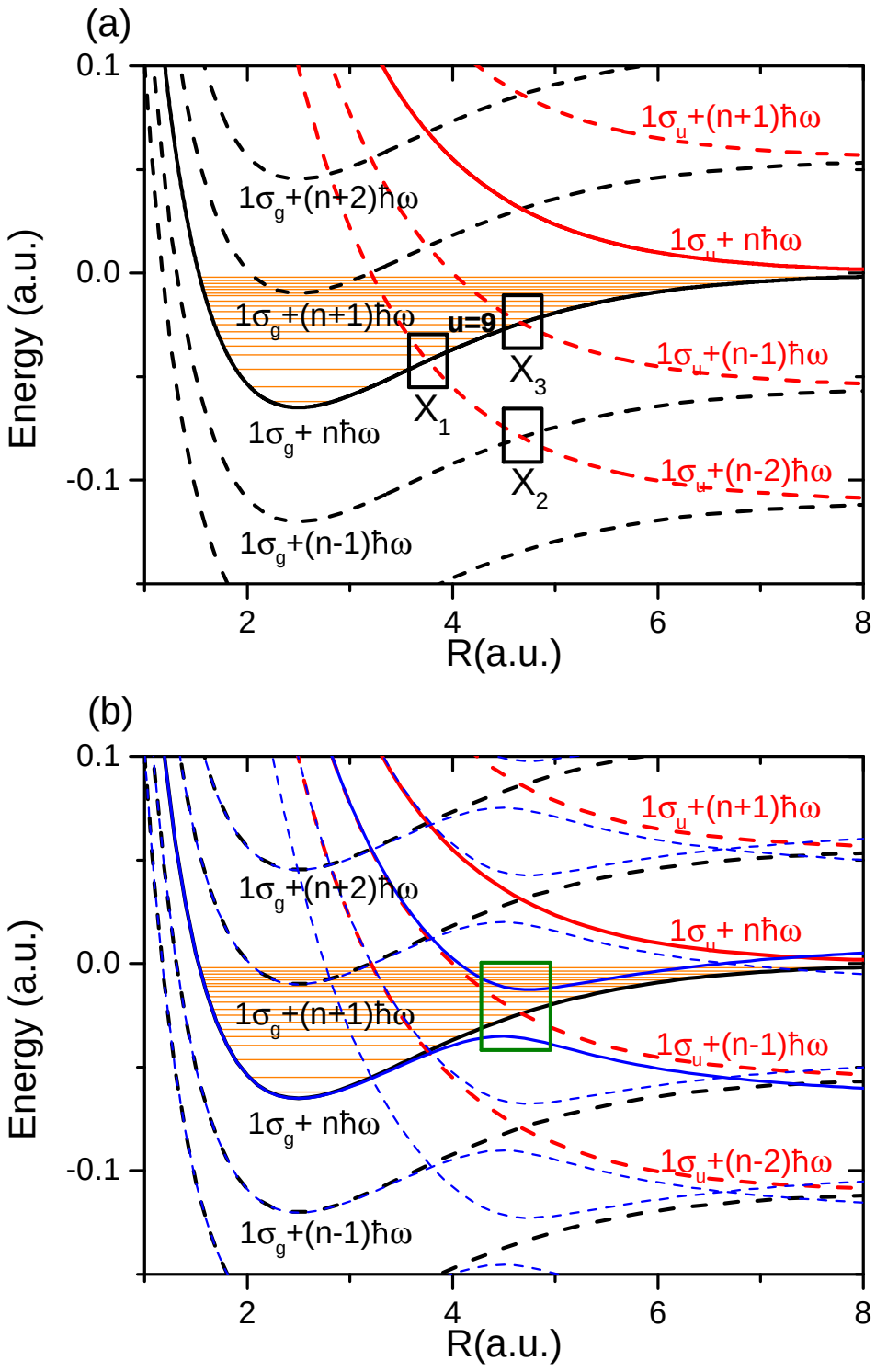

Fig. 2.8: (a)The potential energy curves (‘*diabatic*’ curves) of photon dressed $1\sigma_g$ and $1\sigma_u$ states are shown. The rectangles marked with X_1, X_2 and X_3 highlight the curve crossings. Based on dipole selection rule only X_2 and X_3 crossings are feasible. The horizontal lines depicts the field free vibrational energy levels. (b) The photon dressed ‘*diabatic*’ and ‘*adiabatic*’ curves for field strength $F_0 = 0.01$ a.u. are shown.

be rewritten for the hydrogen molecular ion in the following manner for possible one photon coupling between n and $n \pm 1$-photon dressed electronic states :

$$\left[E + n\hbar\omega - V_g(\vec{R})\right] |\phi_s(\vec{r},\vec{R})\rangle_{g,n} = V_+ |\phi_s(\vec{r},\vec{R})\rangle_{u,n-1} + V_- |\phi_s(\vec{r},\vec{R})\rangle_{u,n+1} \tag{2.84}$$

$$\left[E + (n+1)\hbar\omega - V_g(\vec{R})\right] |\phi_s(\vec{r},\vec{R})\rangle_{g,n+1} = V_+ |\phi_s(\vec{r},\vec{R})\rangle_{u,n} + V_- |\phi_s(\vec{r},\vec{R})\rangle_{u,n+2} \tag{2.85}$$

This infinite set of differential equations can be represented in a matrix formulation, which is known as Floquet matrix and the quasi-energy values can be obtained by diagonalizing the matrix

$$\begin{bmatrix}
 & . & . & . & . & \\
 & . & . & . & . & \\
 & . & . & . & . & \\
\ldots & V_{u,g}(\vec{R}) & 0 & 0 & 0 & \ldots \\
\ldots & V_u(\vec{R}) - (n-1)\hbar\omega & V_{u,g}(\vec{R}) & 0 & 0 & \ldots \\
\ldots & V_{g,u}(\vec{R}) & V_g(\vec{R}) - n\hbar\omega & V_{u,g}(\vec{R}) & 0 & \ldots \\
\ldots & 0 & V_{g,u}(\vec{R}) & V_u(\vec{R}) - (n+1)\hbar\omega & V_{u,g}(\vec{R}) & \ldots \\
\ldots & 0 & 0 & V_{g,u}(\vec{R}) & V_g(\vec{R}) - (n+2)\hbar\omega & \ldots \\
\ldots & 0 & 0 & 0 & V_{g,u}(\vec{R}) & \ldots \\
 & . & . & . & . & \\
 & . & . & . & . & \\
 & . & . & . & . &
\end{bmatrix} \tag{2.86}$$

where, n runs from $-\infty$ to $+\infty$ and

$$V_{u,g}(\vec{R}) = V_{g,u}(\vec{R}) = \langle 1\sigma_u | V_\pm | 1\sigma_g \rangle = \frac{F_0}{2} \langle 1\sigma_u | ez | 1\sigma_g \rangle \approx \frac{\hbar\omega_R}{2} \tag{2.87}$$

where, Rabi frequency ω_R.

This infinite Floquet matrix is usually truncated into a finite matrix for the practical scenario. For the smallest 2×2 Floquet block, the eigenvalues can be estimated easily

by solving the following equation for one photon coupling :

$$\begin{vmatrix} V_g(\vec{R}) - E & V_{u,g}(\vec{R}) \\ V_{g,u}(\vec{R}) & V_u(\vec{R}) - \hbar\omega - E \end{vmatrix} = 0 \tag{2.88}$$

In this case the associated photon number 'n' is approximated to zero. The estimated eigenvalues $E_{\pm}(\vec{R})$ is termed as *adiabatic* potential energy.

$$E_{\pm}(\vec{R}) = \frac{V_g(\vec{R}) + V_u(\vec{R}) - \hbar\omega}{2} \pm \frac{1}{2}\sqrt{\left[V_g(\vec{R}) + \hbar\omega - V_u(\vec{R})\right]^2 + (\hbar\omega)} \tag{2.89}$$

The *adiabatic* potential energies are shown in Figure-2.8b for different peak intensity values. For, field free condition the off diagonal terms are zero, i.e. $V_{u,g}(\vec{R}) = V_{g,u}(\vec{R}) = 0$ and the corresponding eigenvalues are actually the *diabatic* potential energies. These *diabatic* potential energy curves crosses each other at resonant internuclear separation $\vec{R} = X_2$, where the energy difference between $1\sigma_g$ and $1\sigma_u$ state is equal to one photon energy. In the presence of the laser field these curve crossings become avoided crossings between the *adiabatic* potential energy curves $E_{\pm}(\vec{R})$ with an energy gap proportional to the Rabi frequency.

2.3.2 Bond Softening and Bond Hardening

Figure-2.8a and b depict the *diabatic* and *adiabatic* potential energy curves for several photon coupling conditions. These photon coupled potential energy curves leads to various new dissociation phenomena in the presence of the laser field. After ionization, nuclear vibrational wavepackets are formed over either $1\sigma_g$ or $1\sigma_u$ state. As the $1\sigma_u$ state is repulsive in nature, the vibrational wavepackets escapes and eventually the hydrogen molecular ion dissociates into ionic and neutral fragments. Even though $1\sigma_g$ is a bound state, vibrational wavepackets created in this state can dissociate through various interesting processes depending upon the vibrational energy distribution with respect to the avoided crossings.

For the nuclear wavepackets with vibrational energy below the photon-resonant crossing could dissociate either via *adiabatic* potential curves or by tunnelling through

a small barrier due to avoided crossing. This phenomena is known as '*Bond Softening*' processes(10).

Nuclear wavepackets with higher vibrational energy above the photon-resonant crossing could be trapped in the upper photon induced potential energy curve. This mechanism is termed as '*Bond Hardening*' processes or molecular stabilization(11).

2.4 Laser Induced Rotational Dynamics

The another significant effect of interaction of molecules with intense laser field is charge redistribution over the molecular system in response to an external electric field and it is quantified by the polarizability of the molecule. In the presence of the laser field molecular system experiences a rotational torque due to the induced dipole moment of the molecular system. This phenomena aligns the molecule along the polarization axis. The molecular alignment depends upon several factors such as the peak intensity of the laser pulse, the pulse duration of the laser pulse and most importantly on the effective polarizability of the molecule, which is closely related to the electronic response of the molecule in the presence of the laser field. To make a quantitative correspondence with the molecular alignment a semi-classical model is introduced for a diatomic molecule, considering it as a non-rigid rotor. Now the interaction term in the Lagrangian due to the oscillating electric field $\vec{F}(t)$ and the polarizability $\vec{\mu}$ can be written as :

$$V(\theta) = \vec{\mu}.\vec{F}(t) \tag{2.90}$$

The polarizability term $\vec{\mu}$ can be expanded with Taylor series expansion in terms of the electric field $\vec{F}$ in the following manner :

$$\vec{\mu}(\vec{F}) = \vec{\mu}_0 + \frac{1}{2}\alpha.\vec{F} + ... \tag{2.91}$$

where the first term is the permanent dipole moment of the molecule and the second term is the dipole polarizability α, which is the response of the electrons of the molecule to the effect of the external oscillating electric field. The interaction term can be rewrit-

ten as:

$$V(\theta) = \vec{\mu}.\vec{F}(t) = \vec{\mu}_0.\vec{F} + \frac{1}{2}\alpha.\vec{F}\vec{F} + ... \tag{2.92}$$

and due to the oscillating laser field the first term averages out to zero over a complete optical cycles, however, the polarizability term survives. Neglecting all the higher order terms, the approximated interaction term is :

$$V(\theta) \approxeq \frac{1}{2}\alpha.F^2 \tag{2.93}$$

The complete *Lagrangian* for a non-rigid rotor in an electric field (cycle averaged) can be written as(65; 66):

$$L = \frac{1}{2}m\left(\dot{R}^2 + R^2\dot{\theta}^2\right) - V(R) - \alpha_{||}F^2(t)\cos^2\theta + \alpha_{\perp}F^2(t)\sin^2\theta \tag{2.94}$$

where, $V(R)$ is the electronic potential as a function of internuclear separation, which defines the dynamics of the nuclear wavepackets. $\alpha_{||}$ and $\alpha_{\perp}$ indicates the dipole polarizability of the diatomic molecule along the internuclear separation and perpendicular to it, respectively. The corresponding equation of motion for the radial and angular part can be written as (67; 68) :

$$m\ddot{R} = -\frac{dV(R)}{dR} \tag{2.95}$$

$$\ddot{\theta} = -\Delta\alpha\frac{F^2}{2I}\sin 2\theta - 2\frac{\dot{R}}{R}\dot{\theta} \tag{2.96}$$

The equation of motion for the angular rotation of the molecule contains one accelerating term and a damping term, the damping term leads to a reduced acceleration due to conservation of angular momentum as the two nuclei move apart. The accelerating term contains effective dipole polarizability, $\Delta\alpha = \alpha_{||} - \alpha_{\perp}$, and time dependent moment of inertia, however, the accelerating term reduces with increasing bond length. These coupled differential equations are needed to be solved to understand the molecular alignment quantitatively. Numerical methods are usually used to solve these equation to estimate the rotation of the molecule in the laser field.

2.5 Experimental Strategy

Till now we have seen how a molecular system interacts with intense laser field and as a consequence, the molecular system goes through ionization, which will cause dissociation of the molecular ion into several ionic and neutral fragments. However, the varying characteristics of the laser pulses can initiate a wide range of electronic processes which play a key role in the dissociation. One of the possible ways to understand the dissociation dynamics of a molecular system could be achieved by capturing these ionic fragments. For the ion detection techniques, kinetic energy distribution and the angular distribution of these ions with respect to the polarization axis are mainly required. The kinetic energy distribution of these ionic fragments helps to get an idea about the potential energy of excited states of the molecular ions. On the other hand, the angular distribution can reveal many pieces of information like the symmetry of the outermost molecular orbitals, symmetry properties of the participating electronic states, etc. under several valid approximations. In the following section, the possible ways to study various aspects of molecular dissociation dynamics are discussed thoroughly.

Intensity Variation

One of the most significant properties of the laser pulse that controls the ionization processes and molecular dissociation dynamics is the peak intensity of the laser pulse.

For NIR laser pulses varying the peak intensity systematically over $10^{11} - 10^{15}$ W/cm^2 range, one can observe the participation of various ionization processes in the formation of single to multi-electron dissociative ionization. The detected ionic fragments could indicate the charge state of the parent molecular ions. With the variation of the peak intensity of the laser pulse, one could expect change in the distribution of the final ionic fragments.

Photodissociation processes like *Bond Softening* and *Bond Hardening* are strongly dependent on the peak intensity of the laser pulse and the intensity variation could control these processes very effectively.(10; 11; 69; 70)

The intensity of the laser pulse induces dipole moment over the molecular system as a response of the electrons in the molecule. Variation of the peak intensity can control the alignment of the molecule with respect to the polarization axis(71; 72; 73; 74). The degree of alignment could be estimated by looking into the angular distribution of the ionic fragments as the ions produced in the dissociation process will move outward along the straight line defined by the internuclear axis of the molecule, known as the axial recoil approximation.

Wavelength Variation

The wavelength of the laser pulse is also a very important parameter to control the ionization and dissociation processes. Over a similar intensity regime, the variation of laser wavelength could initiate different dissociation channels and various electronic processes start to participate. The detection of kinetic energy distribution and angular distribution of the ionic fragments with respect to the polarization axis of the laser field could indicate the participation of possible dissociation channels with wavelength variation(75).

Time Resolved Experiments

The electronic processes govern the dissociation dynamics of a molecular system and the electronic processes like the transition between photon-coupled states occur in an ultrashort time scale ($<$ 100 fs) for most of the molecules. To understand such ultrafast dynamics of molecules in greater detail more careful time-resolved studies are required. The most common way to do time-resolved studies is by pump-probe experiments(76; 77; 78; 79; 80). Here a single pulse ionizes the molecule and creates vibrational wavepackets over some electronic state and then a second pulse is applied after the first pulse with some time delay to probe the nuclear dynamics over this specific excited state. The detected ionic fragments at each delay very clearly reflect the internal dynamics of the molecular system. A similar kind of information can also be obtained by stretching a single pulse over a wide range from femtosecond to picosecond regime

systematically(81; 82).

2.6 Summary

This chapter contains a brief discussion on molecular structures and various nuclear motions of a simple diatomic molecule. The main goal of this chapter is to understand the laser-molecule interaction in detail. In this chapter, various photoionization mechanisms are discussed. The Keldysh parameter (γ) is introduced to distinguish between multi-photon ($\gamma \gg 1$) and tunneling regimes ($\gamma \ll 1$). To understand the tunnel ionization of molecules the MO-ADK-model has been introduced and discussed thoroughly. The dissociation of the ionized molecular system in the presence of the intense laser field is highlighted in terms of Floquet representation. Another significant dynamical process, the molecular alignment in the presence of the laser field is also highlighted. At the end of this chapter, different experimental strategies to understand the photon-induced dissociation dynamics of a molecular system by fragment ion detection are discussed briefly.

CHAPTER 3

EXPERIMENTAL DETAILS: VELOCITY MAP ION IMAGING TECHNIQUE

3.1 Overview of the Ion Imaging Technique

One of the possible ways to understand the multi-electron dissociative ionization (83; 84) initiated by any kind of external perturbation could be achieved by capturing the fragmented ions. The main goal is to detect the complete kinematic information of the ionic fragments efficiently to obtain significant information about the dissociative ionization. Usually, for a multi-electron dissociative ionization of diatomic molecular system, two partner ionic fragments fly away with equal momentum in opposite directions in the center of mass frame. For a collection of such events, the velocity space can be visualized as a set of concentric spheres, which is known as *Newton sphere*. The photon-induced dissociative ionization process of a model diatomic molecule $AB + h\nu \rightarrow A^{p+} + B^{q+}$ creates two *Newton spheres* shown in Figure-3.1 assuming the ionic fragments emerging from a point source at (x,y,z) with $(\Delta x \sim 0, \Delta y \sim 0, \Delta z \sim 0)$ and with zero initial velocity distribution $(\Delta v_x \sim 0, \Delta v_y \sim 0, \Delta v_z \sim 0)$. The size of the *Newton spheres* is closely related to the kinetic energy of the ionic fragments. The kinetic energy distribution of the ionic fragments indicates the dynamics of the molecular ions over potential energy surfaces. Also, the event distribution on the surface of the *Newton spheres* with respect to the polarization axis of the laser field could reveal overwhelming information about the symmetry of the outermost molecular orbital under the axial recoil approximation. In the ion imaging method, *Newton spheres* of the ionic fragments are guided towards the time and position-sensitive detector with the help of electric fields. All the momentum components of the ionic fragments can be estimated from the time and position information. The momentum information helps to obtain the kinetic energy distribution and the angular distribution of these ionic fragments.

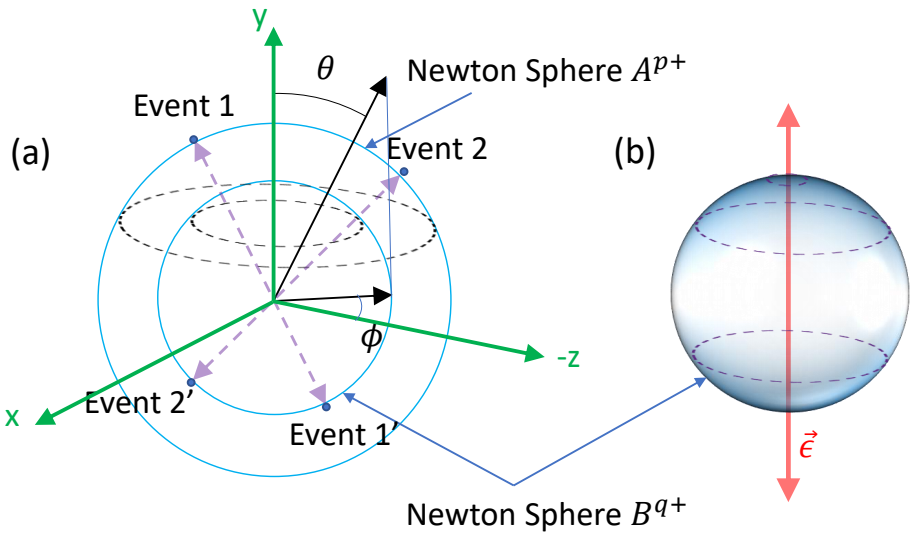

Fig. 3.1: (a)Two dissociation events and the associated pair of ionic fragments A^{p+} and B^{q+} are shown in velocity space. (b) Adding up a large number of events a spherical surface pattern is observed, which is known as *Newton sphere*. The *Newton sphere* of B^{q+} is shown here and it represents a typical $\cos^2\theta$ distribution with respect to the polarization axis.

For accurate detection of the *Newton spheres* of the ionic fragments, several experimental requirements need to be fulfilled. Obtaining accurate momentum distribution of ionic fragments requires a point source, however, in reality, the source is extended $(\Delta x \neq 0, \Delta y \neq 0, \Delta z \neq 0)$ over a few mm. The spread in the source position can blur the image of the *Newton sphere* on a position-sensitive detector. The blurring can also arise from the initial velocity spread $(\Delta v_x \neq 0, \Delta v_y \neq 0, \Delta v_z \neq 0)$ of the parent molecule due to the thermal energy. Compared to the dissociation energies of the ionic fragments the velocity spread at room temperature$(T \sim 300K)$, is negligible. The ion imaging quality can be improved by using several tricks with electrostatic lensing. In the following section, the details of the electrostatic lensing will be discussed to show how the ion imaging techniques are modified to capture the information of *Newton spheres* independent of the position spread of the source.

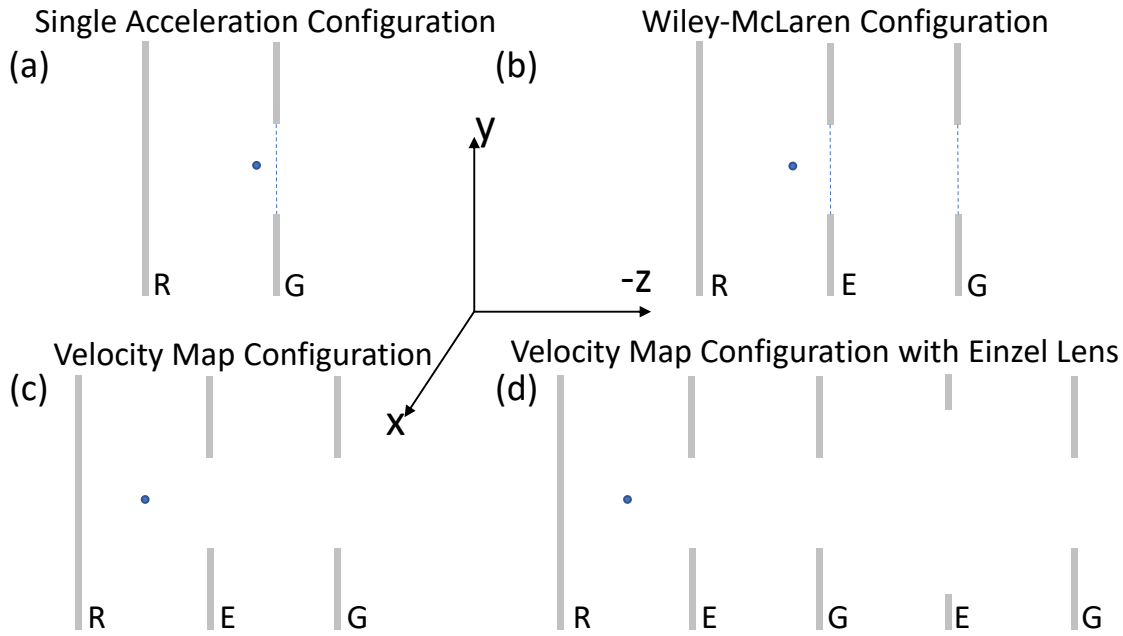

Fig. 3.2: The schematic of various ion-imaging configurations (a) single acceleration configuration, (b) Willy-McLaren configuration, (c) velocity map configuration and (d) velocity map configuration with einzel lens using several electrodes: Repeller (R), Extractor (E) and Ground (G) are shown. Most spectrometers have a field free drift region after G electrode but is not shown here.

3.2 Velocity Map Ion Imaging Techinque

In ion imaging, ionic fragments are guided towards the detector by applying an external electric field using several flat annular ring-type electrodes. To acquire a proper image of the *Newton sphere* by minimizing the effect of the extended source, electrostatic lensing should be adjusted properly. In the following section, the details of different electrostatic lensing conditions are discussed(22).

3.2.1 Electrostatic Lensing

Ion counting is widely used for mass spectroscopy, where the time-of-flight of the ions is detected using a timing detector. The time-of-flight depends upon the ratio of mass m to charge q of the ions as $\sqrt{m/q}$. On the whole, the mass resolution is closely related to the time spread of the time-of-flight spectrum. The time spread in the time-of-flight spectrum arises mostly due to extended ion sources along the time-of-flight

axis i.e. when $\Delta z \neq 0$. To improve the mass resolution Wiley and McLaren introduced a very special kind of field configuration(85) in 1955 for the first time. In the following years, several modifications are made to improve the ion imaging techniques. Figure-3.2 shows several electrostatic lens configurations used in ion imaging experiments.

Figure-3.2b shows the Wiley-McLaren type electrostatic lensing configuration, where three electrodes and a field-free drift region are used. Out of three electrodes, Repeller is a flat disk and the other two electrodes Extractor and Ground are flat annular ring-type electrodes covered with a fine mesh grid to form a homogeneous electric field along the time-of-flight axis. This configuration is optimized to achieve the space focusing condition, which ensures all the ions of the same mass arrive at the detector at the same time irrespective of the source point over the time-of-flight axis.

For the simplest single acceleration configuration (Figure-3.2a), the effective time jitter Δt due to extended source Δs_0 can be determined as :

$$\frac{\Delta t}{t} = \left(\frac{2s_0 - D}{4s_0 + 2D}\right).\frac{\Delta s_0}{s_0} \tag{3.1}$$

This time jitter can be completely eliminated for the space focusing condition $D = 2s_0$. For a Wiley-McLaren type electrostatic lensing configuration, electrodes are separated by $\sim$ 15 mm and the biasing voltages over Repeller (R), Extractor (E), and Ground (G) are (V_R) 5000 V, (V_E) 3000 V and (V_G) 0 V respectively. The drift tube length can be estimated from the Wiley-McLaren space focusing condition :

$$D = 2s_0 k_0^{3/2}\left(1 - \frac{d}{s_0}.\frac{1}{k_0 + \sqrt{k_0}}\right) \tag{3.2}$$

where,

$$k_0 = \left(\frac{s_0.V_R + d.V_E}{s_0.V_R}\right) \tag{3.3}$$

For the above biasing condition and the dimensions $s_0 = 7.5$ mm, $d = 15$ mm the drift tube length should be $D \sim 360$ mm. This is commonly known as Wiley-McLaren electrostatic lensing condition, which ensures the space focusing along the time-of-flight axis. A 2-Dimensional histogram of time-of-flight and radius of specific ionic fragments obtained from the time-of-flight and position information forms half-ring-

like structures and each half-ring structures map out ion hits with the same kinetic energy.

Figure-3.2c shows the electrodes in velocity map imaging configuration(23; 34), where the fine mesh grids are removed from the electrodes. The velocity map imaging configuration exhibits similar acceleration properties as the Wiley-McLaren configuration except for the lensing property. This lensing effect influences the ion trajectories in such a way so that ions with initial velocity components $(v_x, v_y, |v_z|)$ falls at the same point on the detector, irrespective of their formation in the x-y plane within a certain $\Delta x_0, \Delta y_0$. A weak smearing effect is usually observed for the extended sources along the z-axis. The importance of the velocity map imaging technique is the unique ability to map the velocity on the detector for an extended source $(\Delta x \neq 0, \Delta y \neq 0, \Delta z \neq 0)$. In the year 1998, for the first time, Eppink and Parker came up with this unique velocity map imaging technique, which can map the entire *Newton sphere* of the ionic fragments over a 2-Dimensional detector(23). These velocity map imaging spectrometers are widely used to study various kinds of laser-induced molecular dissociation processes. The velocity map images can be further magnified by putting an Einzel lens after the velocity map imaging lenses. A typical Einzel lens configuration having an annular ring electrode with biasing voltage V_E is placed in between two grounded annular ring electrodes after the velocity map imaging lenses. This configuration is shown in Figure-3.2d. Vrakking *et al.* introduced such Einzel lens configuration to magnify the velocity map images up to $\sim$20 times(86).

In this thesis work, a velocity map imaging spectrometer is used. The design of the spectrometer is derived from the classic Eppink and Parker instrument using three electrodes with a drift tube(87). In this current form, the extractor plate has a central $\sim$250 μm hole which is coupled to the gas line to form the effusive jet into the interaction region. The repeller plate is placed at a distance of $\sim$22 mm from the extractor to form the extraction region. The extractor has an opening of $\sim$25 mm and is followed by the ground plate with a gap of $\sim$22 mm having an aperture of $\sim$35 mm. All the plates have an outer diameter of $\sim$80 mm and a thickness of $\sim$5 mm. The deviation from the flat field lines close to the central axis near the apertures of the electrodes leads to the lens-

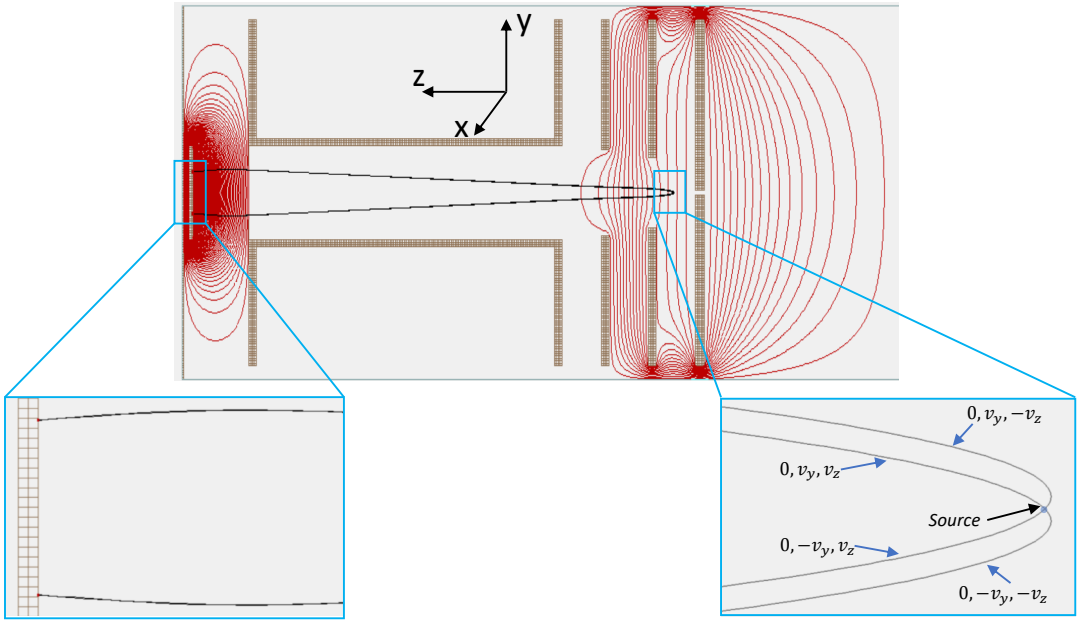

Fig. 3.3: Simulated ion trajectories of charged particles with initial velocity components $(0, \pm v_y, \pm v_z)$ for the velocity map configuration shows the ion focusing on the planar detector.

ing effect as seen from the figure, which focuses ions at the imaging plane. The outer and inner diameter of the rings is designed in such a way that the fringe fields caused by the finite electrode size, do not penetrate inside. The acceleration region leads to a drift region terminated at the exit by a nickel mesh with 95 % optical transparency. The $\sim$170 mm drift tube has a clear aperture of $\sim$40 mm throughout. The velocity focussed ions from the interaction region are designed to be imaged on a $\sim$40 mm diameter position-sensitive detector.

The focusing condition for the above-mentioned geometry for the positively charged particles was simulated using SIMION 8.0 (Scientific Instrument Services, Inc. USA). We considered a source of O^+ ions located on the axis at a distance of $\sim$262 mm from the detector at the central point between the extractor and repeller plate. The spatial spread of the ions was taken to be 4 mm $\times$ 4 mm in the plane perpendicular to the spectrometer axis with 0.4 mm extension along the spectrometer axis. For a voltage configuration of 645 V and 478 V on the extractor and repeller plate respectively, the focussing of velocity components $(0, v_y, v_z)$ is shown in Figure-3.3. Ion trajectories with initial velocity component $(0, v_y, 0)$ from an extended source of 0.4 mm$\times$ 4 mm in the

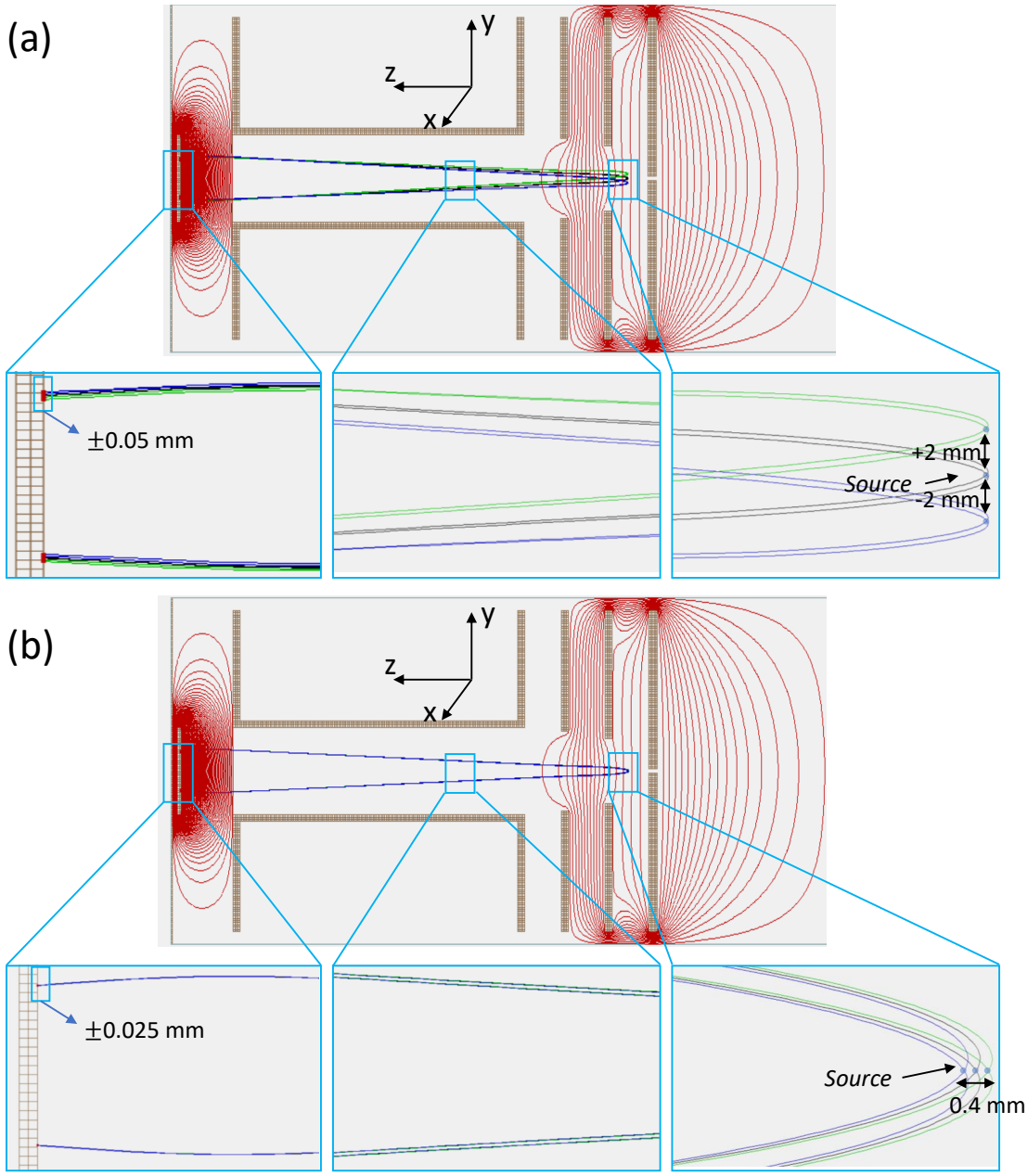

Fig. 3.4: Simultated ion trajectorices of charged particles with initial velocity components $(0, \pm v_y, \pm v_z)$ for the velocity map configuration for a wide source about (a) ~ 4 mm along y-axis and (b) ~ 0.4 mm along z-axis. Under this biasing condition of 645 V/478 V ions are mapped within ± 0.05 mm and ± 0.025 mm due to vertical spread of ~ 4 mm and horizontal spread of ~ 0.4 mm respectively.

(z-y) plane is shown in Figure-3.4. These ion trajectories confirm that for this voltage configuration the velocity components are mapped at the same point (with $\sim$ 0.02 mm ($\sim$20 μm) of variation) on a 2-Dimensional detector independent of the source position. However, for other voltage settings, the focusing conditions can also be achieved, but to obtain, an ideal focusing condition for this ion spectrometer the biasing voltage ratio (V_E/V_R) should be 0.74$\pm$0.01.

3.2.2 Detection Technique

The *Newton spheres* of the ionic fragments created at the source due to the laser-molecule interaction can be successfully guided to the detector by using proper electrostatic lensing with velocity map imaging conditions. The complete information of the *Newton spheres* could be obtained from the spatial 2-Dimensional image by applying several reconstruction methods. So, the accuracy of the estimated kinetic energy distribution and angular distribution strongly depends upon the quality of the spatial detection system. In this thesis work, we have used a $\sim$ 40 mm position sensitive detector comprising of a set of Micro-Channel Plates (MCP) and Delay Line Anode(DLD) made by Roentdek Handels GmbH, Germany. The details of the MCP and DLD are discussed in the following section.

Micro-Channel Plate

Micro-Channel Plates are the most sophisticated detectors used for single charged particle or photon detection. Micro-Channel Plates are consist of several millions of micro-channels and each of the micro-channels has a typical radius of $\sim$ 10–40 μm and a length of about $\sim$ 1.5 mm. The inner surface of individual channels is coated with a semiconductor material, which serves as a source of secondary electrons when a charged particle/photon hits the inner surface. So, each microchannel works as an electron multiplier tube. The microchannel plates are biased with a high electric field ($\sim$1 kV/mm) to enhance the production of secondary electrons. These electron multiplier tubes are usually inclined to the MCP surface to increase the gain. Most of the time

Typical performance of MCPs:	
temporal resolution :	$\leq$ 0.2 ns
rate capability :	$\sim$ 1 MHz
multi-hit dead time :	$\sim$ 10-20 ns
Typical characteristics of MCPs:	
Number of MCPs in stack :	2
Outer Diameter :	50 mm
Active Diameter :	40 mm
Thickness :	1-1.5 mm
Channel size :	25 μm
Center-to-center spacing :	32 μm
Bias Angle :	$8^{\circ} \pm 1^{\circ}$
Open Area Ratio :	$\geq$ 50 %

Table 3.1: The typical performace and the characteristic of a $\sim$ 40 mm MCP detector is listed here.

stack of two to three MCPs is used for better performance. Finally, the cloud of $\sim 10^6$ electrons emerges from the rear side of each microchannel. It makes the microchannel plate a special detector in which the amplified signal (the electron cloud) is localized to a tiny channel and the presence of a large number of channels over a larger area that operate independently. So, it can be used for a single charged particle/photon imaging. Also, due to the tiny size of each individual electron multiplier tube, the timing of the charged particle/photon hit can be determined very accurately with a precision of better than 100 psec. The typical performance and the characteristic of the MCP detector used in our experiments are listed in the following Table-1(29).

After the formation of well-localized electron clouds at the backside of the microchannel plate detector, the position encoding is performed in the second stage. There are several methods like-charged coupled device, the wedge, and strip anode, delay line anode to assign the coordinate of the centroid of the electron cloud. However, in our experiment, we have used a delay line anode (DLD) due to various unique features like high position resolution over a large area, fast read-out, and the best multi-hit detection ability above all. The principle of the DLD detector is discussed in the following section.

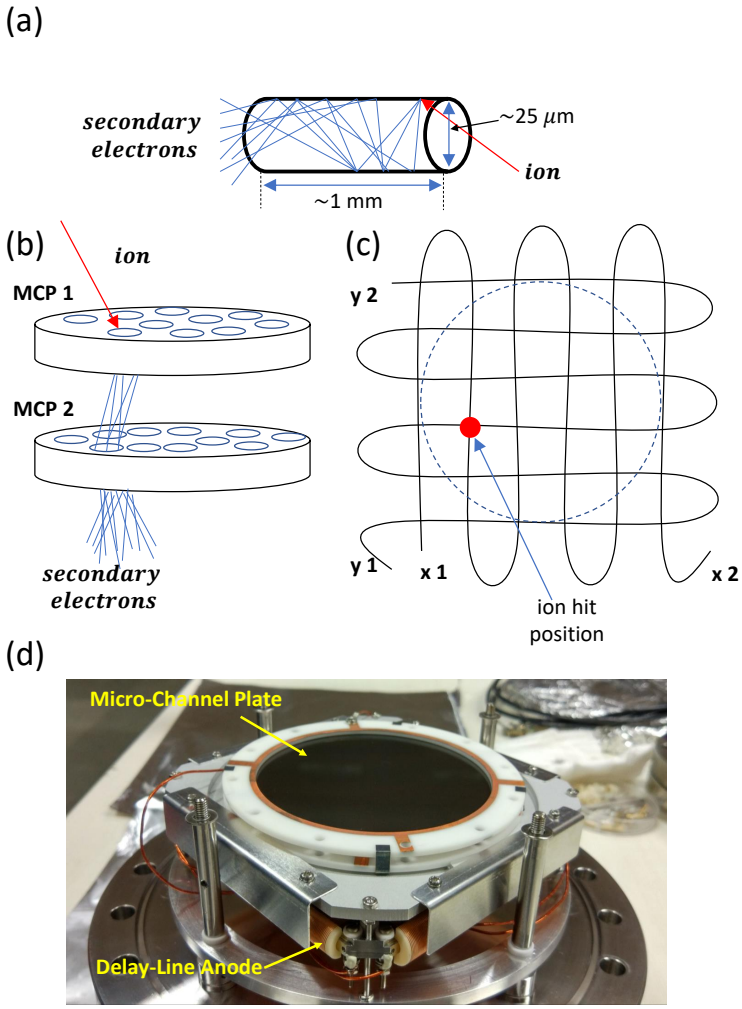

Fig. 3.5: (a) and (b): Schematic representation of secondary electron formation inside a micro-channel and through a stacked MCP. (c) Encoding the position of ion hit (red dot) using a delay line anode system. (d) Actual MCP+DLD detector system.

Delay Line Anode

The delay-line is made of a bare copper wire continuously wound without contact between successive turns across the opposite edges of an insulating plate. Two mechanically crossed, but electrically isolated pairs of delay lines form a 2-Dimensional grid with an equal spacing ($\sim$ 250 μm) and which can give the x and y coordinates of the electron shower. The electron clouds formed at the back of the MCP detector hit the delay line anode and it causes image charge pulses to propagate over the pair of copper wires to the end, which gives rise to four signals for each hit of the charged particles.

The position (x, y) can be obtained from the time difference of the signals detected at the end of each delay line in the following manner :

$$x = (t_{x1} - t_{x2}) \times v_{signal} \tag{3.4}$$

$$y = (t_{y1} - t_{y2}) \times v_{signal} \tag{3.5}$$

here, v_{signal} indicates the speed of the signal propagating through the bare copper wires, which is close to the speed of light. Since the length of the copper wire is constant, the total propagation time $(t_{x1} + t_{x2})$ and $(t_{y1} + t_{y2})$ are also constant for a given delay line irrespective of the source position. This information can be used as a cross-check for separating true ion hits from the background noise.

Signal Processing

To obtain all the ion hit signals with equal efficiency the microchannel plate detector should be used in the constant gain region (≥ -3.5 kV). However, we have biased the MCP front with -2.9 kV, which is slightly lesser than the constant gain region to avoid any kind of damage due to small discharges near the MCP front. Under this biasing condition, the measured value of the timing pulse has a width of ~ 1 ns and an amplitude of ~ 15 mV.

The DLD should be kept at a positive potential with respect to the potential of the MCP backside to extract the four signals from the DLD. During the experiment, the DLD is usually kept at ~ 250 V potential difference with respect to the MCP back. A decoupler unit having a RC circuit is used to extract the primary signals from MCP and DLD units. The primary signals are further amplified and converted into NIM signals through the ATR unit provided by the manufacturer. The five output NIM signals are further fed to multi-channel time to digital converter (TDC)(31).

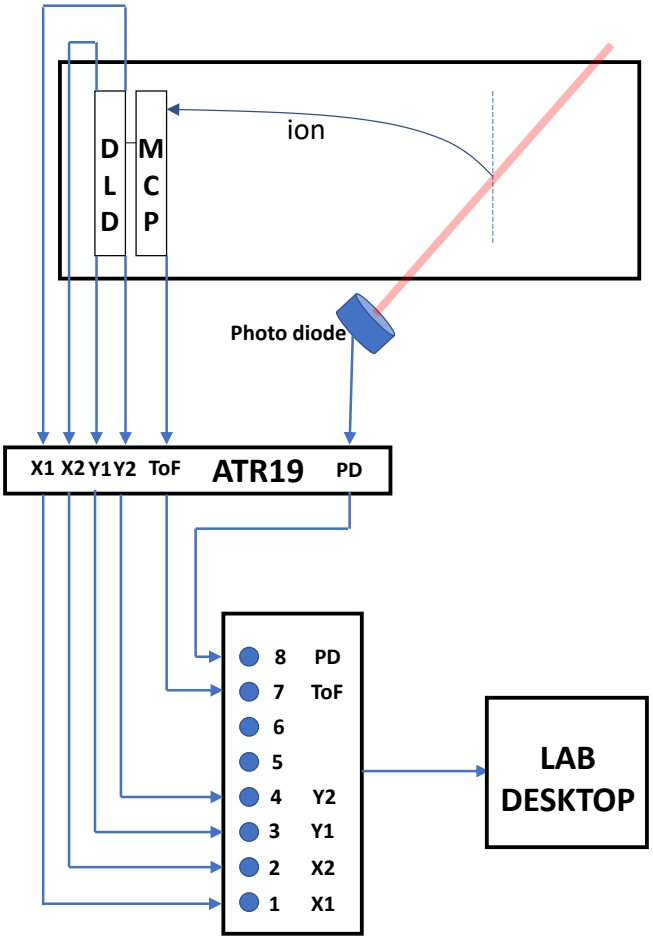

Fig. 3.6: The complete data acquisition scheme.

List Mode Data Acquisition and Multi-hit Coincidence

The data acquisition for ion imaging purposes requires six timing signals. Ion imaging experiments with a pulsed laser source uses photodiode (DET10A, Thorlabs, USA) signal as the start signal for every event, triggering the other five channels of the TDC from one MCP and four DLD timing signals. First, four channels of the TDC are associated with the four DLD signals and the fifth channel is directly from the ion MCP signal. The TDC has a time resolution of $\sim$ 500 ps with a range of $\sim$32 μs. However, for the multi-hit condition, the TDC automatically stops after four ion hits are detected within $\sim$32 μs.

Under the multi-hit condition, more than one ionic species arising from a single

Event number	Ion-1	Ion-2
...	...	...
51	$(t,x,y)_{51,1}$	-
52	$(t,x,y)_{52,1}$	$(t,x,y)_{52,2}$
53	$(t,x,y)_{53,1}$	$(t,x,y)_{53,2}$
54	$(t,x,y)_{54,1}$	-
55	$(t,x,y)_{55,1}$	$(t,x,y)_{55,2}$
56	$(t,x,y)_{56,1}$	-
57	$(t,x,y)_{57,1}$	-
...	...	...

Table 3.2: The schematic of the event list storing the time and position information of detected ion species arising from each event.

dissociation event can be detected. It has an immense impact on the studies of molecular dissociation dynamics. For example, let us assume a simple molecular system AB ionizes to form monocations and dications at a certain intensity regime. These monocations and dications can be unstable and dissociate into ionic and neutral fragments through several dissociation channels as shown in the following :

$$AB + h\nu \rightarrow AB^{+} \rightarrow A + B^{+}$$

$$AB + h\nu \rightarrow AB^{+} \rightarrow A^{+} + B$$

$$AB + h\nu \rightarrow AB^{2+} \rightarrow A + B^{2+}$$

$$AB + h\nu \rightarrow AB^{2+} \rightarrow A^{2+} + B$$

$$AB + h\nu \rightarrow AB^{2+} \rightarrow A^{+} + B^{+}$$

These fragmentation channels indicate the formation of similar ion products from monocation and dication. It is not possible to uniquely identify the fragmentation channels only from the time-of-flight spectrum. Under the multi-hit detection technique, simultaneous detection of multiple ions is possible. Fragmentation events involving two ions in coincidence can be visualized by plotting a 2-Dimensional histogram of time-of-flight spectrum of the ion species hitting first and second on the detector and hence one can identify the Coulomb explosion channel $AB + h\nu \rightarrow AB^{2+} \rightarrow A^{+} + B^{+}$ unambiguously. The digitized outputs of the MCP and DLD channels are read event by event and stored in a list format. The list-mode data acquisition has significant importance in multi-ion

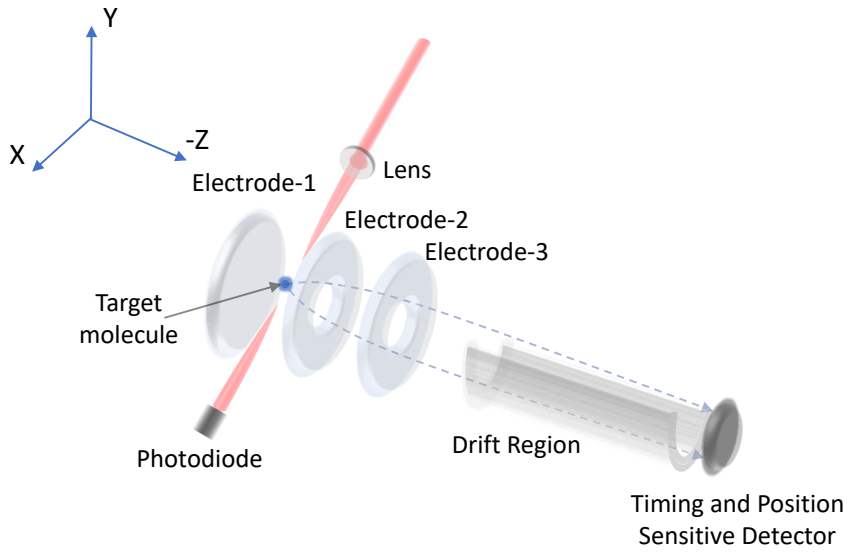

Fig. 3.7: Schematic of the experimental set up used to study photo-induced molecular fragmentation processes using velocity map imaging technique.

coincidence measurements due to its clean storage format. A program CoboldPC (Computer Based Online-offline List mode Data Analyser), written in MS Visual C++ works as PC interface of the TDC. This program is also used for offline data analysis after acquisition. This program is also used to do complex calculations, transformations, conditional sorting, histogramming events, etc. and displaying the processed data.

Experimental Set-Up

The designed spectrometer was implemented with non-magnetic components and housed in a non-magnetic stainless steel chamber which is pumped by a 350 l/s pumping speed turbomolecular pump. The ultimate vacuum achieved in the chamber is 1×10^{-8} mbar, with no gas load. With the effusive gas jet, the operating pressure was under 1×10^{-7} mbar.

The Femtopower V (Spectra-Physics, Austria) generates 25 fs, 1kHz, 5 mJ pulses at 800 nm, of which some energy is used to generate around 35 mJ of 400 nm pulses using Second Harmonic Generation by a 0.5 mm thick KDP crystal. Appropriate filters were used to separate the remnant fundamental laser radiation. The polarisation of the laser

beam is linear and is set perpendicular to the spectrometer axis using a thin $\lambda/2$ plate to operate in imaging mode. A lens of f = 30 cm is used to focus the laser to a measured spot size of FWHM radius of $\sim$100 μm leading to a peak intensity of 1×10^{13} W/cm^2.

3.2.3 Conversion Methods

Figure-3.8c, and d shows a projection of the 3-Dimensional *Newton spheres* over a 2-Dimensional detector of fragmented I^+ and CH_3^+ ions respectively. However, to obtain the complete 3-Dimensional velocity information of the fragmented ions we need to rely on various reconstruction methods to reconstruct the 3-Dimensional velocity distribution from a 2-Dimensional position image.

Usually, three different approaches are taken for converting a projected 2-Dimensional position image to a central 2-Dimensional slice of the 3-Dimensional *Newton spheres*: a) inversion methods(88; 89), b) forward convolution methods(90; 91), c) time-slicing methods(87). Inversion methods exploit the fact that if the primary 3-Dimensional distribution has an axis of cylindrical symmetry parallel to its 2-Dimensional projection then the complete 3-Dimensional information can be reconstructed. For laser-induced molecular dissociation processes, the ionic fragments are ejected with cylindrical symmetry about the laser polarization axis, which is parallel to the 2-Dimensional detector plane. Using Abel transformation, the 3-Dimensional velocity can be recovered from its projection over the 2-Dimensional detector. However, if for some experiments there exists no cylindrical symmetry, forward convolution methods are necessary. In forward convolution methods, 2-Dimensional images are constructed from a trial 3-Dimensional distribution and compared with the 2-Dimensional images obtained from the experiment. The trial distribution is iteratively adjusted to reconstruct a reasonable 2-Dimensional image. Further modification of this method is possible by the basis set expansion approach. In this way, the experimentally observed 2-Dimensional images are expanded in a set of basis functions, which are considered to be analytical projections of Gaussian-like well-behaved functions. The 3-Dimensional distribution can be reconstructed from the linear combination of these Gaussian-like functions. This method is known as the BASEX (BAsis Set EXpansion) method.

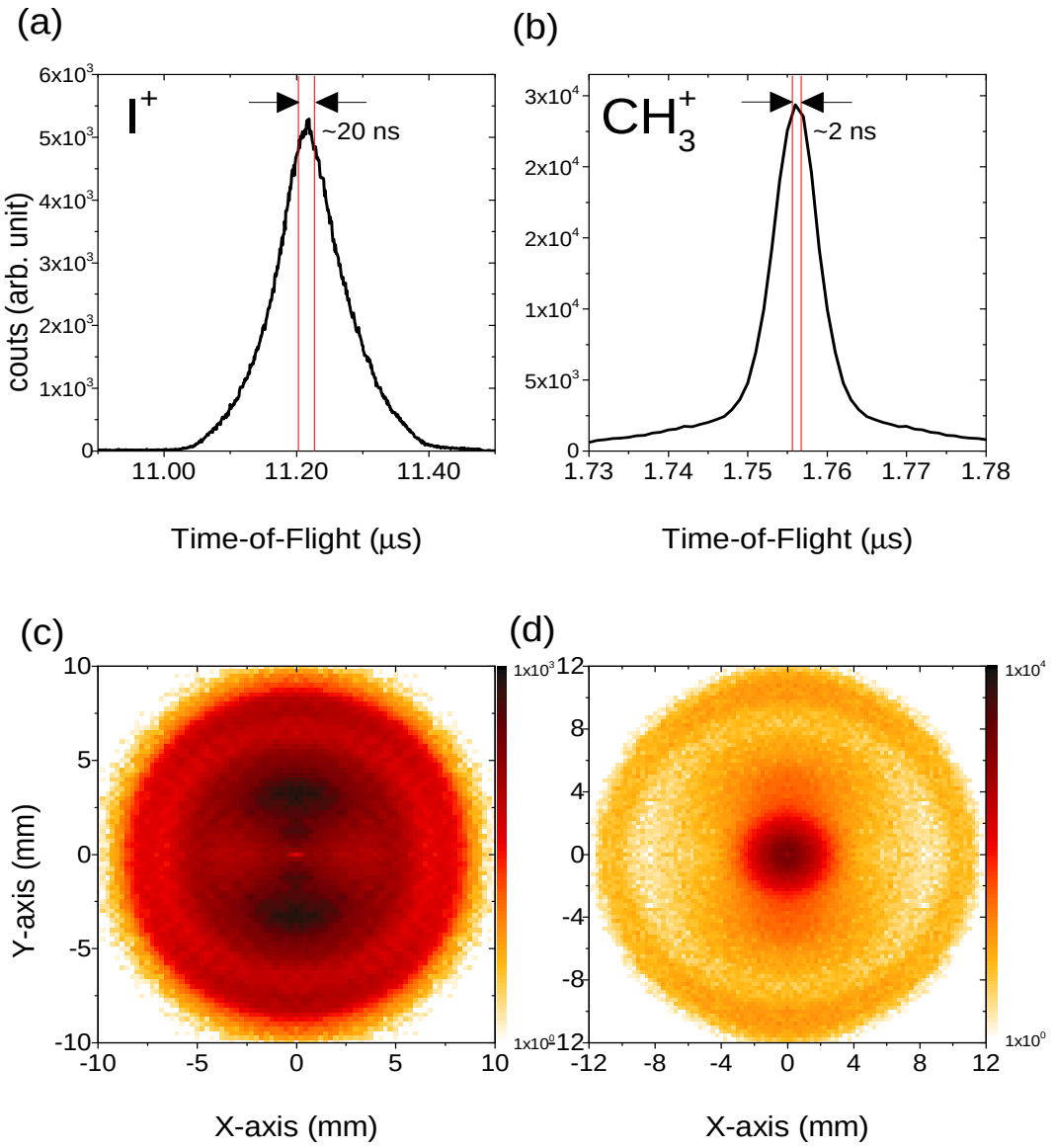

Fig. 3.8: The time of flight and postion spectrum of the fragmented I^+ ions are shown in (a) and (c) respectively. The time window to obatin the central slice of the *Newton spheres* is highlighted with red solid lines. Similarly CH_3^+ ions are shown in (b) and (d) respectively.

The time-slicing method, on the other hand, is a more direct way to get the entire 3-Dimensional velocity information from the 2-Dimensional projection of the *Newton spheres* by time gating in the post-processing of all the events, which only allows

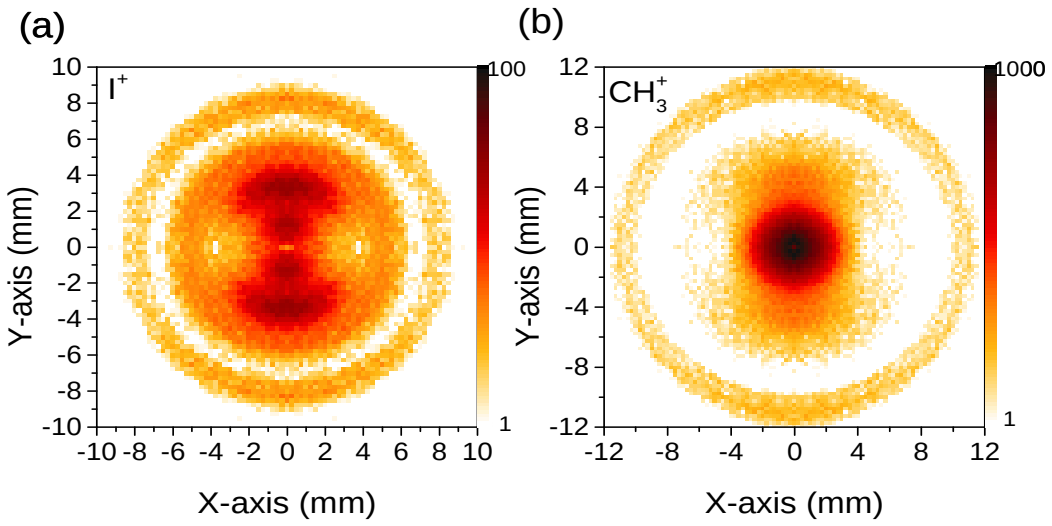

Fig. 3.9: Time sliced velocity map images of (a) I^+ and (b) CH_3^+

the ionic fragments with nearly zero v_z velocity components to be projected on the 2-Dimensional detector plane. In this thesis work, we have exclusively used this time-slicing method to extract the 3-Dimensional velocity information to avoid any kind of imposed approximation.

Figure-3.8a and b show the entire time-of-flight distribution of the I^+ and CH_3^+ ionic fragments under two different biasing conditions, respectively. The time-of-flight distribution of the ionic fragments contains the information of v_z velocity component and the 2-Dimensional position image contains the v_x and v_y velocity information. From the time-of-flight distribution, a narrow range has been selected with respect to the mean value and it indicates the events with nearly zero v_z velocity component. In the post-processing, the *x*-*y* position spectrum is generated for all the ionic fragments that fall in a narrow time-of-flight window with respect to the mean value and it will allow extracting the central slice of the 3-Dimensional *Newton spheres*. Usually, the time window for the time-slicing condition depends upon the ion species and biasing voltage conditions. In general, the time window of the central slice is only about ∼5% of the entire time-of-flight spectrum. For example, the time window for I^+ ion species is about ∼ 20 ns, whereas the time-of-flight spread of the ions is ∼ 200 ns. On the other hand, the

time window is only about $\sim$ 2 ns over a time-of-flight distribution of $\sim$50 ns for CH_3^+ ions.

Figure-3.9a and b show the time-sliced *Newton spheres* of the I^+ and CH_3^+ ionic fragments, which are known as *time-sliced velocity map images*. It shows several concentric annular structures which are associated with different kinematics. One can estimate the kinetic energy distribution of these ionic fragments by integrating the radial distribution of the counts over the 2π azimuthal angle as the radius of these concentric rings are proportional to the speed.To estimate the kinetic energy from the radial distribution for a given biasing condition of the spectrometer, calibration factors are needed to be calculated. In the following section, calibration technique is discussed in detail.

3.2.4 Calibration Technique

In the time-sliced velocity map images, concentric ring-like structures arise due to the variety of energy values corresponding to different dissociation kinematics. Fragmented ions with low kinetic energy come at the center and with increasing kinetic energy of the ionic fragments, the radius of the rings in the time-sliced velocity map images increases, however, the relation between ring radius and kinetic energy is non-linear. To obtain the calibration factor we have used SIMION to obtain the radius of the ion hit as a function of the initial energy. In the simulation, the ion source position is assumed to be on the axis at a distance of $\sim$262 mm from the detector at the central point between the extractor and repeller plate. The velocity components of the ions are considered as $(0, v_y, 0)$ for different energies, so that : $KE \approx 0.5 \times m \times v_y^2$. For two biasing conditions ($V_E, V_R \approx$ 2250,3000) and ($V_E, V_R \approx$ 478,645), ion energies are varied over a wide range with a small step size. Figure-3.10a and b shows a near quadratic dependence between radius and energy and has been fitted with a third-order quadratic function of the following manner :

$$E = aR + bR^2 + cR^3$$

Using these calibration factors, the kinetic energy distribution is generated from the

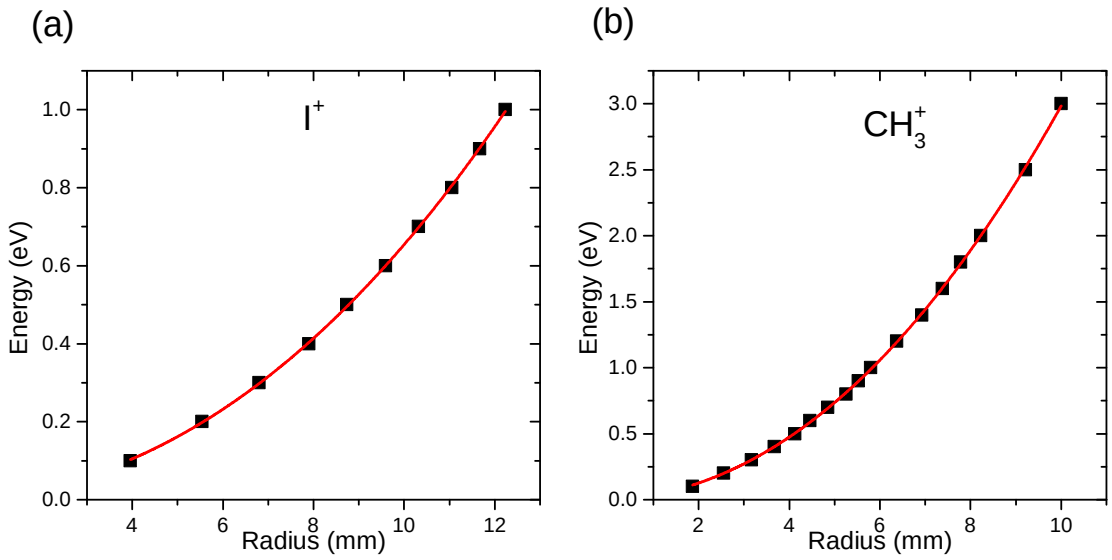

Fig. 3.10: Plot of the radius of the impacting ions on the detector as a function of the energy fitted using a third order quadratic function. (a) for $V_E, V_R \approx 478$ V, 645 V with coefficients $a = 0.00309$, $b = 0.00547$ and $c = 7.62337E-5$. (b) for $V_E, V_R \approx 2250$ V, 3000 V with coefficients $a = 0.01004$, $b = 0.02605$ and $c = 2.78529E-4$ for calibrating the images of I^+ and CH_3^+ fragments.

time-sliced velocity map images of CH_3^+ and I^+. The kinetic energy distributions of these ion species for two different biasing conditions are shown in Figure-3.13a and b respectively. We have used self-consistency checks to affirm the energy scale. In this procedure, we operated the spectrometer in a different way, where the polarisation axis of the laser field is aligned along the spectrometer axis. As the ion fragmentation in intense laser fields is preferential along the polarization axis, we have initially, equal energy products flying forwards and backward from the reaction point, with respect to the detector. While the extraction field turns around the backward components the difference in the time-of-flight between the two components yields the kinetic energy release (which depends upon the mass ratio of the fragmented ions). Processes with high kinetic energy release such as Coulomb explosion result in sharp peaks in the time-of-flight spectrum, symmetric with respect to the median time-of-flight, and are easily

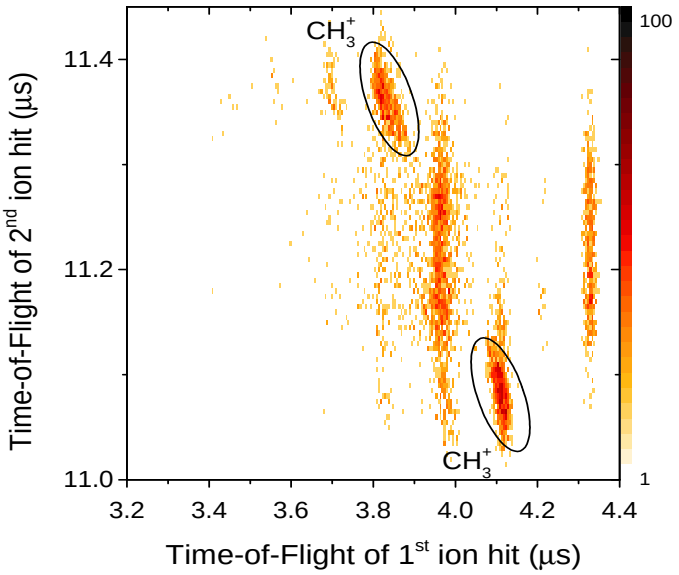

Fig. 3.11: Coincidence map of CH_3^+ and I^+ ions arising from Coulomb explosion events.

identifiable. Low energy dissociative products from different quantum states appear as kinks over a continuous background.

We studied the photo-fragmentation of Methyl Iodide (CH_3I) in moderate-intensity femtosecond laser pulses in a low extraction field, with the polarisation of the laser field parallel to the spectrometer axis. To unambiguously isolate the Coulomb Explosion events from dissociative fragmentation, the multi-hit acquisition was deployed, and a correlation plot between the first hit and the second hit was derived. Figure-3.11 highlights the islands corresponding to the coincident detection of the CH_3^+ and I^+ ions. To invert the time-of-flight spectrum and thereby to obtain the kinetic energy distribution, we have used the following relation to estimate the momentum components along the spectrometer axis(25):

$$\overrightarrow{p}_z = m \times 8.042 \times 10^{-3} . \frac{qU}{a} . \Delta T \hat{z} \tag{3.6}$$

where U is the acceleration potential over a distance a with respect to the reaction

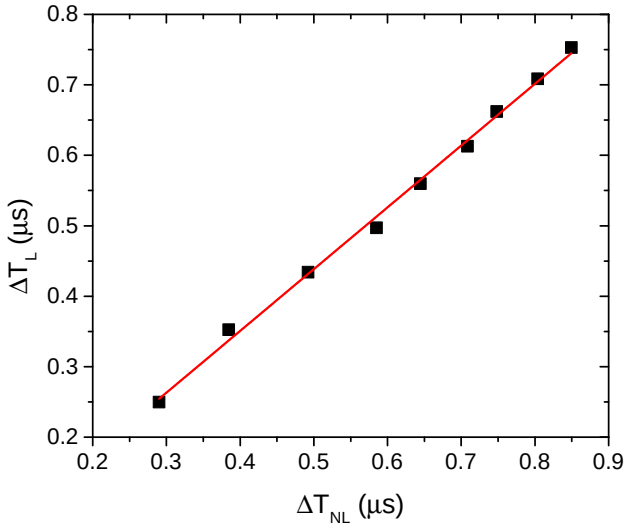

Fig. 3.12: The difference between the arrival times of the forward and backward emitted ions in the time of flight spectrum simulated for various initial energies of I^+ ions is calculated for two spectrometer configurations. The flight time difference for operation with lensing fields (ΔT_L) is compared against flight time difference for operation with a homogeneous, lensless fields (ΔT_{NL}). The estimated slope from the linear fitting is ~ 0.9

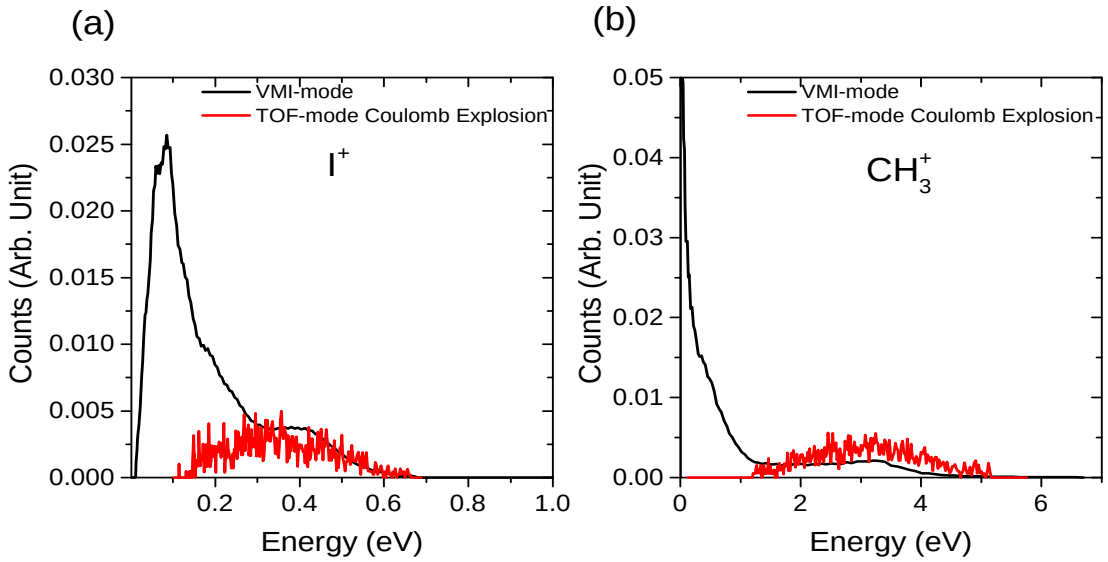

Fig. 3.13: The kinetic energy distribution of (a) I^+ and (b) CH_3^+ ions obtained from the time sliced velocity maps are shown in black. The kinetic energy distribution obtained from the time of flight spectrum of the ions arising in pairs from Coulomb expolsion are shown in red.

point. ΔT is the difference between the flight times of the ion with zero longitudinal momentum t_0 and the ion hit under consideration t. m is a multiplicative correction factor to account for the inhomogeneous lens fields(87; 92; 93). To obtain this factor, we simulated two cases. In the first case, the time-of-flight difference between the same energy ions flying in the opposite direction was obtained for different kinetic energies I^+ ions with the lensing fields present (ΔT_L). Second, each electrode was capped with meshes, simulating homogeneous, lensless fields, and the same forward-backward ToF difference was obtained (ΔT_{NL}). In the inset of Figure-3.12, the correlation between (ΔT_{NL}) and (ΔT_L) is plotted and a linear fit is evident. Keeping in mind that (ΔT_{NL}) represents the homogeneous fields for which the above equation is satisfied. We have used the slope of the above correlation ($m \approx 0.9$) as the multiplicative correction factor to invert the time-of-flight into the kinetic energy distribution. The kinetic energy distribution of the CH_3^+ and I^+ ions are plotted as black curves in Figure-3.13a and b.

While the full kinetic energy spectra contain dissociative fragmentation channels, the Coulomb explosion channel is indicated by arrows as the high kinetic energy shoulder in both spectra. The correspondence of the Coulomb explosion peak for kinetic energy spectra obtained in both methods is clear.

3.3 Summary

In this chapter, the basics of the velocity map imaging technique are discussed in detail along with the detection techniques, signal processing, and calibration technique. The introduced calibration technique offers a unique way where the energy calibration is performed through SIMION-based ion trajectory simulations and it has been tested against kinetic energy spectra obtained from coincident time-of-flight data alone. The method illustrated here does not rely on the existence of high-energy photon sources or calibration using electrons. Using this Velocity Map Imaging spectrometer we have thoroughly investigated the post-ionization dynamical processes happening over the excited electronic states of a molecule for two different molecular systems. To do so, we have taken two different experimental strategies. Firstly, we have used laser pulses with

two different wavelengths and varied the peak intensity over a similar range to show how the electronic properties of the electronic states participating in the dissociation process influence the dynamics of the molecular Oxygen ion. Secondly, we have varied the pulse duration of the laser pulses over a wide range by keeping the peak intensity constant to show the contribution of orbital rearrangement in the dissociation dynamics of the Methyl Iodide molecules. In the following chapters, we will highlight the results from these experiments, which show two different aspects of transient electronic processes which govern the dissociation dynamics of the molecule in the presence of the intense laser field.

CHAPTER 4

HINDERED ALIGNMENT IN ULTRASHORT, INTENSE LASER-INDUCED FRAGMENTATION OF O_2^+ MOLECULAR ION

4.1 Introduction

In an intense laser field, a molecule can be ionized via various ionization mechanisms like multiphoton ionization, tunnel ionization, over the barrier ionization, etc. In the intensity regime between 10^{13}–10^{15} W/cm^2 for a near-infrared laser pulses tunnel ionization is most dominant. The ionization occurs via tunneling through the potential barrier resulting from the combination of the external field and the mean-field of the nuclei. According to MO-ADK theory(36), in a quasi-static tunneling picture of strong-field molecular ionization, the ionization rate is maximum when the direction of the laser polarization axis is along the region having the highest probability of finding an electron. For example, the ionization rate of molecules having outermost orbital with σ symmetry is maximum when the molecular axis stays parallel to the polarization axis of the laser pulse, i.e. $\theta = 0^\circ$. The degree of alignment of molecules interacting with laser pulse could be mapped through dissociation processes of molecular ions under axial recoil approximation. Several ion imaging studies on molecules such as H_2, N_2 which have σ orbital symmetry in the outermost molecular orbital indicates the peaking of fragment ions H^+/N^+ along the polarization axis. However, the scenario changes for molecules with outermost orbitals having π symmetry. The ionization rate for molecules like O_2, having outermost orbital with π symmetry becomes maximum when the molecular axis is aligned at $\theta \sim 40^\circ$ with respect to the polarization axis. Ion imaging experiments on O_2 through O^+ ion detection point out the peaking of ion density at an angle about $\theta \sim 40^\circ$ with respect to the laser polarization axis(74; 95). However, in contrast to the

Coulomb Explosion of H_2^{2+} or N_2^{2+}, the angular distribution of the O^+ ions emerging from the Coulomb Explosion of O_2^{2+} ions shows a strong dependence with the peak intensity of the laser pulse. This alignment phenomenon observed in O_2^{2+} fragmentation in the presence of intense laser field is a direct manifestation of the rotational kick imparted to the molecular ion by the cycle averaged electric field of the laser pulse. Rotational kick depends upon both the specification of the laser pulse (i.e. peak intensity and pulse duration) and the molecular response to the external electric field of the laser pulse(67; 72). The charge distribution of a molecular system rearranges as a response to an external electric field and it is governed by the polarizability of the molecular system. The polarizability of a molecule manifests itself in the response to an intense laser field. The dipole polarizability of a molecular system is closely associated with the participating electronic state in the Coulomb Explosion process. A similar alignment effect could also be observed in the dissociation processes of a monocationic molecular system. However, the alignment of a monocationic molecular system could lead to very complex rotational dynamics due to the involvement of several electronic states in the dissociation process. To the best of our knowledge, no experiments have been performed to investigate the alignment effect in the monocationic molecular system as a response to the interacting laser pulse.

In this thesis work, we have studied the alignment effect through the dissociation of O_2^+ using a velocity map ion imaging spectrometer. To investigate the degree of alignment the intensity of the interacting near-infrared ($\sim$ 800 nm)laser pulse has been varied over a certain range systematically. To understand the electronic response in the alignment effect, the wavelength of the interacting laser pulse should be varied over a wide range. The interaction with laser pulses of different wavelengths could involve different electronic states in the dissociation process. The involvement of different electronic states could exhibit a different response to the external laser field, which could be inferred through the change in the angular distribution of the detected O^+ ions. Due to the unavailability of the Optical Parametric Amplifier (OPA), we have only been able to generate 400 nm pulses (rather than a broad range of tunable wavelengths) by second-order harmonic generation from the seed 800 nm pulse. The peak intensity of the 400 nm pulses is also varied over a wide range. We have compared the time-sliced

velocity map images of O^+ ions emerging from the dissociation of O_2^+ after interacting with 800 nm and 400 nm laser pulses. The degree of alignment of the O_2^+ ions is estimated from the observed angular distribution of the O^+ ions with respect to the polarization axis as a function of peak intensity. We have figured out the possible dissociation pathways of the O_2^+ ion based on the kinetic energy distribution of the ionic fragments and the available potential energy curves. The dipole polarizability of the participating electronic states is estimated with the help of a detailed quantum chemistry calculation. Using a simple classical model we had some success in explaining the degree of alignment of the O_2^+ ion observed for both wavelengths.

4.2 Experimental Details

In this section, experimental details are discussed thoroughly. A Femtopower V (Spectra-Physics, Austria) laser generates 25 fs, 1 kHz, and 5 mJ pulses at 800 nm. Part of the energy is used to produce 35 μJ of 400 nm pulses by second harmonic generation using a 0.5 mm thick KDP crystal (Eksma Optics, Lithuania). Appropriate filters are used to separate the remnant fundamental laser radiation. The polarization of the laser beam is linear and is set perpendicular to the spectrometer axis using a thin $\lambda/2$ plate (B-Halle, Germany). A thin f = 30 cm lens focuses the laser to a spot size (the diameter at half-maximum) of 70 μm, which is also used to estimate the peak intensity (I_0= 2.3×10^{13} W/cm^2). The pulse duration immediately after the laser amplifier is measured through autocorrelation and estimated at the spectrometer by accounting for dispersion along the beam path. The maximum intensity used for 800 nm is $4I_0$ and that for 400 nm is $3I_0$. These upper limits are chosen such that no O_2^{2+} is observed in the spectrometer. At the highest laser intensity used, the count rate for the parent molecular ion O_2^+ is kept below 1 kHz to rule out space charge effects by ions generated in the laser focal volume. Laser pulses are focused on an effusive jet of O_2 inside a vacuum chamber. An ion imaging spectrometer records the fragmented ions created by the laser pulse(87). The ion lens optics maps equivelocity ions of a given species (mass-to-charge ratio) to the same radius on a planar detector. The time and position information of each hit is

saved in the list mode format. Data were acquired for about 2 h at each experimental setting. In post-experiment processing, events with flight times close to the mean arrival time of the O^+ ions were selected, thus choosing ions with a nearly zero velocity component perpendicular to the laser polarization axis. These velocity slice images are presented in Figure-4.1a and b. Each position corresponds to a unique velocity of the ion, thereby allowing us to obtain a 2D map of the velocity distribution of the fragmented ions ejected in a plane containing the laser polarization axis. Since events lying on a circle centered on the 2D map correspond to ions having the same magnitude of velocity, the kinetic energy spectrum of the ions is readily obtained by integrating the counts over the azimuthal angle at each radius in the image. The Kinetic Energy Release (KER) spectrum can be further calculated since the momentum of the neutral O fragment is equal and opposite to that of O^+. The multi-hit capability of the detector is also exploited to check if there are any coincident O^+ ions recorded in the second hit. This allows us to establish that the ions recorded are from the dissociation channels (O^+/O) and not from any Coulomb explosion channel (O^+/O^+). The calibration of the spectrometer has been discussed in a previous paper.

4.3 Identification of Fragmentation Pathways

Figure-4.1a and b show the time-sliced velocity map of O^+ ions emerging from the dissociation of O_2^+ ions in the presence of a moderately intense laser field of wavelength 800 nm and 400 nm respectively. Two distinct ring-like structures are visible in both the time-sliced velocity maps. The ionic fragments over the outer ring carry higher kinetic energy as it is known that with increasing radius the energy of the fragmented ions increases. The density of the outer ring is not along the direction of the laser polarization axis and this is true for both wavelengths. However, this observation is not entirely unexpected, these 4-lobe structures could be closely associated with the π_g orbital symmetry of the outermost orbital of O_2. According to the MO-ADK theory, the molecular tunnel ionization rate is independent of the wavelength of the polarization axis but depends on the angle between the molecular axis and the laser polarization.

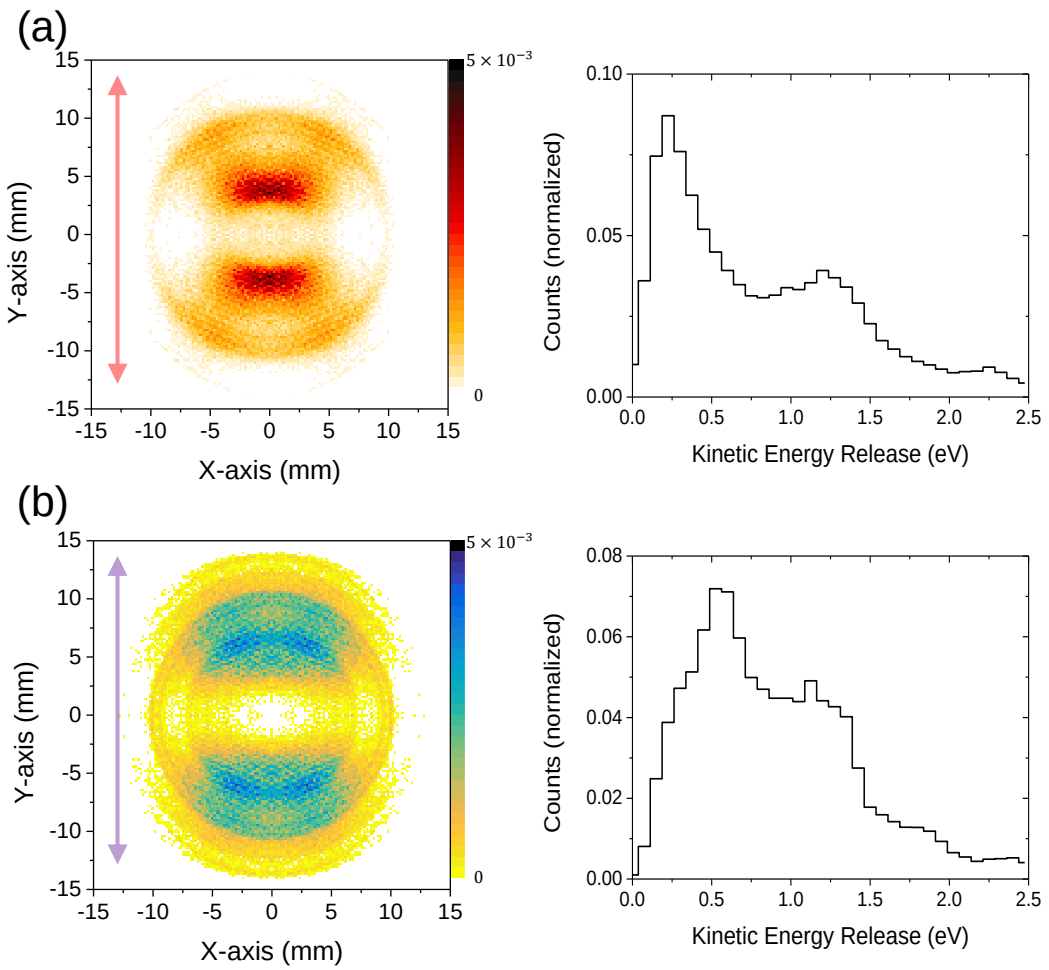

Fig. 4.1: The time sliced velocity map of O^+ ions emerging from the dissociation of O_2^+ ions in the presence of moderately intense laser field of wavelength (a) 800 nm and (b) 400 nm.

For this particular case, the ionization rate is maximum for O_2 molecules making $\sim 40^\circ$ angle with respect to the laser polarization axis. In the dissociation process, O_2^+ ions will move outward along the straight line defined by the internuclear axis of the molecule due to conservation linear momentum. Hence, the degree of alignment of the molecular ion is reflected in the time-sliced velocity map images for both wavelengths.

To establish the dissociation pathway for high-energy ions, we turn to the peak positions in the KER distribution, as illustrated in Figure-4.1. The outer ring in the fragment distribution map corresponds to a broad KER feature with mean energy 1.2 eV. In this low intensity regime $\sim 10^{12}$–10^{14} W/cm^2, the O_2^+ ions are mostly populated over $X^2\Pi_g$ and $a^4\Pi_u$ state. The kinetic energy release for different pathways can be

calculated very easily by the following equation

$$KER = E_{vib} - (E_D - n\hbar\omega) \tag{4.1}$$

where E_{vib} denotes the vibrational energy levels over the electronic states (for example either $X^2\Pi_g$ and $a^4\Pi_u$ state), E_D is the dissociation limit of the corresponding electronic state and the $n\hbar\omega$ indicates the energy shift due to the n photon dressing. Using this equation we have tried to calculate the KER for the pathways from the initial states $X^2\Pi_g$ and $a^4\Pi_u$ through the coupling of different photon-dressed states (see Chapter-2 for details). As the laser intensity is just at the threshold for dissociative ionization, we consider the only single-photon coupling between the O_2^+ ground state and the dissociative state. Molecular dipole selection rules mentioned in the following table restrict the states which can couple, thereby limiting the number of pathways to only a few.

Selection Rules	Example
$\Delta\Lambda = 0, \pm 1$	$\Sigma \Longleftrightarrow \Sigma$, $\Pi \Longleftrightarrow \Delta$,
Δ S = 0	$\Sigma^1 \Longleftrightarrow \Sigma^1$, $\Pi^3 \Longleftrightarrow \Pi^3$
g $\Longleftrightarrow$ u	$\Sigma_g^1 \Longleftrightarrow \Pi_u^1$
+ $\Longleftrightarrow$+ , or, - $\Longleftrightarrow$-	$\Sigma_g^{1+} \Longleftrightarrow \Pi_u^{1+}$

Table 4.1: Dipole selection rules with few simple examples

With these restrictions, the possibility of dissociative ionization by populating first the O_2^+ $X^2\Pi_g$ state, followed by coupling to a dissociative state of O_2^+ is ruled out. As Figure-4.4. shows the Frank-Condon population over the $X^2\Pi_g$ state is narrow and spread over only a few low lying vibrational states, so to get the KER of $\sim$ 1.5eV we have to introduce 5ω coupling to the $A^2\Pi_u$ state, which is very less likely in the intensity regime we have performed the experiment.

The O_2^+ $a^4\Pi_u$ is the next energetically available state. Ionization to this state, followed by a single-photon transition to a dissociative state is possible, giving the dissociation pathway for events with KER $\simeq$1.2 eV as O_2^+ $|a^4\Pi_u\rangle \rightarrow |1^4{\Sigma_g}^+ - 1\omega\rangle \rightarrow |1^4{\Sigma_u}^+ - 2\omega\rangle$, which is depicted in Figure-4.2.

We apply the same considerations in determining the pathway for the 400 nm case as in the case of 800 nm. The plausible pathway under 400 nm irradiation is O_2^+ $|a^4\Pi_u\rangle \rightarrow$

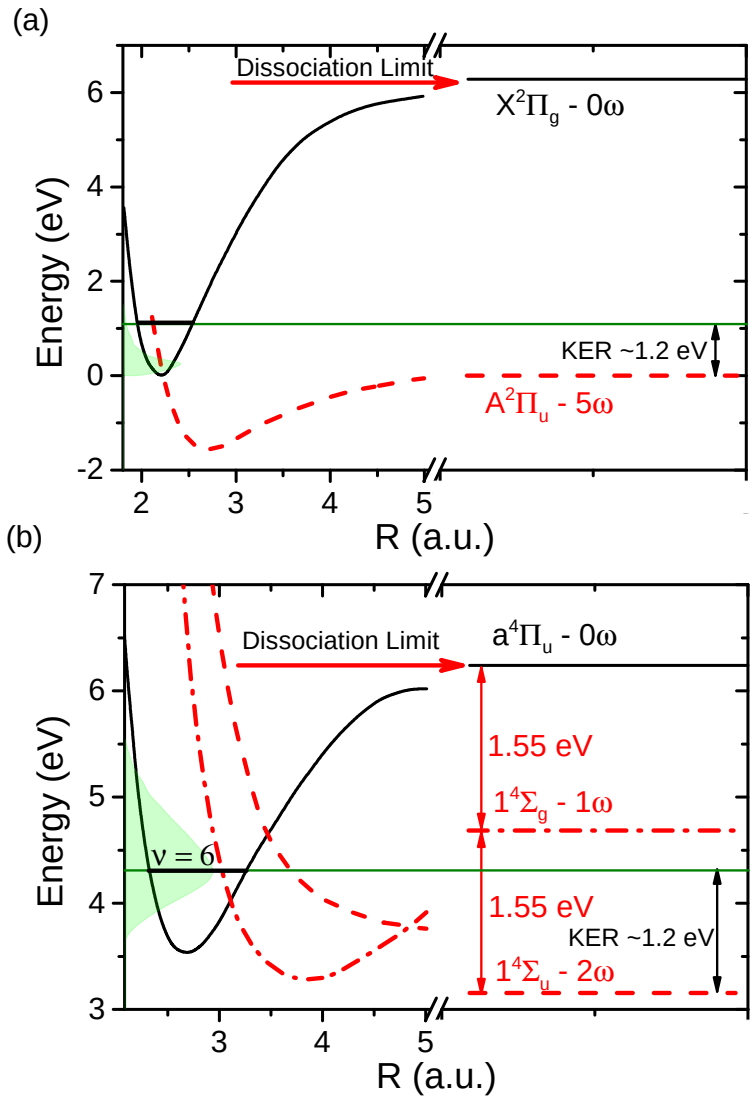

Fig. 4.2: Possible dissociation channels leading to higher kinetic energy relase via the (a) $X^2\Pi_g$ and (b) $a^4\Pi_u$ state in the presence of 800 nm pulses.

$|1^4\Sigma_g{}^+ - 1\omega\rangle$ for the KER peak at 1.1 eV (see Figure-4.3). With changing intensities, Stark effects also modulate the observed vibrational distributions. This could account for the shifting of the 1.1 eV peak towards 0.9 eV with increasing laser intensity in Figure-4.3. A similar shift is seen even for the 800 nm laser data. However, in the 400 nm case, this changing distribution would imply a larger contribution of this path-way to the low-energy ions. We have also analyzed the low energy ionic fragments, however, for O_2^+ fragmentation, a plethora of excited states can potentially contribute to the dissociation into low energy fragments. Also, the energy and angular resolution

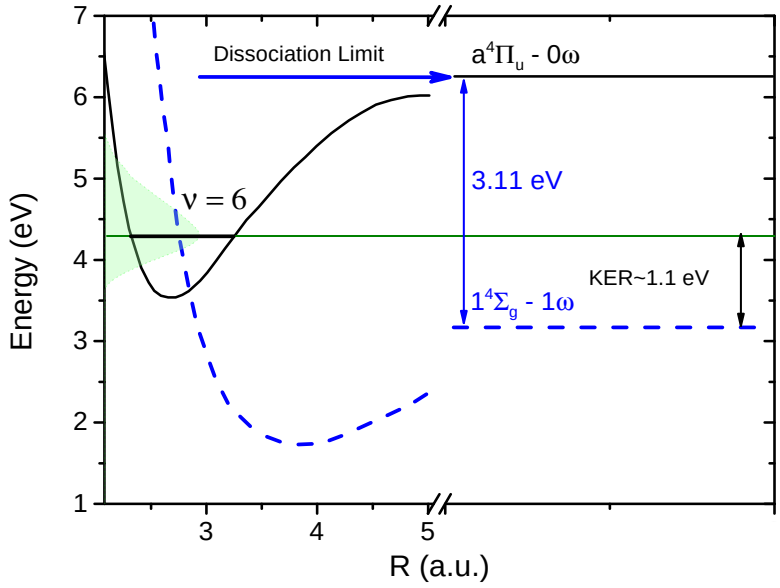

Fig. 4.3: Possible dissociation pathway for the higher kinetic energy fragments through $a^4\Pi_u$ state in the presence of 400 nm, 35 fs pulses.

of the spectrometer increases with radial distance along with the detector, so the low energy fragments will have low resolution. Figure-4.4 and 4.5 show possible dissociation channels for the low energy fragmentation through two different quartet parent ion states in the presence of 800nm and 400nm laser pulses respectively. As the energy and angular resolution for the low energy fragments is not adequate to resolve these dissociation channels, it would not be possible to draw a conclusion about the low energy fragmentation. A similar analysis for the low-energy ions is not straightforward. Multiple dissociation pathways can contribute to the prominent low-energy KER peak (0.25 eV) in Figure-4.4a and 4.4b. For example, again considering one photon mediated dissociation pathways alone, $|a^4\Pi_u\rangle \rightarrow |f^4\Pi_g - 1\omega\rangle$, $|b^4\Sigma_g^-\rangle \rightarrow |c^4\Sigma_u^- - 1\omega\rangle$ and $|b^4\Sigma_g^-\rangle \rightarrow |2^4\Pi_u - 1\omega\rangle$ are probable pathways which may contribute to the low energy peak at $\approx$0.25 eV. Dissociation through the ground state of O_2^+ through a.) $|X^2\Pi_g\rangle \rightarrow |A^2\Pi_u - 1\omega\rangle \rightarrow |^2\Sigma_g^+ - 2\omega\rangle$ or b.)$|X^2\Pi_g\rangle \rightarrow |^2\Sigma_u{}^+ - 1\omega\rangle \rightarrow |^2\Sigma_g^+ - 2\omega\rangle$ are also possible routes to the low energy ions. However, this requires that the higher vibrational states of $\upsilon \geq 16$ be populated in the FC transition in the ionization, which can be ruled out. Similarly, for 400 nm pulses the low lying KER channels of $\sim$0.5 eV could arise from several channels like a.) $|a^4\Pi_u\rangle \rightarrow |2^4\Pi_g - 1\omega\rangle$ b.) $|b^4\Sigma_g^-\rangle \rightarrow |3^4\Pi_u - 1\omega\rangle$

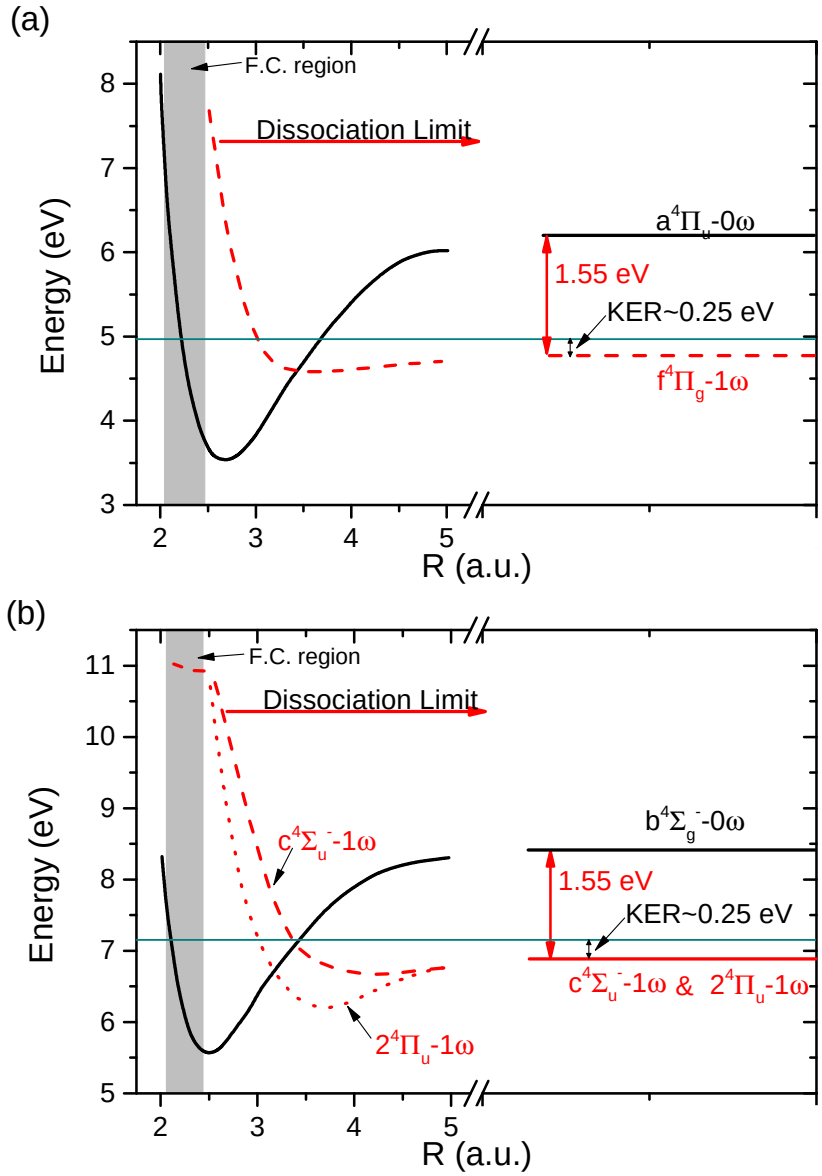

Fig. 4.4: Possible dissociation pathways for low energy fragments through (a) $a^4\Pi_u$ and (b) $b^4\Sigma_g^-$ parent ion states in the presence of 800nm laser pulse.

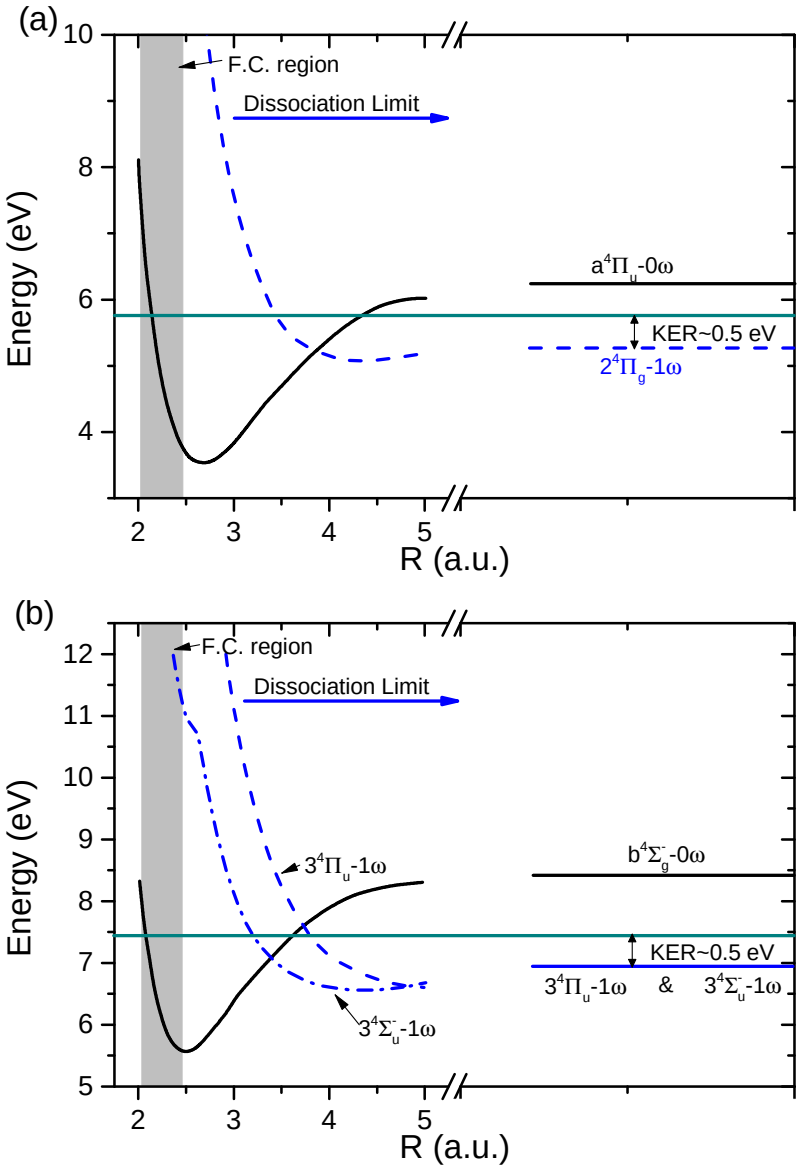

Fig. 4.5: Same as Figure-4.6 for 400nm laser pulse.

c.) $|b^4\Sigma_g^-\rangle \rightarrow |3^4\Sigma_u^- - 1\omega\rangle$. As the energy and angular resolution for the low energy fragments are not adequate to resolve these dissociation channels.

So, within the limitations, it is clear that an interpretation of the observations can be attempted unambiguously, for the high energy ions $\simeq$1.1-1.2 eV for 800 nm and 400 nm laser data.

4.4 Effect of Peak Intensity Variation of The Laser Pulse

4.4.1 For 800 nm

The left panel of Figure-4.6 shows the velocity maps of the O^+ ion at three different values of laser intensities $2I_0$, $3I_0$, and $4I_0$. The right panel shows the kinetic energy release obtained from the corresponding time-sliced velocity map images. In all the time-sliced velocity maps two distributions corresponding to O^+ ions of different energies peaking at 0.25 eV and 1.2 eV respectively are easily identifiable. A weak peak around 0.5 eV is also seen, however, it decreases in strength with increasing laser intensity. Here, at the lowest intensity the angular distribution of the energetic ions peaks at an angle of 30°, shifting towards 20° at the highest intensity (see left panel of Figure-4.8 a, b, and c). Concomitantly the mean of the distribution shifts from 38° to 28° and the standard deviation shows nearly no change. The detector angular resolution is $\simeq \pm 1.5^\circ$ for the high energy ions not taking into account thermal and laser focal volume effects.

On the other hand, the low energy $\sim$ 0.25 eV ion distribution is also not strongly peaked along the laser polarization axis at low intensities. But with increasing intensity, these ions also tend to appear predominantly along the laser polarization axis. Quantitatively, however, the mean of the distribution is within $30^\circ \pm 1^\circ$ and a prominent alignment as observed for the energetic ions is not seen. The low resolution of the detector for the low energy ions ($\simeq \pm 3^\circ$) precludes a finer distinction of the angular distribution behavior with intensity.

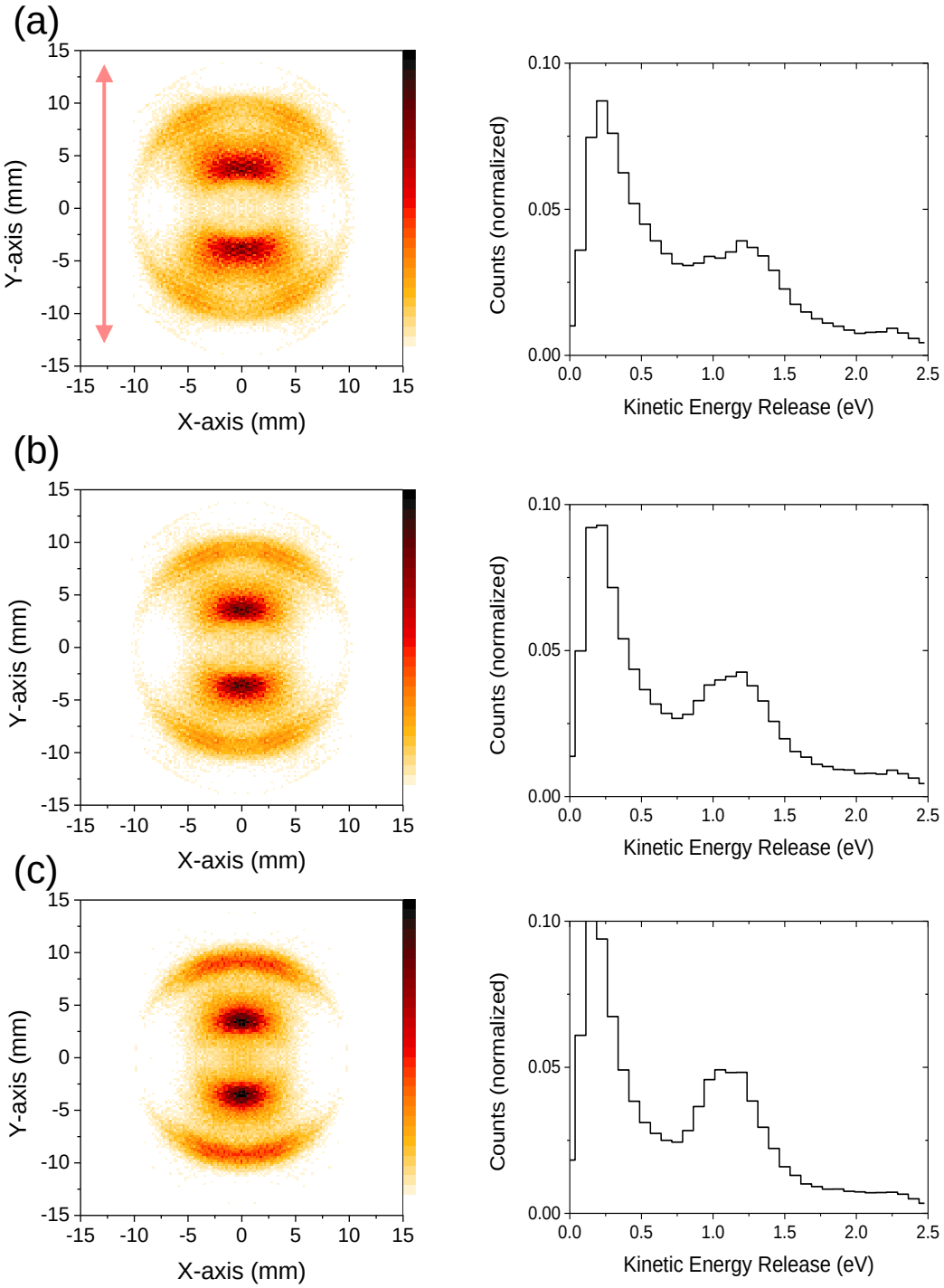

Fig. 4.6: Time sliced velocity map images of O^+ ions in the plane of the laser polarization for 800 nm, 25 fs pulses at (a)$2I_0$, (b) $3I_0$, and (c) $4I_0$. The corresponding KER distribution, obtained by azimuthal integration over these images is plotted in the right panel.

4.4.2 For 400 nm

The left panel of Figure-4.7 shows the two-dimensional velocity distribution (in a plane containing the laser polarization axis) with 400 nm, 35 fs laser pulses at the intensities I_0, $2I_0$ and $3I_0$. These velocity maps indicate two concentric distributions corresponding to O^+ ions of different energies are identifiable. The peak of the observed angular distribution for the energetic ions is at $\simeq 25^\circ$ for all intensities and is in disagreement with the prediction ($\sim 40^\circ$) of the molecular tunneling theory (see Figure-4.8d, e, and f). The mean of the distribution stays at 34° and likewise, the standard deviation shows no change with increasing laser intensity. On the other hand, the low-energy ions do not have a prominent dip along the laser polarization axis compared to the high-energy ions. The mean angle of ejection at low intensities is 28° which increases to 33° at $2I_0$ and falls to 31° for $3I_0$ with no significant change in the standard deviation.

4.5 Post Ionization Alignment

As seen in the previous section the degree of alignment of the O_2^+ molecular ion due to the interaction of 800 nm and 400 nm laser pulses shows a striking contrast with increasing intensity. For the interaction with 800 nm pulses, the observed alignment in the higher energy fragments could be associated with the involvement of the inner orbitals with σ-symmetry, which could lead to enhancement in the ion density in the velocity maps along the polarization axis of the laser pulse. X.M. Tong *et al* (59) included the HOMO-1 orbitals in the tunneling ionization from O_2 and estimated the angle-dependent ionization rate. The angle-dependent ionization rate has been compared experimentally by obtaining angular distribution following the Coulomb explosion in laser-induced double ionization of these molecules(72; 74). Previous studies indicate, that the intensities in the range of 10^{14} W/cm^2, the main contribution to the angular distribution is from HOMO orbital for O_2 molecules. The peak for angular distributions for O_2 for example is $\geq 35^\circ$, when it is compared to the angle-dependent ionization rate obtained by MO-ADK theory, which is maximum at 40°. Using the Time-Dependent Schrödinger Equation (TDSE) calculations, the ionization yields from

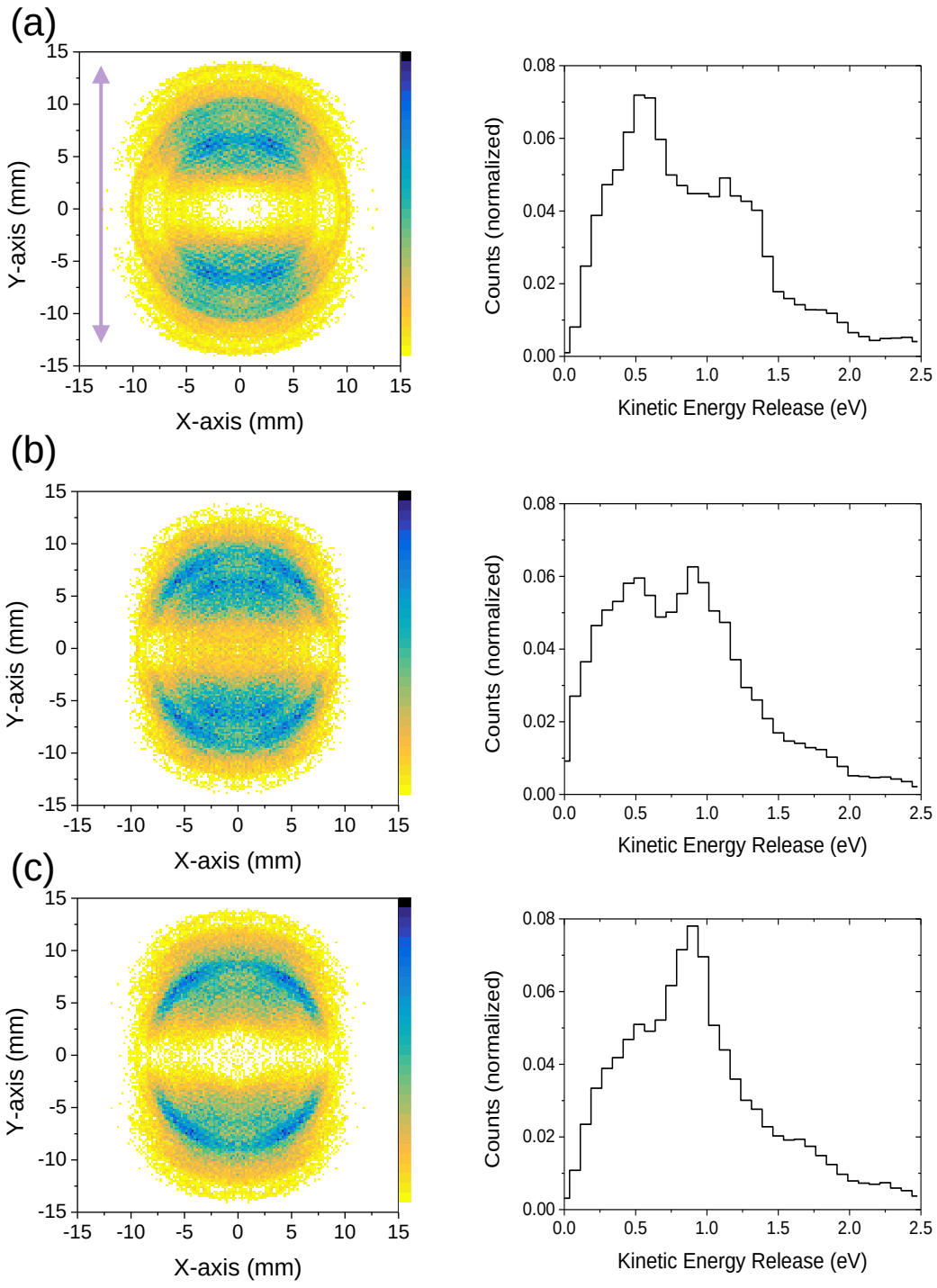

Fig. 4.7: Same as Figure-4.6, but for 400 nm, 35 fs pulses at (a) I_0, (b) $2I_0$, and (c) $3I_0$.

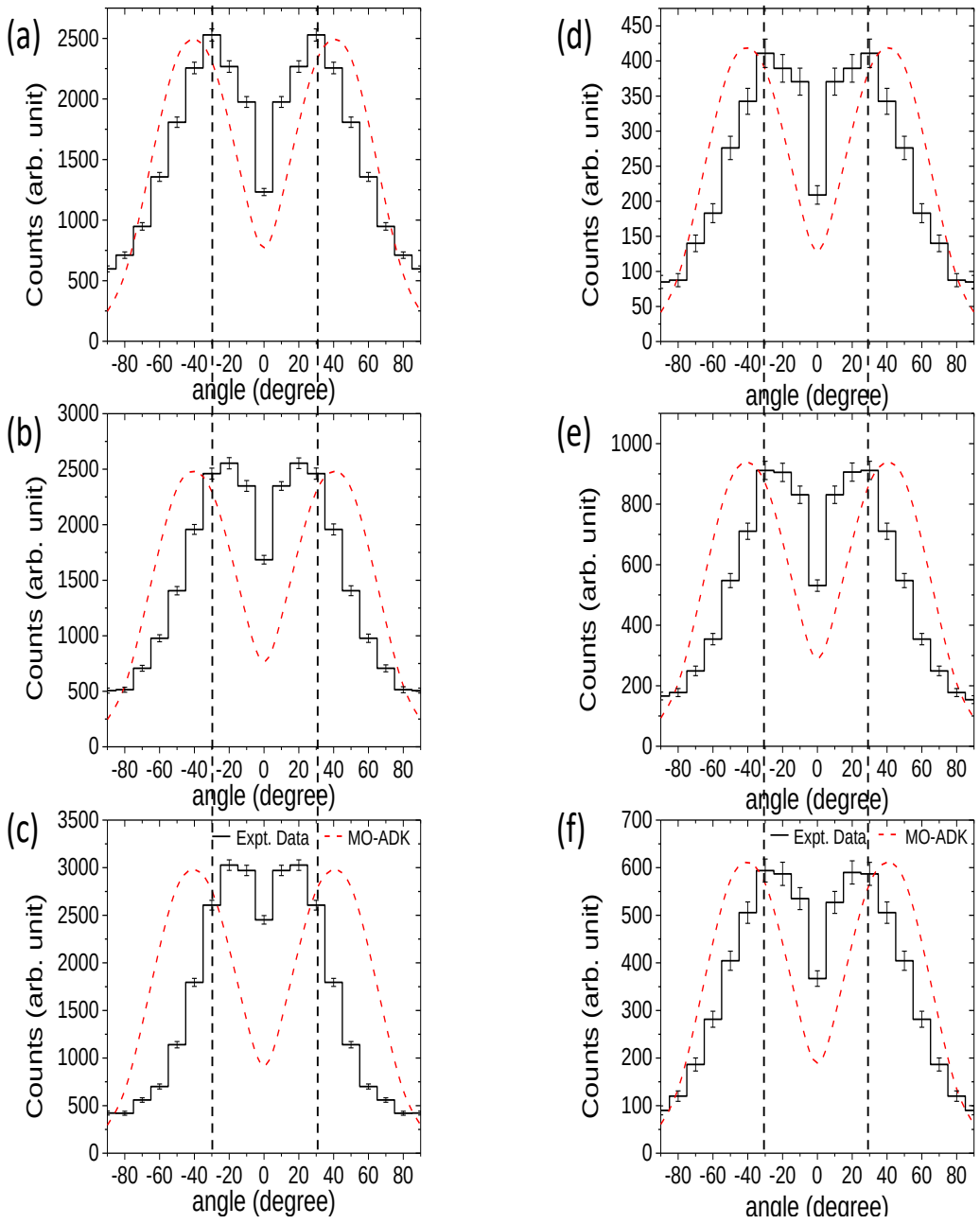

Fig. 4.8: The angular distribution (w.r.t. the laser polarization axis) of the high energy ions 25 fs, 800 nm pulses of intensities at (a) $2I_0$, (b) $3I_0$, and (c) $4I_0$. The Black histograms are experimental data. The red dashed curve indicates the expected angular distributions based on MO-ADK theory. The vertical dashed line placed at the peak position of the angular distribution obtatined at $2I_0$ to highlight the shift in angular distribution with increasing peak intensity of the laser pulse. Same for 400 nm, 35 fs pulses at intensities (d) I_0, (e) $2I_0$, and (f) $3I_0$.

the HOMO orbital for O_2 ($1\pi_g$) are seen to be greater than that from the HOMO-1 ($1\pi_u$) orbital by more than four orders of magnitude, for molecules aligned at 45° to the laser polarization. Along the laser polarization axis, ionization from the HOMO-2 ($3\sigma_g$) becomes comparable to, or even greater than that from HOMO-1. This would yield an ion signal component along the laser polarization axis and could become relevant for the interpretation of the 800 nm data. Also, the involvement of the inner orbital is to compare the ionization potentials of the HOMO (12.5 eV),HOMO-1 (19.2 eV), and HOMO-2 (19.5 eV) orbitals. Ionization of HOMO will require 10 photons, while ionization of HOMO-1 and HOMO-2 will require 15 photons. In the intensity regime between 10^{12}–10^{14} W/cm^2, the involvement of inner orbitals is highly unlikely. Even at higher intensities 10^{15} W/cm^2, at which double ionization is also seen, experimentally for O_2, there is very weak evidence of multi-orbital contribution. So, the involvements of the inner orbitals can be ruled out to support the observed alignment due to the interaction 800 nm laser pulse.

The other possibility could be the alignment of the molecule due to the rotational kick experienced by the molecule due to the induced dipole moment in the presence of the laser field. However, as we know the ionization probability of the O_2 molecule is maximum when it has a specific alignment with respect to the laser polarization axis so the rotation of the molecule prior to the ionization can not explain the alignment. However, such rotational kick after the ionization might explain the observed alignment if the dipole moment of the molecular ion and the remnant laser intensity are favorable. This is known as post-ionization alignment.

In this model, we may consider the O_2^+ molecular ion subjected to a (cycle-averaged) laser field $E(t)$. The rotational response of the molecular ion to the field, treating it to be a non-rigid rotor, is given by the equations:

$$\mu\ddot{R} = -\frac{\partial V(R)}{\partial R} \tag{4.2}$$

$$\ddot{\theta} = -\Delta\alpha\frac{E^2(t)}{2I}\sin(2\theta) - 2\frac{\dot{R}}{R}\dot{\theta} \tag{4.3}$$

where R is the internuclear separation, θ is the angle made by the internuclear axis with respect to the laser polarization, μ is the reduced mass of the molecule with a moment of inertia I and $V(R)$ is the potential energy of the molecular ion as a function of the internuclear separation. $\Delta\alpha$ is the difference between $\alpha_{||}$ and $\alpha_{\perp}$ and known as polarizability anisotropy of the molecule, where $\alpha_{||}$ and $\alpha_{\perp}$ are the molecular polarizabilities along the internuclear axis and perpendicular to it. These equations predict impulsive angular acceleration (i.e. a 'rotational kick') towards the laser polarization axis.

To make a quantitative correspondence with the post-ionization alignment model requires us to dynamically account for a number of parameters. These include the polarizability of the involved states in the dissociation, the laser pulse duration, and its intensity, and the initial orientation of the molecular ion with respect to the polarization axis. The pulse durations and intensities can be obtained from the experimental estimations. Additionally, we postulate that the molecular ion is formed at the peak of the laser pulse envelope and that the initial orientation of the molecular ion is fixed by molecular tunneling theory. What remains to be determined is the polarizability of the molecular ion as the molecule dissociates. The possible dissociation pathways assigned for the energetic fragments arising due to interaction with the laser pulse have been thoroughly discussed in the previous section (see Section-4.3). The polarizability of these participating electronic states can be extracted through quantum chemistry calculations. It is to be noted that the effect of molecular alignment prior to ionization may be happening; however, we have no way of concluding anything about it. This is justified for ultrashort laser pulses and particularly in the case of O_2 which has negligible polarizability anisotropy in the neutral ground state as known from previous works and confirmed by our calculations.

However, for the 400 nm case, in complete contrast to the 800 nm case, the angular distribution is unaffected by the increasing laser intensity. At first glance, the latter observations seem to be in complete disagreement with the post-ionization alignment model, at least qualitatively. A more careful analysis is required to understand this anomalous trend for these energetic ions arising from the interaction of 800 nm and 400 nm pulses.

4.6 Polarizability Calculation

The polarizability calculation is essential to quantify the degree of alignment of the molecular ion interacting with the laser pulse. The polarizability of the participating electronic states involved in the dissociation can be extracted by quantum chemistry calculations. The details of the calculation process are discussed in the following section.

Theory

External electric field polarizes the molecules and the polarization P depends upon the strength of the applied field. The polarization of the molecule is described by this following power series relation.

$$P(t) = \chi^{(1)}F(t) + \chi^{(2)}F^2(t) + \chi^{(3)}F^3(t) + ... \tag{4.4}$$

where $\chi^{(1)}$ is the linear susceptibility and $\chi^{(2)}$ and $\chi^{(3)}$ are the second- and third-order susceptibilities, respectively. The nonlinear terms come into play when the applied field is sufficiently large. As a consequence of this induced polarization the potential energy of the molecule also changes. The dependence of the potential energy of the molecule on an external static electric field F can be written in a Taylor series expansion of the form

$$E(F) = E(0) + \left.\frac{\partial E}{\partial F}\right|_0 F + \frac{1}{2!}\left.\frac{\partial^2 E}{\partial F^2}\right|_0 F^2 + \frac{1}{3!}\left.\frac{\partial^3 E}{\partial F^3}\right|_0 F^3 + .. \tag{4.5}$$

$$E(F) = E(0) - \mu F - \frac{1}{2}\alpha F^2 - \frac{1}{6}\beta F^3 - \frac{1}{24}\gamma F^4 + .. \tag{4.6}$$

Here μ is the permanent dipole moment and α is the dipole polarizability of the molecule. The dipole polarizability is responsible for the induced dipole moment of the molecule in the presence of the external electric field. The dipole polarizability is the second-order derivative of the electronic energy of the molecule with respect to the external electric field. The third derivative of the energy is called the first hyperpolarizability β,

and the fourth-order derivative is called the second hyperpolarizability γ. Dipole polarizability and the first and second hyperpolarizability of the molecule can be calculated using different methods such as response theory, coupled-perturbed schemes, sum-over-states method, and finite field method. The finite field method is straightforward and can be implemented easily for any quantum chemistry calculation. In this method, polarizability and hyperpolarizability can be determined directly from the potential energy of the molecule at different external electric field values. To do so we have used a quantum chemistry package GAMESS(97). Polarizabilities are readily obtained via the central difference expressions.

$$\mu = -\frac{E(F)-E(-F)}{2F} \tag{4.7}$$

$$\alpha = -\frac{E(F)+E(-F)-2E(0)}{F^2} \tag{4.8}$$

$$\beta = -\frac{E(2F)-E(-2F)-2(E(F)-E(-F))}{F^3} \tag{4.9}$$

$$\gamma = -\frac{E(2F)+E(-2F)-4(E(F)+E(-F))-6E(0)}{F^4} \tag{4.10}$$

$$\tag{4.11}$$

For homonuclear molecules like O_2, the asymmetric terms become zero. Changes in the polarity of the external static electric field do not change the energy of the homonuclear molecule $E(F) = E(-F)$.

This method is very easy to implement at a very low computational cost but it has some limits and drawbacks. This calculation is strictly valid for static response properties but the most crucial downside of this calculation is the dependence of the polarizability and hyperpolarizability on the choice of the initial field strength. Evaluation of these factors at very small values of the field leads to noise due to the finite convergence thresholds for energy and wave function optimization. On the other hand, choosing a too strong field strength will bring higher-order terms in the Taylor series and they will contribute to the potential energy of the molecule and polarizability calculation using the central difference method will become inaccurate. We have used a moderate static

field ranging from $F = 0.001$–0.01 a.u., which is equivalent to the electric field of the laser peak intensity of $\sim 10^{12}$–10^{13} W/cm^2. In the following section, the computational details of the quantum chemistry calculation are mentioned in detail.

Computational Details

All the potential energy calculations of the molecule in the presence of static electric field presented below have been performed using General Atomic and Molecular Electronic Structure System (GAMESS) quantum chemistry package(97). We have used the multiconfiguration (MC) self-consistent (SCF) method along with configuration interaction (CI)(98) to get the excited states with four different basis sets to calculate the potential energy curve.

- Dunning and Hay type 'double' zeta basis set with d- and p-type polarization functions. (DH)
- Dunning type correlation consistent triple zeta valance basis, but augmented with a set of diffuse functions.(aug-cc-pVTZ)

The change in the potential energy of the molecule in the presence of the external field is very small. For the maximal precision of these numerical differences, care was taken that all the wave-function, molecular energies were tightly converged. We have put the threshold value for convergence of the energy to 10^{-10} for our SCF calculation and 10^{-8} for our CI calculation. All the calculations are carried out in point group symmetry C1 and because of that π_x and π_y are no more degenerate. For this reason quartet ground state of O_2^+ ended up with two different states, which were averaged over these two states to avoid the degeneracy artifact.

Results

We have performed polarizability calculation of the ground state of the neutral O_2 to optimize all the parameters used in quantum chemistry calculation. Figure-4.9a shows the calculated field-free potential energy curve of the ground electronic state $X^3\,\Sigma_g^-$ of

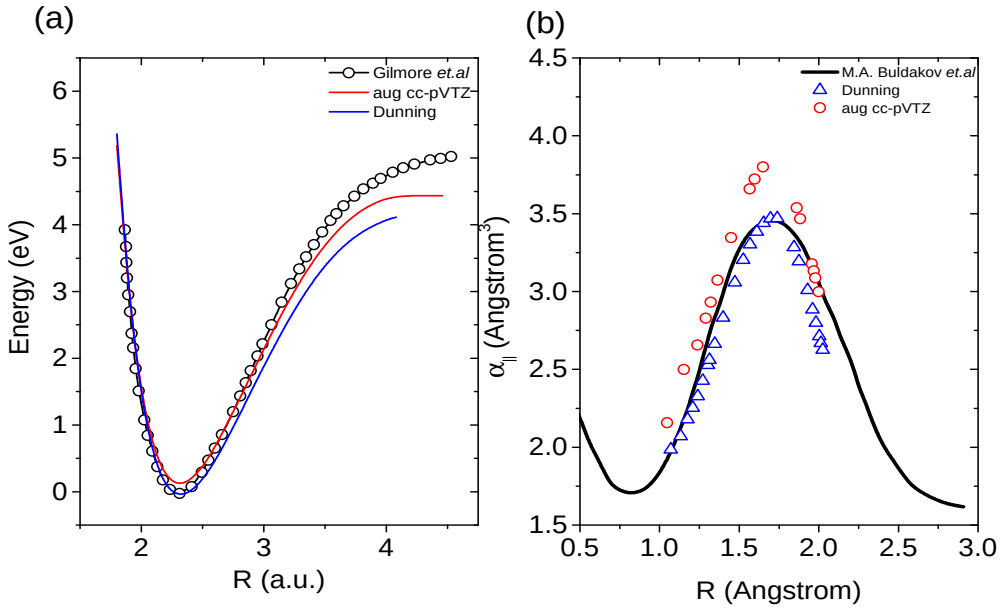

Fig. 4.9: (a) Potential energy curves calculated using two different basis sets. Blue curves: Dunning and Hay type basis set. Red curves: correlation consistent triple valance zeta basis set. Black circles: obtained from work of Gilmore*et.al*(99). (b) Calculated dipole polarizability ($\alpha_{||}$) along the molecular axis using finite difference method with external field value $\pm$0.002a.u. using two different basis sets. Black dashed line: dipole polarizability ($\alpha_{||}$) calculated by M.A.Buldakov*et.al*(100).

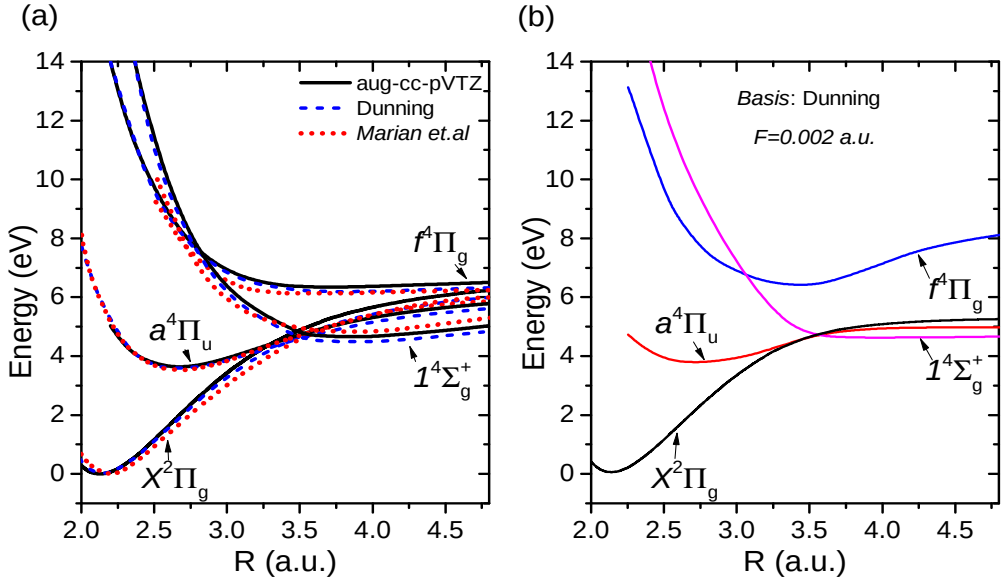

Fig. 4.10: (a) Potential energies for the O_2^+ molecular ion for doublet and quartet states using Dunning type and correlation consistent augmented triple zeta valance type basis set. The zero of the energy axis is taken as the $v = 0$ level of the $X^2\Pi_g$ ground state of O_2^+ ion. (b) Same potential energy curves in the presence of electric field $F = 0.002$ a.u. along the molecular axis.

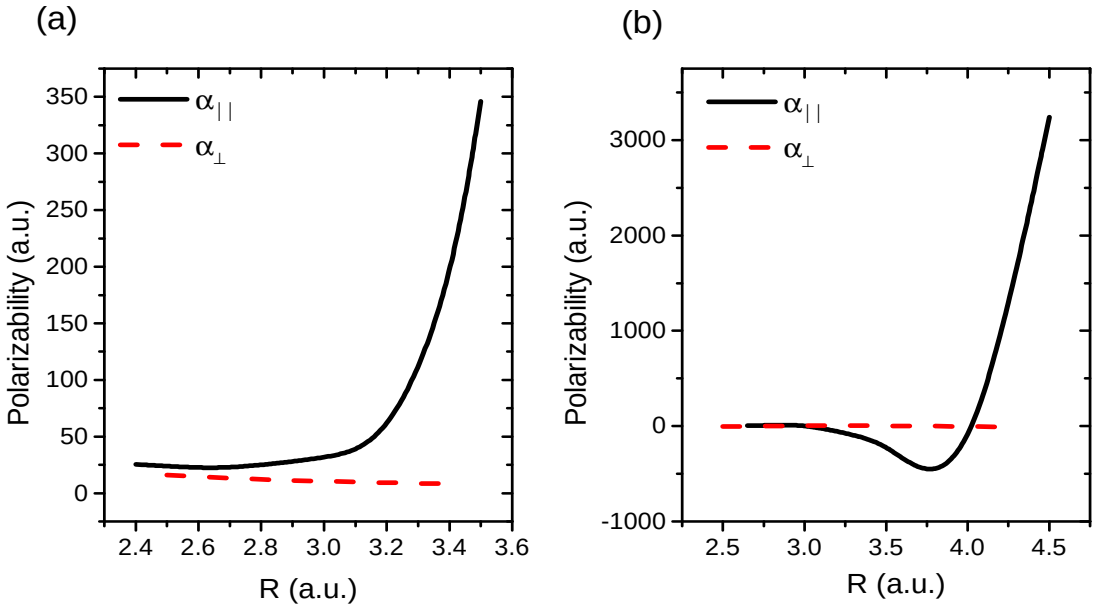

Fig. 4.11: Calculated polarizabilities ($\alpha_{\perp}$ and $\alpha_{||}$) of the (a) $a^4\Pi_u$ and (b) $1^4\Sigma_g{}^+$ states which participate in the proposed dissociative ionization pathway.

neutral O_2 with two different basis sets(99). We have compared our result from the experimental observation and found the error in calculating dissociation energy by using Dunning type basis set and correlation consistent augmented triple zeta valance type basis set to be 1.3% and 2.5% respectively. Using the finite field method the polarizability of the ground electronic state of O_2 has been estimated and it shows a good agreement with the analytically estimated polarizability value provided by Buldakov *et. al*(100) for the field value $F = 0.002$ a.u. (see Figure-4.9b).The estimated polarizability values for the applied field range from $F = 0.001$–0.01 a.u. shows a variation of roughly $\sim$10% from the analytically estimated values.

Similarly, the potential energy curves and the polarizability of the excited electronic states of O_2^+ ion are calculated. Figure-4.10a shows some of the calculated electronic states using two different basis sets and it shows a reasonable agreement with the data from Marian *et.al*(101). Having a good agreement with previous calculations for different states, we proceed with the dipole polarizability calculation of these electronic states. The response of these electronic states in the presence of the external field of field

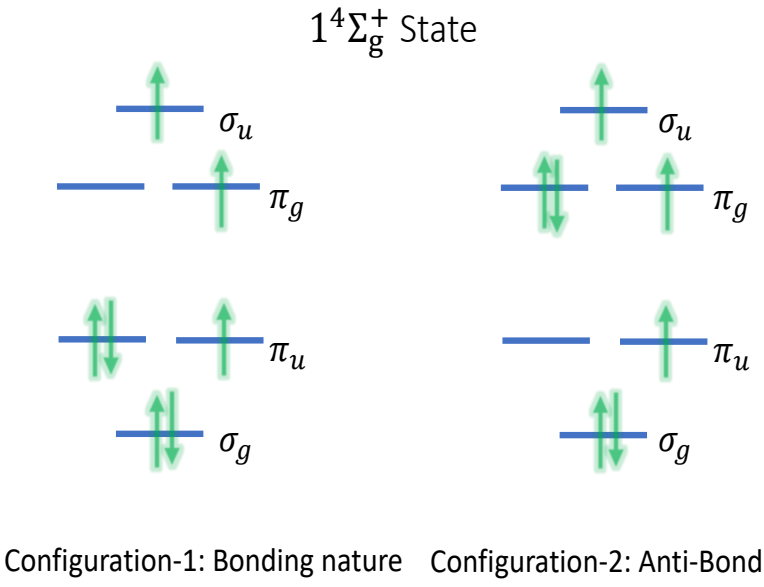

Fig. 4.12: Dominant electronic configuration diagram of $1^4\Sigma_g$ state.

value $F = 0.002$ a.u. has been shown in Figure-4.10b. The calculated polarizabilities for the states $a^4\Pi_u$ and $1^4\Sigma_g{}^+$ from the finite field method are plotted in Figure-4.11 as a function of R. For small internuclear distances, the values for both states are small and positive. Beyond R of 3.0 a.u, the polarizability of $1^4\Sigma_g{}^+$ goes negative. Conversely, the polarizability of the $a^4\Pi_u$ state rapidly rises to large positive values with increasing R.

Origin of negative polarizability

Examples of negative polarizability are sparse, as such phenomena can only be observed in the excited states of the molecule. Some reports in this context are on near-threshold photodetachment of alkali ions, in which large negative polarizability of the excited state inhibits the detachment process. This is a consequence of electronic repulsion arising from neighboring low-lying electronic states. In the case with O_2^+ ions, the complex multi-correlation effect in the presence of an external electric field plays an important role behind the negative polarizability in one of the excited electronic states.

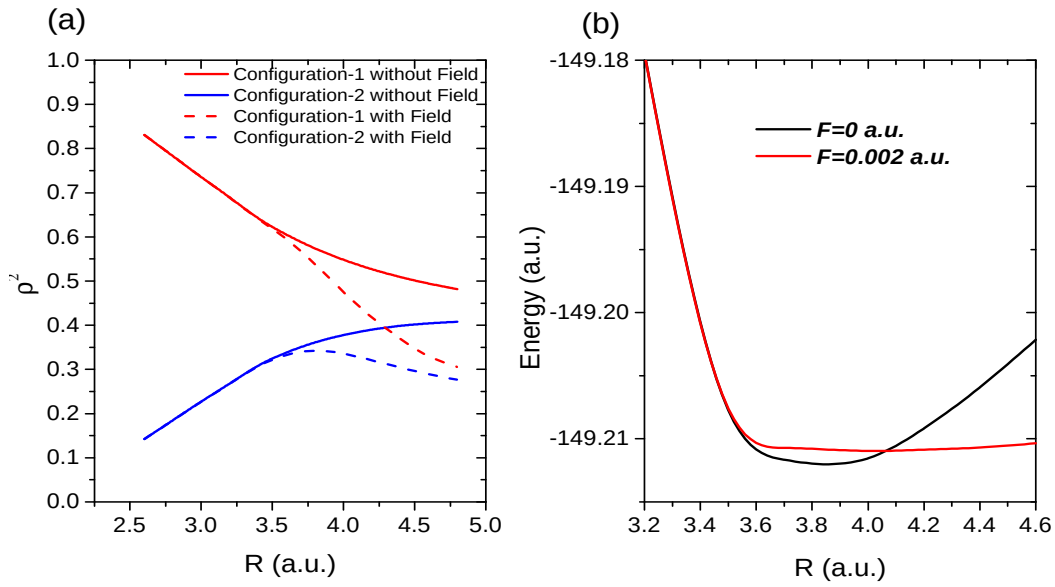

Fig. 4.13: (a) The change in squared configuration interaction coefficient for the bonding and anti-bonding configuration at external electric field $F = 0.002$ a.u. (b) Potential energy curve of $1^4\Sigma_g$ state in the presence and absence of the electric field applied parallel to the molecular axis.

The electronic states are represented by a linear combination of configuration state functions(CSFs). Each CSF corresponds to a configuration diagram(see Figure-4.12). In our calculation, we have found two dominant electronic configurations giving rise to the $1^4\Sigma_g$ state. One of the configurations shows the electron population in bonding orbital to be greater than in anti-bonding orbitals(see Figure-4.13a). The other configuration shows the anti-bonding nature. In the field, free condition CI level calculation shows, that the contribution from these two (bonding and anti-bonding configurations) varies with the internuclear separation, as the internuclear separation increases the anti-bonding nature of the electronic state increases(see Figure-4.13b). However, the presence of the external field applied along the molecular axis changes the behavior of the electronic state. Figure-4.13a shows that the bonding nature of the electronic state, $1^4\Sigma_g$, diminishes rapidly in the presence of the field beyond $R \sim 3$ Å and it destabilizes the state. The external field distorts the molecular orbitals, leading to a change in the energy of the electronic state. The distortion of the orbitals will also depend upon the applied field values and internuclear separation. It is plausible that the destabilization

and distortion in the presence of electrostatic field is a multi-electron correlation effect, which gives rise to 'negative polarizability'

4.7 Rotation and alignment of the transient molecular ion

The coupling of the polarizability to the 'averaged' electric field of the laser pulse, accounts for the rotational impulse, causing the molecule to change its orientation. Since the rotor is non-rigid, the rotational acceleration also leads to an increase in the internuclear separation. This, in turn, increases the moment of inertia thereby damping the rotational motion. This evolution of the system is followed in time until the internuclear separation increases to ten times the ground state bond length, giving us the asymptotic value of the molecular orientation. This calculation is done for different initial molecular orientations between $\theta = 0^\circ$ and 90° and weighted by angle-dependent ionization probability from molecular tunneling theory, as the shape of the HOMO of O_2 determines the preferred orientation of O_2 for ionization. The molecular ion is assumed to be created at the temporal peak of the laser pulse at an internuclear separation of $R_0 = 2.3$ a.u via a Frank-Condon transition. At the peak of the laser pulse, $t = 0$, the molecular ion is created in $a^4\Pi_u$ state with $R = 2.3$ a.u. In this state the molecule is 'kicked' in the direction of the laser polarization axis by the induced dipole, resulting in alignment. In a quantum mechanical picture, the above process can be modeled as the evolution of a ro-vibrational wavepacket created in the $a^4\Pi_u$ state. The wavepacket evolves leading to increasing mean internuclear distance with time corresponding to a classical traversal of the molecule along the potential energy curves.

The differentiation between the response to 800 nm and 400 nm irradiation hinges on the difference in the point of crossover from one state to another. The transition in the 800 nm case happens at $R \sim 3.2$ a.u and $R \sim 2.8$ a.u in the 400 nm case (see Figure 4.14 and 4.15). Thus, in the 400 nm case, the molecular ion crosses over to the $1^4\Sigma_g{}^+$ state at an earlier instant of time as compared to the 800 nm case. The longer

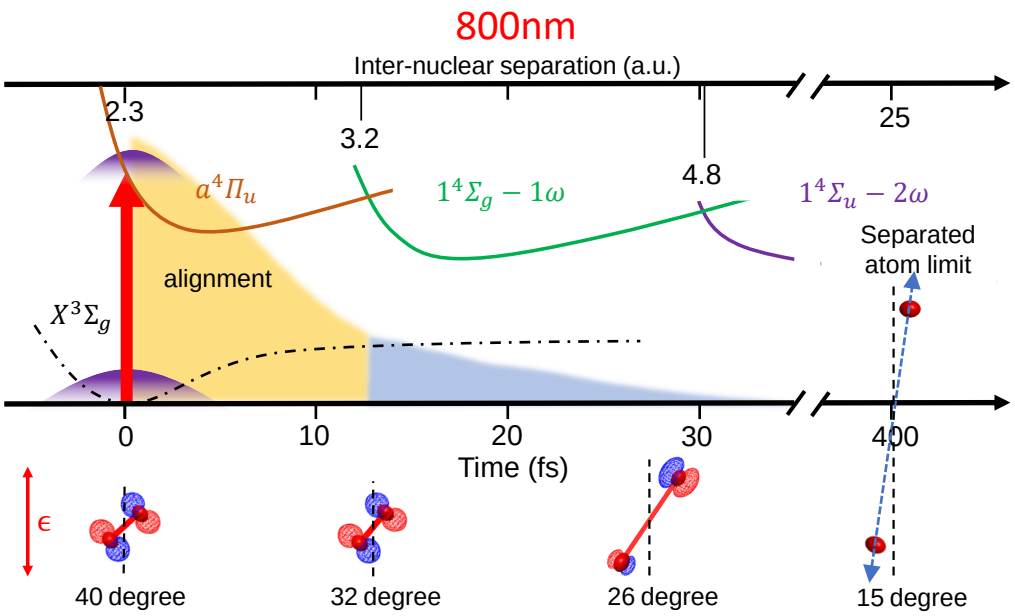

Fig. 4.14: Schematic of the dissociation of O_2^+. In the presence of 25 fs 800 nm pulses, the value of $\alpha_{||}$ for the $a^4\pi_u$ state (brown curve) is positive, resulting in a strong aligning torque. The shaded areas denote the cycle-averaged, quasi-static field of the laser pulse. When the ion makes a transition to the negative polarizability state (green curve) at $R \sim 3.2$ a.u. ($t \sim 13$ fs), the torque due to the weak trailing pulse (blue shaded) is insufficient to counter the alignment.

400 nm pulse means that after the molecular ion makes a transition to the $1^4\Sigma_g{}^+$ state, the negative polarizability produces a decelerating torque, hindering the alignment. In the 800 nm case, by the time the transition to $1^4\Sigma_g{}^+$ state occurs, the laser intensity falls drastically, and as a result, the rotation under the influence of the positive value $\alpha_{||}$ of the $a^4\Pi_u$ state causes the molecular ion to evolve essentially unhindered.

The blue curves in the angular distributions shown in Figure-4.16 are from calculations based on the evolution along the pathways explained above and the calculated polarizabilities of the participating states. The only free parameter used in the model is the laser intensity and the calculated angular distributions are normalized to the experimental distributions on the total counts. The intensities used for the calculation are systematically higher than the experimental intensities by a nearly constant factor of around $\sim$1.5. A 20–25% uncertainty in estimating experimental laser intensities is a common issue in strong-field laser-matter interaction studies, so, the broad agreement between model and experiment is noteworthy.

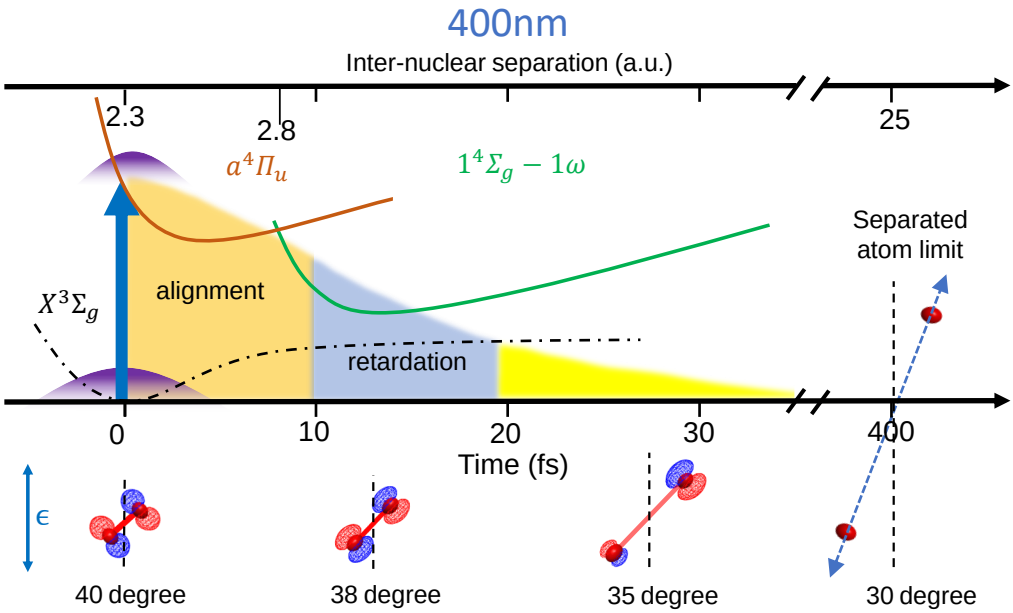

Fig. 4.15: For 35 fs 400 nm laser pulses, the molecular ion created in the $a^4\Pi_u$ state crosses over to the $1^4\Sigma_g$ dressed state, which has a negative value of $\alpha_{||}$. The ion crosses over to the state with $\alpha_{||} < 0$ earlier in time ($t \sim 7$ fs or at $R = 2.8$ a.u.). There is sufficient remnant laser intensity (blue shaded region) at this time, which coupled with the negative polarisability, will hinder the alignment.

4.8 Discussion

In essence, we have inquired why fragment angular distributions and their dependence with laser intensity are different for 800 nm and 400 nm laser pulses. In the two-step model for the dissociation, we have assumed, the ionization of the molecule is through a tunneling process and yields a preferred alignment for the molecule. In the second step, the dissociation of the molecular ion proceeds through dressed states whose polarizabilities account for further rotation of the molecular ion during dissociation. The tunnel ionization has been modeled through MO-ADK here, but it is pertinent to have a look at other approaches used to explain the angular distribution from fragmentation. For example, including multiorbital tunneling(102) in the ionization from N_2, O_2, and CO in the calculations, angular dependent ionization rates can also be obtained. These compare better with experimentally obtained angular distributions following the Coulomb explosion in laser-induced double ionization of these molecules. However, it is clear that for the intensities in the range of 10^{14} W/cm^2 , the main contribution to the angular

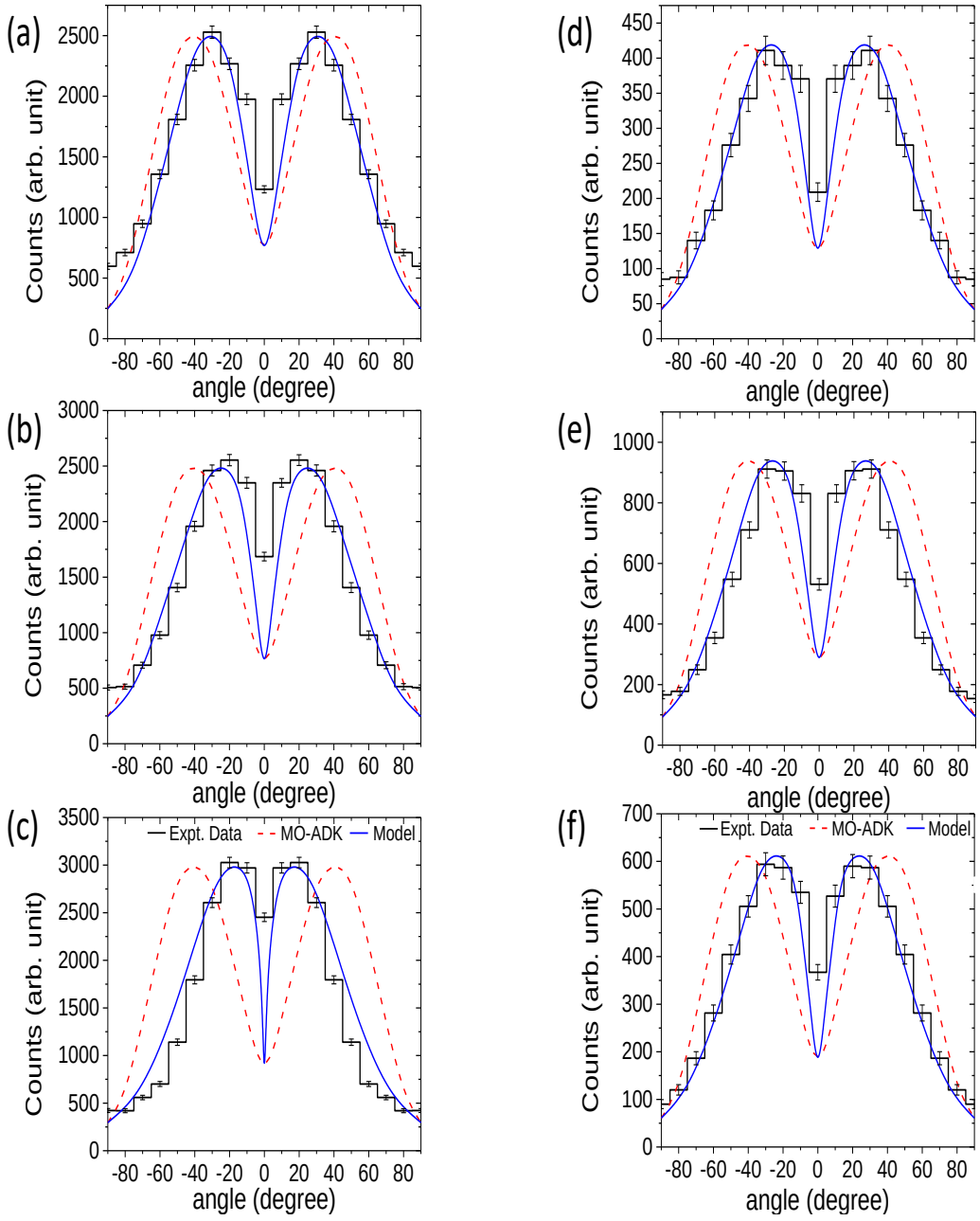

Fig. 4.16: The angular distribution (w.r.t. the laser polarization axis) of the high energy ions is shown for (a) $2I_0$, (b) $3I_0$ and (c) $4I_0$. Black histograms are experimental data. The blue solid curve is from our model that includes molecular tunneling and torque due to the laser. The same for 35 fs, 400 nm pulses of intensities (d) I_0 (e) $2I_0$ and (f)$3I_0$.

distribution is from the HOMO for molecules such as D_2, N_2, and O_2, while for CO, there is significant ionization from the HOMO-1 orbital. The peak for angular distributions for O_2, for example, is $\geq 35^\circ$, as compared to 40° using MO-ADK theory. Using Time-Dependent Schrödinger Equation (TDSE) calculations(103; 104) the ionization yields from the HOMO orbital for O_2 ($1\pi_g$) are seen to be greater than those from the HOMO-1 ($1\pi_u$) orbital by more than four orders of magnitude for molecules aligned at 45° to the laser polarization (800 nm). Along the laser polarization axis, ionization from the HOMO-2 ($3\sigma_g$) becomes comparable to, or even greater than that from the HOMO-1. This would yield an ion signal component along the laser polarization axis and could become relevant for the interpretation of the 800 nm data. However, the ionization rates for the HOMO-2, along the laser polarization axis, are still two orders of magnitude lower than those of the HOMO for 400 nm and four orders of magnitude lower for 800 nm. Furthermore, including other effects such as exchange interactions(105) would lead to small corrections to the absolute value of the peak of the angular distribution of O_2^+ and to corrections in the yield parallel and perpendicular to the laser polarization axis.

In the dissociation step, laser field-induced deformation of the PEC manifests as bond-softening and bond-hardening, modifying the preferred directions of ejection of the fragments(106). Specifically, in bond softening, the bond is weakened and dissociation through this channel is enhanced for transition dipole moments aligned parallel to the laser polarization axis. This could be a possible explanation for the alignment trend observed for the 800 nm data. However, to explain the 400 nm results, we would have to invoke the opposite effect of bond-hardening, where the molecular ion seeks antialignment to dissociate, with the additional complication of having to account for the absence of the bond-softening channel in the experimental data. We have considered these possibilities with the molecular ion states available and have not been able to come to consistent and physically feasible explanations.

The observation of alignment effects in laser-induced fragmentation of molecules is fairly ubiquitous over a large range of laser intensities and pulse lengths. Only with intense ultrashort ($<$8 fs) laser pulses where Coulomb explosion of the doubly charged

species is initiated before the molecule can rotate is the alignment arrested. The experimental angular distribution of O^+ in these experimental conditions matches with MO-ADK predictions. Our results of the 800 nm pulses appear to match the MO-ADK predictions in conjunction with the post-ionization alignment model. In the case of 400 nm, primarily, we notice a discrepancy with respect to the expected angular distribution from MO-ADK alone and also an apparent discrepancy from the post-ionization alignment model. Through our semiclassical model, we can account for both the alignment and the hindering of alignment in the dissociation step.

A criticism of the model could be the use of static polarizabilities close to the transition. In the region of the resonance, the polarizability associated with the oscillating laser field, i.e., the dynamic polarizability should be considered. However, the dynamic polarizability rapidly diverges and flips its sign as it passes the resonance. Therefore, for the dissociating molecule, the integral contribution to the aligning torque from the dynamic polarizability is insignificant compared to that due to a quasistatic (averaged) field. An ambiguity in interpretation may stem from the assignment of the dissociation pathway, for which we have assumed that only single-photon transitions couple O_2^+ to a dissociating state (subsequent to multiphoton ionization of O_2 in the ground state). These assignments need to be validated with TDSE calculations. In spite of these limitations of our model, we posit that our results suggest that the negative polarizability of an excited state leads to the hindering of the molecular ion alignment in the laser field. Nevertheless, detailed experiments over varied intensities and pulse lengths are warranted to clarify this interpretation.

4.9 Summary

Dissociative ionization of a molecule via laser pulses is inherently complex, involving the coupled dynamics of a multi-body system. Here, through fragment ion imaging and a simple model, we have explored molecular alignment and we have extracted an important molecular property, viz polarizability, which governs the alignment(107). The evidence of negative polarizability in excited states of a simple molecular system(108),

which is observed in a certain state and is found to be closely connected with the unexpected alignment behaviour. Of particular interest would be to investigate the origin of this singular behaviour, possibly a result of electron correlation. In alkali atoms, we see this as a consequence of electronic repulsion of the state by neighboring low-lying electronic states through the Stark Effect. Conjugated polymers in weak electric fields exhibit correlated bi-excitonic states with negative polarization. Our calculations suggest that the state in question is composed of electronic configurations of both anti-bonding and bonding characters. A subtle change in the relative weights of the configuration under the influence of the electric field causes the state to have higher energy, and hence, the negative polarizability. If such states are easily accessible, then, in the context of recent advances in the control of molecular rotation, one could conceive of switching applications and pulse shaping in the THz frequency range and it could potentially uncover rich correlation physics.

CHAPTER 5

DISSOCIATION DYNAMICS OF CH_3I IN INTENSE ULTRASHORT LASER FIELDS

5.1 Introduction

The coupled response of the electronic motion and the nuclear motion in a molecule subjected to several phenomena such as bond softening(10), bond hardening(11), and enhanced ionization(39; 40; 41) was observed even in the simplest molecular systems H_2^+ / D_2^+. In recent times, many attempts have been made to understand intense field interaction with multi-electronic molecular systems, based on the understanding of the template molecular systems H_2^+ / D_2^+. However, multi-electronic molecular systems, such as diatomic molecules, like O_2(106), N_2, HCl, CO and small polyatomic molecules, like CO_2(82), NO_2, C_2H_2(42), CH_3I(109; 110; 111; 112; 113) present more complex effects as a consequence of the involvement of multiple electronic states and multiple orbitals, induced by nuclear dynamics. The participation of multiple orbitals even within a single electronic state and the role of the symmetries of these orbitals make for a rich and often inextricable dynamic response of the molecular system. In the previous chapter we have shown, how the electronic processes can govern the dissociation dynamics of a molecular system. For a diatomic system, like O_2, electronic processes like the transition between several photon-coupled states occur in a time scale that is less than $\sim$20 fs. Detailed time-resolved studies, like pump-probe experiments, are required to understand ultrafast dynamics for diatomic molecules in greater detail. To do such time-resolved experiments, the pulses should be much shorter than the time-scale associated with the typical vibrational time-scale ($\leq$10 fs)of a diatomic molecular system. The shortest pulse available in our lab ($\sim$25 fs) is not suitable for time-resolved experiments for most of the diatomic molecular system. However, time-resolved studies

are possible in heavier molecules even with ∼25 fs pulses, since the internal dynamics get slower due to heavier masses.

CH_3I has been a popular molecule for studying ionization, and dissociation over many years. CH_3I has a geometry with C_{3v} symmetry, which leads to various distinguishable vibrational motions, and due to the presence of a heavier atom, Iodine, the vibrational motion gets much slower than O_2. Slower vibrational motion allows time-resolved studies even with a ∼25 fs laser pulses. The presence of Iodine also adds to the complexity of the spin-orbit splitting of the electronic states. Dissociation dynamics of CH_3I in the NIR wavelength regime have only recently been investigated in a few time-resolved studies, incorporating techniques such as transient photo absorption spectroscopy(114) and Coulomb explosion imaging (CEI) of the fragment ions(115; 116). These pioneering studies along with a plethora of single-pulse experiments have helped to improve our understanding of the orbitals involved in the non-adiabatic ionization(117; 118) and the dominant pathways for dissociation and energetic fragmentation(114; 119). There remain, however, several aspects of molecular ionization and dissociation that have not been addressed yet. In particular, there has been recent interest in understanding the phenomena of enhanced ionization in multi-electron molecules. For diatomic molecules, laser-induced electron transfer creates transient ionic states, which are unstable towards ionization. The probability of formation of such ionic states reduces with increasing inter-nuclear separation, and hence the ionization rate is enhanced around a critical range of inter-nuclear distances(120). An alternative picture considers the effect of geometry-induced alterations in the energies of molecular orbitals at increased inter-nuclear separation, and effective ionization from the laser-coupled orbitals(42; 121). In experiments, the observed kinetic energies in laser-induced fragmentation of CH_3I are usually explained by invoking enhanced ionization beyond the equilibrium bond-separation, despite the lack of clarity in the underlying mechanism. At high intensities ($> 10^{14}$ W/cm^2) using ultrashort fs laser pulses, the formation of higher charge states is expected, usually triggered by efficient ionization by rescattering electrons. At low to moderate intensities, the route to the generation of higher charge states is via long pulses (0.1–10 ns) with wavelengths suitable for accessing intermediate resonances, the so-called ladder-climbing mechanism.

But with sub ps to ps pulses, the generation of high charge states at moderate laser intensities, as an explicit application of the postulated enhanced mechanisms referred to above has not been shown. However, a systematic time-resolved study can answer these questions. The most common way to do time-resolved studies is by pump-probe experiments; where a single pulse ionizes the molecule and creates vibrational wavepackets over some electronic state which we want to study and then a second pulse is applied just after the first pulse with some time delay to probe the nuclear dynamics over this specific excited state. Similar information can also be obtained by stretching a single pulse over a wide range from fs to ps regime systematically by keeping a constant peak intensity.

In this thesis work, we have studied the dynamics of molecular dissociation of multiply-charged CH_3I following its interaction with moderately intense ($\sim 10^{12}$ W/cm^2) laser fields investigated as a function of varying pulse duration from 25 fs to 1.5 ps. Using a velocity map imaging spectrometer, the kinetic energy distributions and angular distributions of the major ionic fragments are detected. With the help of detailed quantum chemistry calculation and a systematic experiment, we have tried to answer the contribution of orbital rearrangement in the dissociation dynamics of CH_3I molecule.

5.2 Experimental Details

The main requirement for this study is control over the pulse duration over a wide range and it has been achieved by compressor grating pair. The characteristics of the grating pair are discussed in the following section.

Pulse Duration Variation

The system delivering the ultrashort laser pulses for our experiment, Femtopower V (Spectra-Physics, Austria), provides few-mJ laser pulses at 1 kHz at a central wavelength of 800 nm. A fraction of this power is used for the molecular physics experiments in the ion-imaging spectrometer(87). The shortest pulse duration measured just after the

laser amplifier unit through autocorrelation, is $\sim$ 25 fs. Longer pulses can be obtained by varying the separation between the compressor grating pair. The corresponding pulse duration is estimated from the dispersion curve for the grating pair supplied by the manufacturer. However, using the autocorrelation technique the pulse duration of the laser pulses can be measured for different compressor grating pair separations. The associated residual error arising between the estimated and the measured pulse duration indicates, that for longer pulses the residual error stabilizes to nearly $\sim$10%. To characterize the compressor grating pair we have generated the second harmonics using the KDP crystal (0.5 mm, Eksma Optics, Lithuania) and measured the spectra as a function of grating separation(122). This is similar to the dispersion scan technique, where external dispersion is introduced through the grating rather than glass wedges. We have simulated this experiment numerically, using the values of the compressor as provided by the manufacturer, and compared the generated spectra with the experiment, which shows a good agreement. For pulse durations beyond 75 fs, the dispersion characteristics and hence the pulse widths are determined largely by the grating compressor with a residual error of $\sim$ 10%. The polarization of the laser beam is linear and can be set parallel and perpendicular to the ion-imaging spectrometer axis by using a $\lambda/2$ plate (B-Halle, Germany). The laser beam is focused in the spectrometer chamber by using a thin lens with a focal length of $f = 30$ cm, which focuses the beam to a measured spot size of $\sim$ 70 μm. A peak laser intensity of $I_0 = 5\times10^{12}$ W/cm^2 is thereby estimated. The intensity values are calibrated independently in a COLTRIMS set up using the same laser focusing geometry, where, features in the ion spectrum can be used to extract the intensity in the focus(123).

Spectrometer Conditions and Multi-hit Coincidence

The details of the spectrometer(87) and the extraction of three-dimensional velocity distributions of the laser-induced fragmented ions are thoroughly discussed in Chapter-3. In this specific experiment, the spectrometer is used in two different modes a) the standard imaging mode, where the laser polarization axis is kept perpendicular to the spectrometer axis to obtain the 3-D velocity distribution of the fragment ions, and in

b) the time-of-flight (ToF) mode with the polarization axis parallel to the spectrometer axis. The laser pulse energy is adjusted to maintain the same peak intensity for the different pulse durations. For each laser pulse duration setting, velocity distributions for the different ions are obtained for the same amount of time (2 hours), ensuring the same number of laser shots (within $\pm 5\%$) and constant gas pressure throughout. Since the masses of the fragments are significantly different, the spectrometer voltages have to be turned over a wide range of values to ensure full collection.

The spread in the flight times of ions in the ToF mode can be used to calculate kinetic energies and thus confirm the ion kinetic energies obtained from the velocity distribution. Furthermore, the multi-hit capability of the detector (Roentdek GmbH, up to 8 ions with a double hit dead time of <10 ns) is also exploited to check if there are any coincident ions recorded in the second hit. Through photoion-photoion coincidences, ion-pair break-ups including those with high fragment energies can be unambiguously identified, and their mean ion energies ascertained. The gas pressure is kept low enough to have an event rate of <1 per pulse to avoid false coincidences on the imaging detector and any possible space charge effects. Using the gratings to stretch the laser pulse inevitably introduces wavelength dispersion into the laser pulse. All measurements reported here are done with a positive (dominant) second-order dispersion. The effect of the sign of the dispersion is checked by obtaining spectra for a few pulse duration settings but with negative second-order dispersion and differences are found to be insignificant.

5.3 Time-of-Flight Spectrum

Figure-5.1 and Figure-5.2 show the time-of-flight spectrum of the ionic fragments arising from the interaction of methyl iodide with an 800 nm laser pulse with peak intensity I_0 for two different pulse duration $\sim$25 fs and $\sim$1500 fs, respectively. In both the cases, the dominant peaks are coming from the parent ion CH_3I^+, the singly charged methyl group CH_n^+ $(n = 0\text{–}3)$ and the iodine ions I^{q+} $(n = 0\text{–}2)$. However, the nature of the time-of-flight spectrum of these ionic fragments shows a drastic change with respect to

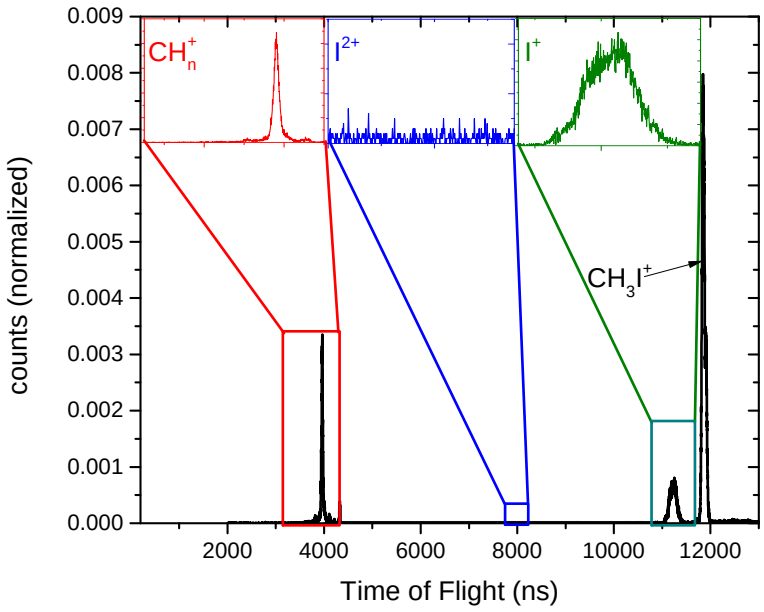

Fig. 5.1: The time of flight spectrum at a pulse duration of ∼25 fs with peak intensity 5×10^{12} W/cm^2 with the main fragments highlighted and their peaks shown in an expanded form.

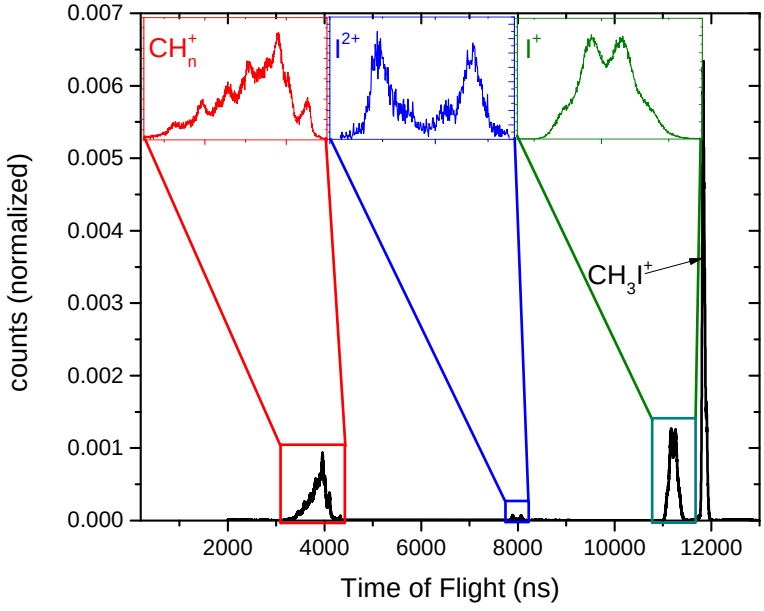

Fig. 5.2: Same as Figure-5.1 at a pulse duration of ∼1500 fs with peak intensity 5×10^{12} W/cm^2

each other. The major ionic fragments are highlighted in the inset of Figure-5.1 and Figure-5.2. It indicates for the shortest pulse duration ∼25 fs, CH_3^+ is the dominant ionic fragment, however, for the longest pulse duration, other fragments are observed in significant quantities. On the other hand, the time-of-flight spectrum of the I^+ ions also indicates a significant change as the contribution from higher energy I^+ ionic fragments increases drastically for the longest pulse duration, ∼1500 fs. Another significant change is observed in the complete time-of-flight spectrum as a new ionic species, I^{2+} is arising for the longest pulse duration,∼1500 fs. However, assigning the parent molecular ions only from the time-of-flight spectrum is impossible. One can identify these fragmentation channels depending upon the final ionic fragments by simultaneous detection of multiple ions and by plotting a 2-D histogram of the Time-of-Flight spectrum of the ion species hitting first and second on the detector, known as 'Correlation Map'. In the following section, we will try to figure out all the fragmentation channels based on the observed Correlation Map.

Multi-Hit Coincidence: The Correlation Map

The photoion-photoion coincidence map shown in Figure-5.3a and b identifies ions obtained in pairs from the fragmentation of the dication molecular ion for pulse durations of ∼25 fs and ∼1500 fs, respectively. For the shortest pulse duration, only a set of islands of ionic fragment pair $CH_n^+ + I^+$ is observed. It mainly arises from a concerted break up from CH_3I^{2+}. Two prominent sets of islands are visible for the longest pulse duration, which represents the coincident detection of the fragment pairs: *a*) $CH_n^+ + I^+$ and *b*) $CH_n^+ + I^{2+}$. Each set contains four pairs of islands associated with coincident detection of CH_3^+, CH_2^+, CH^+, and C^+ ions with I^+/I^{2+}. However, several uncorrelated events indicated as false counts are also detected on the diagonals between the island pairs. The islands are however separated and with suitable conditions imposed the coincident events can be uniquely extracted for analysis. The nature of these islands in the coincidence map indicates a concerted, energetic, back-to-back break up from the molecular ions CH_3I^{2+} and CH_3I^{3+} respectively.

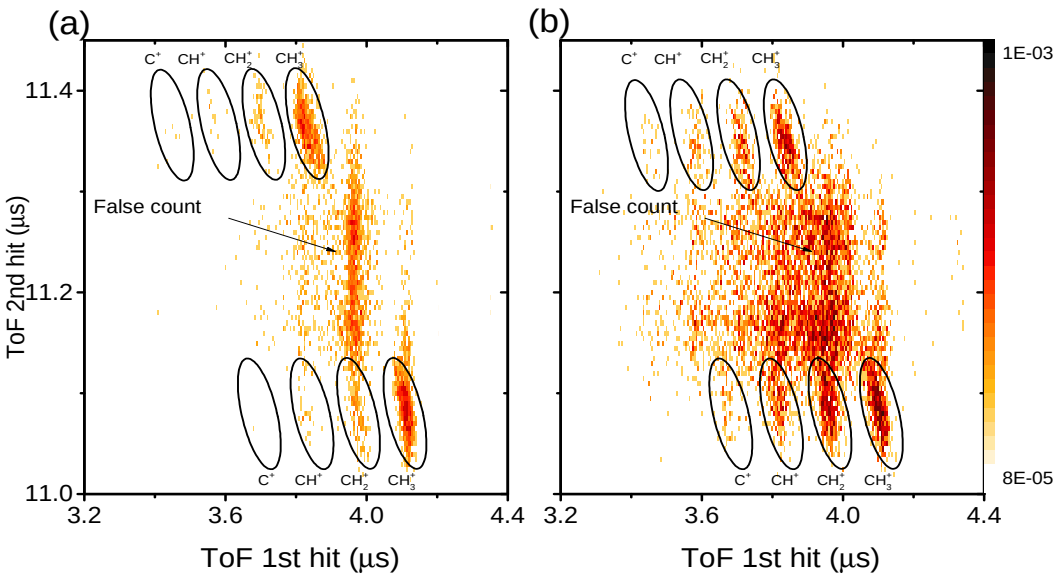

Fig. 5.3: Coincidence plot of the CH_n^+ ions and I^+ ions for (a) $\sim$ 25fs and (b) $\sim$ 1500fs

Effects of Pulse Duration Variation

Keeping the peak laser intensity fixed, spectra are obtained at various pulse durations from 25 fs to 1500 fs. Figure-5.4a shows the variation in the obtained yield as derived from the area under the peaks in the ToF spectrum. The yield of the parent molecular ion CH_3I^+ shows an insignificant variation with pulse duration as compared to the yield of other ionic fragments. A prominent change is seen for the high energy fragments in the $CH_n^+ + I^+$ islands, with a monotonic increase in their yields till about 1000 fs and then a saturation.

The method of changing the pulse duration also introduces dispersion in wavelengths within the pulse duration, that is, a chirp in the pulse. It is therefore important to verify that the observations noted above are mainly pulse-width dependent and that the role of chirp may be disregarded. Towards that, in Figure-5.5 we plot a 2D contour map of the ion yield for the main fragments at various grating position offsets (with respect to the grating position for shortest pulses). Positive offsets introduce a positive chirp of $\sim$ 4700 fs^2/mm. The spectrum at each grating position is normalized to total

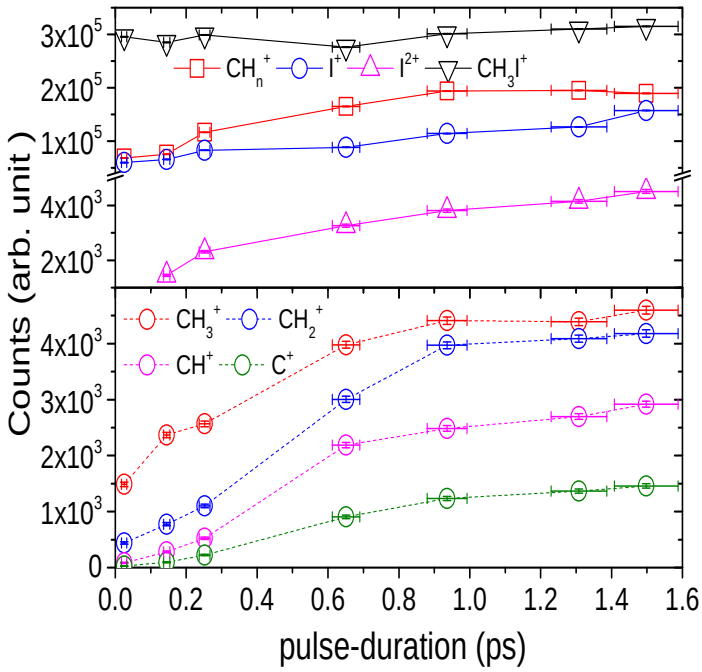

Fig. 5.4: (top) The measured absolute yields of the parent molecular ion CH_3I^+, CH_n^+, I^+ and I^{2+} ions, derived from the area under the corresponding peaks. (bottom) The absolute yields of CH_n^+ ions coming in coincidence with I^+ (bottom) with the increasing pulse duration obtained by summing the counts in the islands in photoion-photoion coincidence.

counts obtained for that setting. That the spectra are identical for positive and negative chirps indicates that in this intensity range and particularly for fragmentation products, the role of chirp may not be too significant.

5.4 Identification of Fragmentation Pathways

To get a clear idea about the participating electronic states in the dissociation processes, the complete kinetic energy distribution and the angular distribution of these ionic fragments are required. Using the spectrometer in an imaging condition the time-sliced velocity map images of the major ionic fragments are detected for various pulse durations with a constant peak intensity.

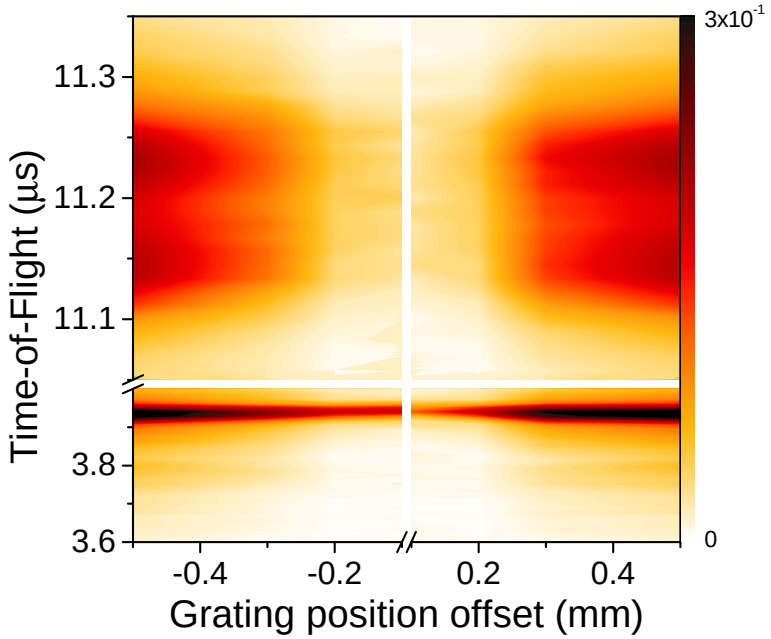

Fig. 5.5: A two-dimensional contour map of the ion time-of-flight spectrum (normalized with respect to the total counts) as a function of grating position offset. The offset is with respect to grating position for the shortest laser pulses. Negative offsets introduce negative chirps into the laser pulse and vice-versa.

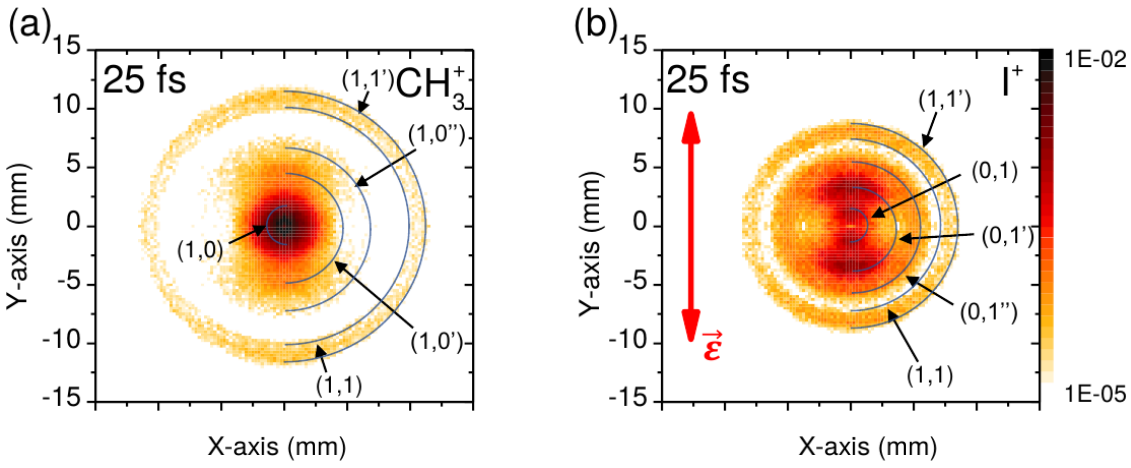

Fig. 5.6: Velocity Map Images of (a) CH_3^+ and (b) I^+ ions at the shortest pulse duration. The color scale for ion counts is logarithmic. The laser polarization axis (red arrow) is vertical. Semicircles identify different dissociation and CE channels.

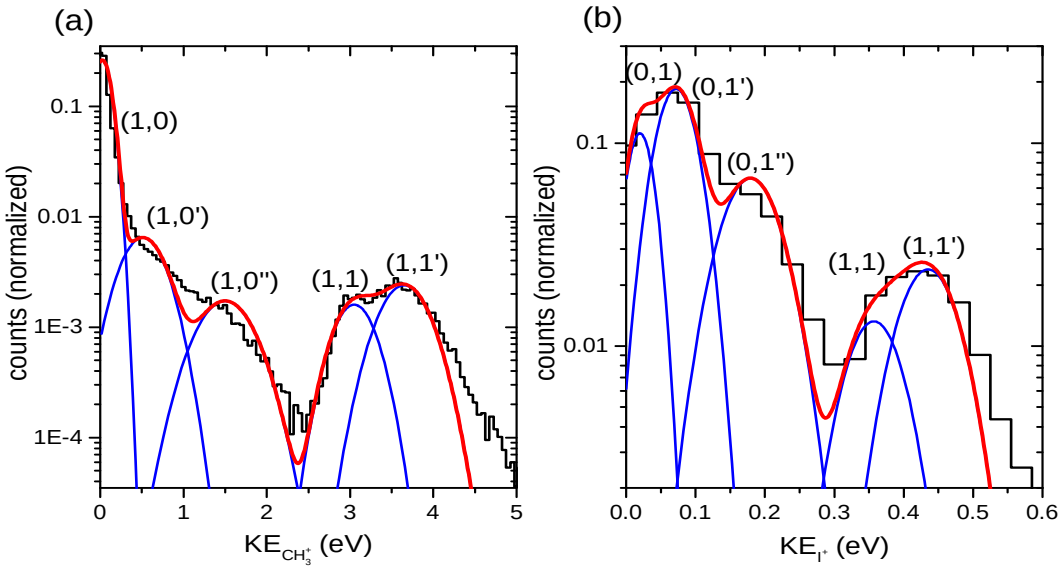

Fig. 5.7: The kinetic energy distribution (black histogram) of (a) CH_3^+ with multiple Gaussian fits (dashed blue and solid red curves) shown for a peak intensity of $\sim$ 5 TW/cm^2 with pulse duration $\sim$25 fs. The same for I^+ ions is shown in (b)

Figure-5.6a and b show the ion distribution map of the central velocity slice (ions ejected in the plane parallel to the detector and containing the laser polarisation axis) of the two major ionic fragments CH_3^+ and I^+ at the shortest pulse duration of $\sim$25 fs. The map shows two distinct segments, with a nearly isotropic outer ring distribution for high energy fragments and several dense distributions for the low energy fragments near the center.

Figure-5.7 shows the kinetic energy (KE) distribution of the ionic fragments obtained by integrating the counts over the azimuthal angle at each radius. The KE distributions (with low energy resolution) can also be obtained by appropriate transformation of the ToF spectrum for the energetic fragments observed in the photoion-photoion coincidence map. A close correspondence (shown in Chapter-3) of the latter KE distribution with that of the high energy fragments in the velocity map images allows us to identify the outermost ring as arising from the Coulomb explosion (CE) of the doubly charged parent ion. The low-energy ionic fragments are mainly due to the dissociation of the singly charged molecular ion into ionic and neutral fragments. All these break-up channels can be labeled in a (p,q) notation, where $p \geq 0$ denotes the charge states of CH_3^{p+}

ions and $q \geq 0$ does the same for I^{q+} ions. Multiple fragmentation channels for the same ion species are discriminated through a primed notation. We fit the KE distribution to a sum of Gaussian distributions corresponding to these (p,q) channels. Figure-5.7 shows the KE distribution of the CH_3^+ and I^+ ions at a pulse duration of $\sim$ 25 fs fitted with three Gaussian distributions for the low energy fragments and two Gaussian distributions for the CE fragments. While the two CE peaks are quite evident for the CH_3^+ fragments, the peaks cannot be distinguished for I^+ due to the reduced energy resolution for higher m/q. However, with higher intensity laser pulses, the CE channels are well populated. It should be noted that even at higher intensities, there is a relative variation in the yield of the channels, but no new channels are observed, and significantly, there is no shift in the peak positions for the CE channels either.

At the intensities used here, CH_3I^+ is populated largely in the spin-orbit split ground states $\widetilde{X}(1\ E_{3/2})$ and $\widetilde{X}(1\ E_{1/2})$. These states dissociate to give rise to CH_3^+ and the neutral I atom in the ground state. The higher excited state of $\widetilde{A}(2\ E_{1/2})$, which accounts for the near-zero energy I^+ ions, is also expected to be populated in the fast non-adiabatic ionization with the 25 fs laser pulses. To account for energetic fragments in dissociation, the involvement of higher excited states $\widetilde{B}(3\ E_{3/2}$ and $5\ E_{1/2})$ through a Floquet type few-photon coupling can be reasonably postulated. Probable dissociation pathways correlating with energies obtained from the Potential Energy Curves (PEC)(124) are listed in Table-5.1. These are not unique assignments, especially for low-energy channels. For example: CH_3I^+ $(1\ E_{3/2}) \leftrightarrow CH_3I^+$ $(5\ E_{1/2}\text{-}2\omega) \rightarrow CH_3^+ + I(^2P_{1/2})$ can also produce CH_3^+ ions with $\sim$0.5 eV of energy, in addition to other channels leading to same kinetic energy release. Here, the notation $(\langle ... \rangle \pm n\omega)$ indicates the dressing of the state with n laser photons. The bi-directional arrows indicate a coupling between the parent state and the dressed state. The molecular ion dissociates along the modified coupled potential curve which exists only as long as the laser field. In such a coupling, two modified potential curves arise resulting from the avoided crossing of the curves. On one of the curves, the molecule is stable against dissociation, known as bond-hardening while the other curve aids dissociation (bond-softening). The modified potential curves assigned for the dissociation channels here are those corresponding to bond-softening. The two CE channels at $\sim$2.9 eV and $\sim$3.5 eV are assigned to the repulsive electronic

Channel	Possible pathway	Kinetic Energy (KE)	Kinetic Energy Release (KER)		
(p,q)		CH_3^+	$KE_{CH_3^+} \times m_{CH_3I}/m_{I^+}$		
		eV	eV		
			Our Experiment	Zhang *et al.*	Liu *et al.*
$(1,0)$	$CH_3I^+ (2E_{1/2}) \leftrightarrow$ $CH_3I^+ (1E_{1/2} + 1\omega) \rightarrow CH_3^+ + I\ (^2P_{3/2})$	0.00	0.00	–	0-0.03
$(1,0')$	$CH_3I^+ (1E_{1/2}) \leftrightarrow$ $CH_3I^+ (5E_{1/2}$ - $1\omega) \rightarrow CH_3^+ + I\ (^2P_{1/2})$	0.51	0.58	–	0.42
$(1,0'')$	$CH_3I^+ (3E_{3/2}) \leftrightarrow$ $CH_3I^+ (1E_{1/2} + 1\omega) \rightarrow CH_3^+ + I\ (^2P_{1/2})$	1.5	1.68	–	–
$(1,1)$	$CH_3I^{2+} \rightarrow CH_3^+ + I^+\ (^3P_{1,0})$	2.9	3.2	3.6	3.1
$(1,1')$	$CH_3I^{2+} \rightarrow CH_3^+ + I^+\ (^3P_2)$	3.5	4.0	4.1	4.0

Channel	Possible pathway	Kinetic Energy (KE)	Kinetic Energy Release (KER)		
(p,q)		I^+	$KE_{I^+} \times m_{CH_3I}/m_{CH_3^+}$		
		eV	eV		
			Our Experiment	Zhang *et al.*	Liu *et al.*
$(0,1)$	$CH_3I^+ (1E_{3/2}) \leftrightarrow$ $CH_3I^+ (2E_{1/2}$ - $1\omega) \rightarrow CH_3 + I^+\ (^3P_2)$	0.02	0.19		–
$(0,1')$	$CH_3I^+ (2E_{1/2}) \rightarrow CH_3 + I^+\ (^3P_2)$	0.07	0.65	0.56	0.66
$(0,1'')$	$CH_3I^+ (3E_{3/2}) \rightarrow CH_3 + I^+\ (^3P_2)$	0.18	1.70	1.40	–
$(1,1)$	$CH_3I^{2+} \rightarrow CH_3^+ + I^+\ (^3P_{1,0})$	0.36	3.4	3.6	3.1
$(1,1')$	$CH_3I^{2+} \rightarrow CH_3^+ + I^+\ (^3P_2)$	0.43	4.0	4.1	4.0

Table 5.1: The possible dissociation pathways and the corresponding values of the peak KE obtained from the fits, and the Kinetic Energy Release (KER), defined as the sum of energy of the fragments. Our data is compared with that from previous studies by Zhang *et al.*(110) and Liu *et al.*(111)

states of the doubly charged parent ion leading to $CH_3^+ + I^+(^3P_{1,0})$ and $CH_3^+ + I^+(^3P_2)$ respectively, which matches well with previous studies(110; 111).

The ionic fragments I^{2+} arising from the dissociation of the di-cation or the CE of the tri-cation have also been collected in the imaging mode. In our experiments we failed to see any I^{2+} ions at $\sim$ 25 fs, indicating that a direct generation of CH_3I^{3+} at these intensities is not feasible. Figure-5.8a shows the velocity distribution of the I^{2+} ions for $\sim$150 fs pulse duration with the same peak intensity as before. The KE distribution of the I^{2+} ions shown in Figure-5.8b, is fitted with three Gaussian distributions,

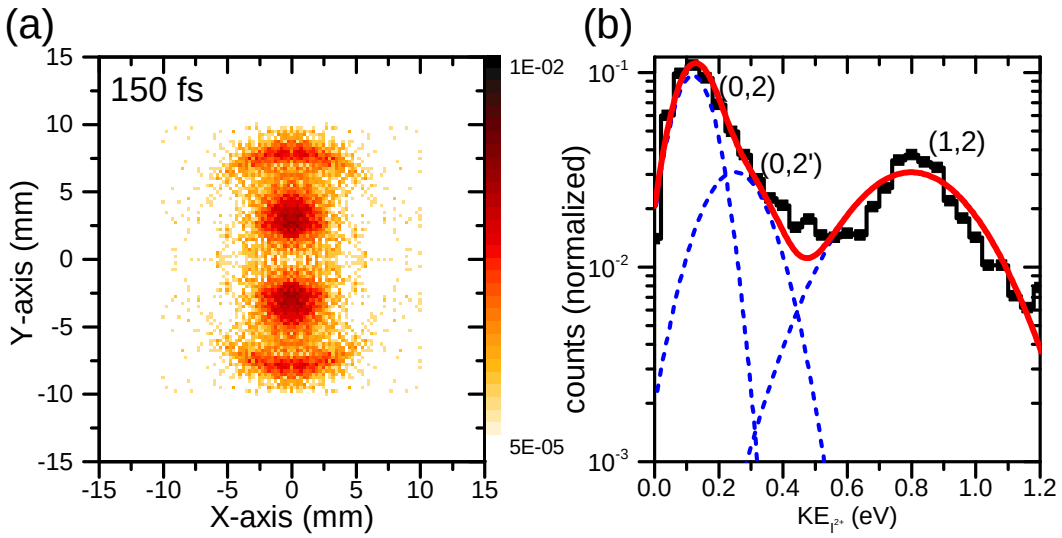

Fig. 5.8: (a) The Velocity Map Images of I^{2+} ions at pulse duration $\sim$ 150 fs with peak intensity $\sim$ 5 TW/cm^2 and the corresponding kinetic energy distribution (b) (black histogram) with multiple Gaussian fits are shown in dashed blue and solid red curves.

two for the low energy fragments and one for the rest. The peak at $\sim$0.2 eV can be associated with the asymmetric dissociation of CH_3I^{2+} ions through $(0,2'')$ CH_3I^{2+} $(\widetilde{X}\ ^2E_{1/2}) \rightarrow CH_3 + I^{2+}$ $(^4P_{3/2})$ channel. However, the origin of the other low energy channel with a mean KE of $\sim$0.1 eV is yet unknown. The high energy peak ($\sim$0.8 eV) corresponds to a Coulomb explosion channel $(1,2)$. This is confirmed by evaluating the KE of the fragments in the ToF spectrum filtered for ions in the $CH_n^+ + I^{2+}$ island. The assignment is also in agreement with previous studies. Corrales *et al.*(109) assigned the same channel $CH_3I^{3+} \rightarrow CH_3^+ + I^{2+}$ $(^2P_{1/2})$ to a KE distribution peaking at $\sim$1 eV. This higher KE (as compared to our observation and others) has been attributed to the low pulse durations (50 fs) and higher intensities in their studies.

The formation of I^{2+}, itself indicates a strong pulse duration dependence as at this intensity I_0, the chance of creating tri-cationic states is negligible for the shortest pulse duration of $\sim$25 fs. To get a clear pulse duration dependence on the dissociation process, the time-sliced velocity map images of these major ionic fragments are required.

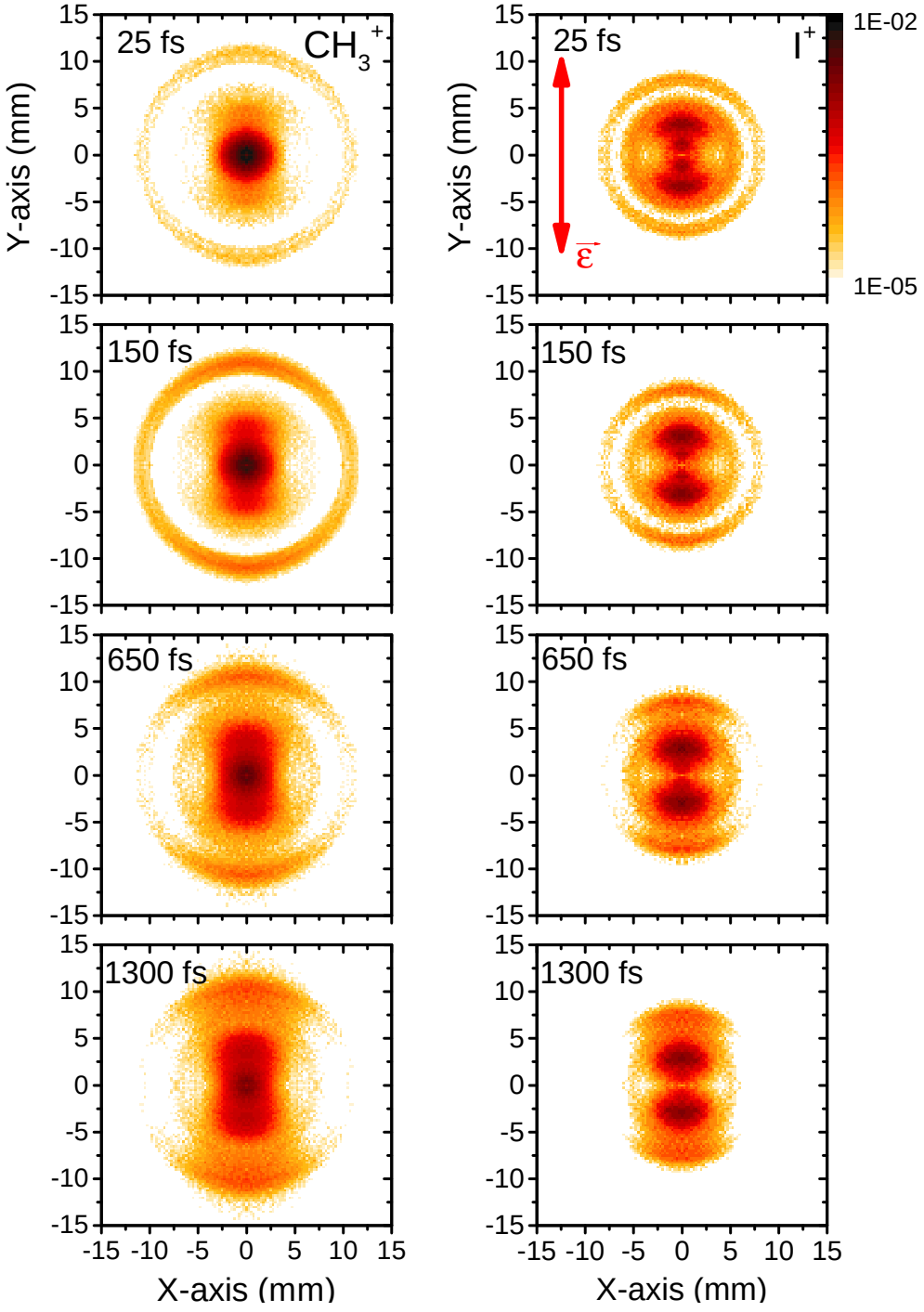

Fig. 5.9: Time sliced velocity map images of [left panel] CH_3^+ and [right panel] I^+ ions recorded at different laser pulse durations.

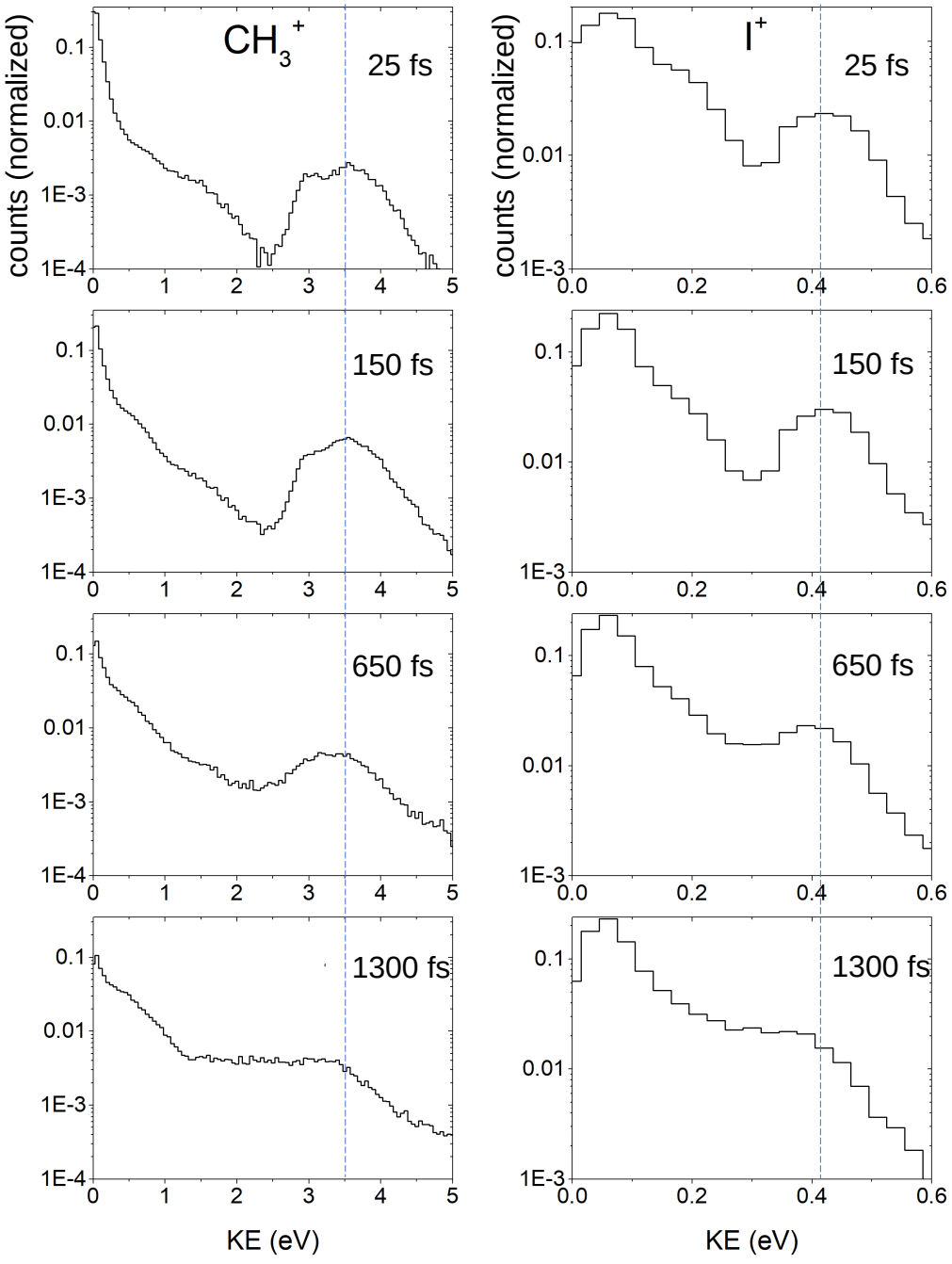

Fig. 5.10: The kinetic energy distribution of [left panel] CH_3^+ and [right panel] I^+ ions obtained at different pulse durations from the associated time sliced velocity map images. The dashed vertical lines are placed to highlight the peak shift with increasing pulse-duration.

Effects of Pulse Duration Variation

As a function of pulse duration, the relative intensities of the dissociation channels change, but no new channels arise, and no shifts in their energies are seen (see Figure-5.9 highlighting the three-dimensional ion velocity distributions of CH_3^+ and I^+ ionic fragments for the pulse durations of 25 fs, 150 fs, 650 fs and 1300 fs keeping the same laser intensity as before). However, we note that the CE channels $(1,1)$ and $(1,1')$ merge and shift towards the lower energies with increasing pulse duration. The KER of the CE channels progressively reduces from 3.6 eV and 4.1 eV (at 25 fs) to an unresolved broad peak at 3.2 eV (at 1500 fs). Furthermore, the nearly isotropic distribution becomes anisotropic as the pulse duration increases. The relative yield of these CE channels also increases with pulse duration, in line with the observations made in ToF mode (see Figure-5.4). In the ToF mode, we also observe an enhancement in yields of de-hydrogenated methyl fragments CH_m^+ $(m = 0–2)$. The kinetic energy of these energetic ionic fragments coming in coincidence with I^+ ions can be estimated from the associated ToF spectrum. The kinetic energy distribution of these de-hydrogenated methyl ionic fragments for the longest pulse duration ($\sim$ 1500fs) has been shown in Figure-5.11. The corresponding mean kinetic energy for these de-hydrogenated methyl ionic fragments are: $\sim$ 2.9 eV of CH_3^+, $\sim$ 2.8 eV of CH_2^+, $\sim$ 2.7 eV of CH^+, and $\sim$ 2.6 eV of C^+. The trend in the mean kinetic energy of these de-hydrogenated methyl ionic groups $KE_{CH_3^+} > KE_{CH_2^+} > KE_{CH^+} > KE_{C^+}$ remain unchanged with pulse duration variation. The mean KE ordering of these de-hydrogenated remains unchanged with increasing pulse duration. We note here that the resolution of the spectrometer in the ToF mode is 0.08 eV (87) for these conditions. The relative mean kinetic energy difference between these de-hydrogenated methyl ionic fragments is found to be independent of the pulse duration of the laser pulse. These observations suggest that these de-hydrogenated ionic fragments arise from the CH_3^+ ions by step-wise dissociation. Step-wise dissociation of the parent CH_3^+ ion occurs just after the Coulomb Explosion of the dicationic Methyl Iodide and the possible dissociation pathways are like(111):

- $CH_3^+ \rightarrow CH_2^+ + H$
- $CH_2^+ \rightarrow CH^+ + H$

- $CH^+ \rightarrow C^+ + H$

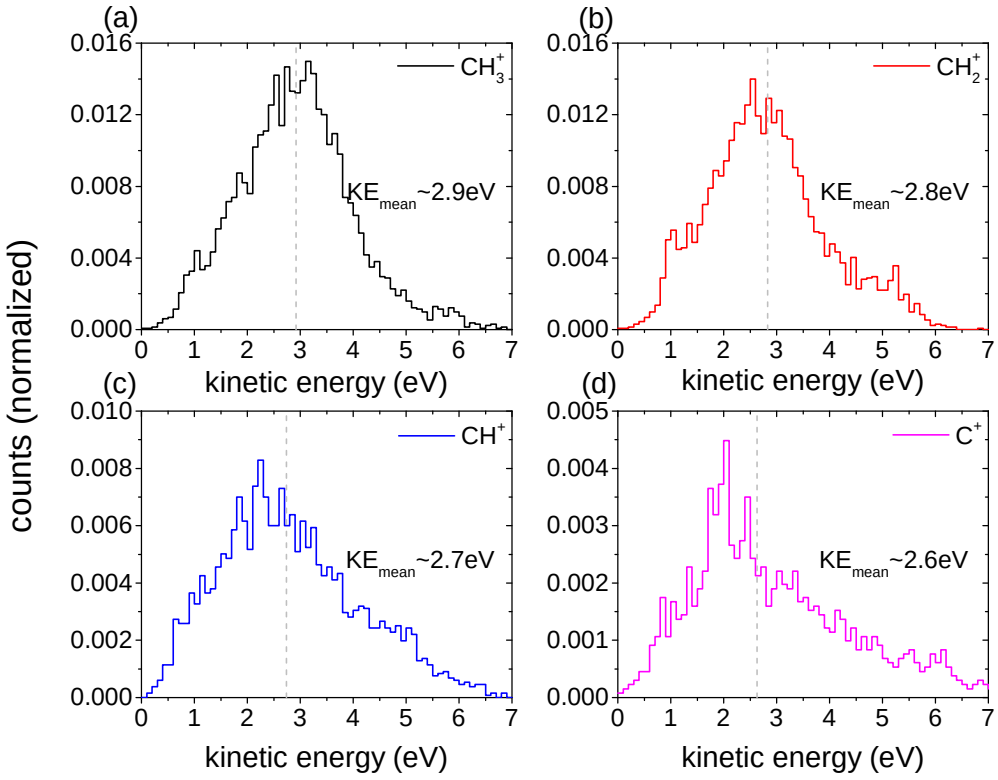

Fig. 5.11: The normalized KE distribution of the de-hydrogenated ions (a) CH_3^+, (b) CH_2^+, (c) CH^+, (d) C^+ with respect to the total CH_n^+ counts coming in coincidence with the I^+ observed for the longest pulse duration in the photoion-photoion coincidence plot. The corresponding mean values of the distribution are highlighted in the plots with a dashed vertical line.

In the above-mentioned dissociation processes, the neutral H-atom is removed in each step and it carries away a small amount of energy which causes the shift in the kinetic energy of these de-hydrogenated ionic fragments.

In our experiments we failed to see any I^{2+} ions at $\sim$ 25 fs, indicating that a direct generation of CH_3I^{3+} at these intensities is not feasible. No significant change in the angular distribution with increased pulse duration is observed for the CE channel (1,2). However, the yield increases and the CE peak shifts towards lower energy (0.6 eV at 1500 fs).

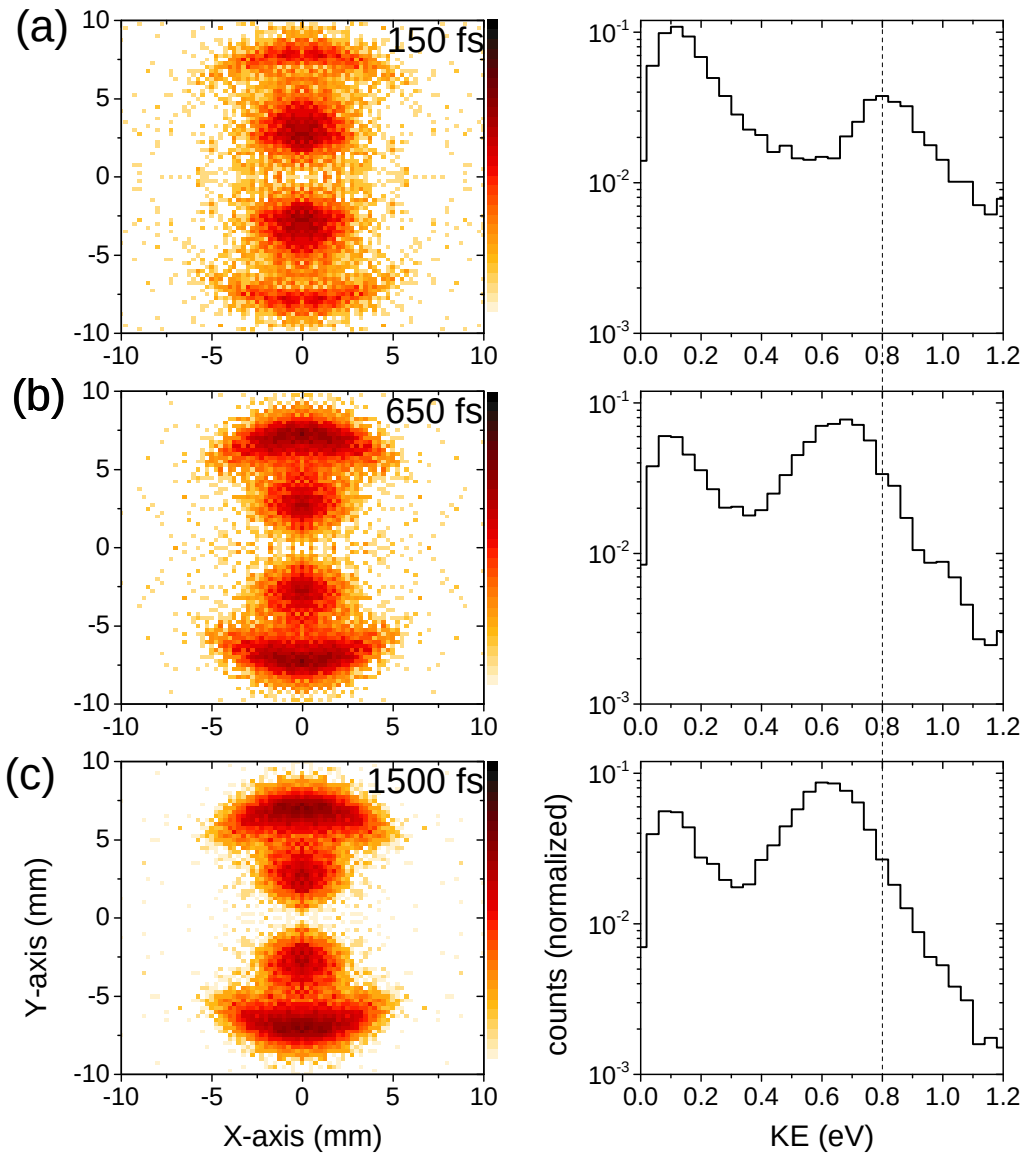

Fig. 5.12: Time sliced velocity map images of [left panel] I^{2+} and [right panel] the kinetic energy distribution associated with time sliced velocity map images recorded at different laser pulse durations. The dashed vertical line is placed to highlight the peak shift with increasing pulse-duration.

5.5 Time-Evolution of The Intermediate States

In the interaction of CH_3I with an ultrashort laser pulse of 25 fs duration in the moderate-intensity regime between 10^{12}-10^{13} W/cm^2, the ion is predominantly formed in the spin-orbit coupled CH_3I^+ $\widetilde{X}(1E_{3/2}$ and $1E_{1/2})$ states by removing a single electron from the outermost orbital ($2e$). This is a rapid, non-adiabatic Frank-Condon type transition. The low energy dissociation channels at the shortest laser pulse provide evidence that the low lying excited states: $\widetilde{A}$ $(2E_{1/2})$ state, and $\widetilde{B}$ states $(3E_{3/2}$ and $5E_{1/2})$ are also populated through direct ionization. The rapid non-adiabatic ionization to any of these electronic states results in multiple ro-vibrational levels being excited by the laser pulse. A ro-vibrational wavepacket evolving in time along the potential energy surface of the electronic state is initiated, mainly along the coordinate defined by the inter-nuclear separation C-I. For the di-cation states too, direct ionization at the equilibrium geometry is predominant for short pulses. However, sequential ionization from the intermediate mono-cationic states should also be considered, particularly for longer laser pulses. It is therefore conceivable that the yield of the subsequent CE is also modulated by the evolving dynamics of the intermediate state. For example in pump-probe studies, Malakar et al.(115), have observed through CEI, the C-I stretches vibrational mode (ν_3) in the $\widetilde{A}$-state of CH_3I^+. A consequence of this bond stretch in the molecule is an unequal shifting of the energies of molecular orbitals relative to each other.

5.5.1 Photon Induced Orbital Coupling

We propose that the variation in the yield and angular distributions as seen in the CE channels here reflects these dynamics. Detailed multi-configuration (MC) self-consistent (SCF) based calculation is carried out using the quantum chemistry package GAMESS in the field-free condition. We have calculated the variation of the orbital energy of outer orbitals due to C-I bond stretching with fixed geometry of CH_3 group. The MCSCF calculation was performed using Pople's N-21G split valence basis set with NGAUSS=3. The calculation shows (see Figure-5.13) an energy uplift of the in-

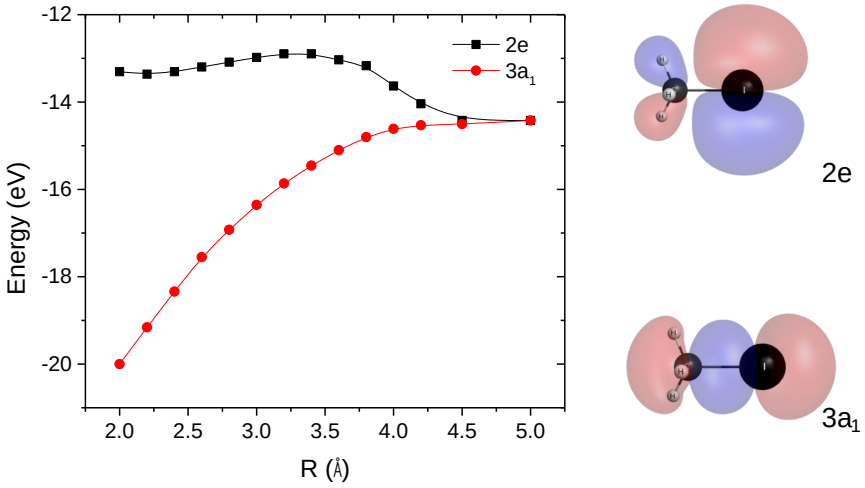

Fig. 5.13: The energy of the HOMO $2e$ and HOMO-1 $3a_1$ orbitals of the monocationic Methyl Iodide obtained from MCSCF calculation. The orbital structres of $2e$ and $3a_1$ orbitals are shown in the right panel.

ner HOMO-1 ($3a$) orbital of the CH_3I^+ ion with increasing bond distance. The HOMO ($2e$) and HOMO-1 ($3a$) orbital merge near $\sim$ 4.5 Å. However, at r_c $\sim$3.9 Å the energy difference equals that of the laser photon energy, $\sim$1.5 eV, at which point the two orbitals could be efficiently coupled in the presence of the laser field. We propose that the variation in the yield and angular distributions as seen in the CE channels here occurs due to the orbital coupling in the presence of the laser field.

5.5.2 Classical Model

The time evolution of the intermediate state can be visualized by a simple classical model by estimating bond-stretching with time and it is shown in the Figure-5.14. The molecular ion can be considered as a classical particle with the reduced mass 'μ', moving over the PEC $V(r)$, defined by the C-I bond separation coordinate r(116). The dynamics of the particle can be tracked by solving the equation of motion $d^2r/dt^2 = -1/\mu \times dV(r)/dr$ over the electronic state. Assuming a Frank-Condon type transition to the corresponding state from the ground state of the neutral CH_3I molecule at ionization, the C-I bond length is taken to be equilibrium bond -length $r_e \sim 2.14$ Å at initiation $t = t_0$. At this intensity regime the formation of monocations over $\widetilde{A}$ state is

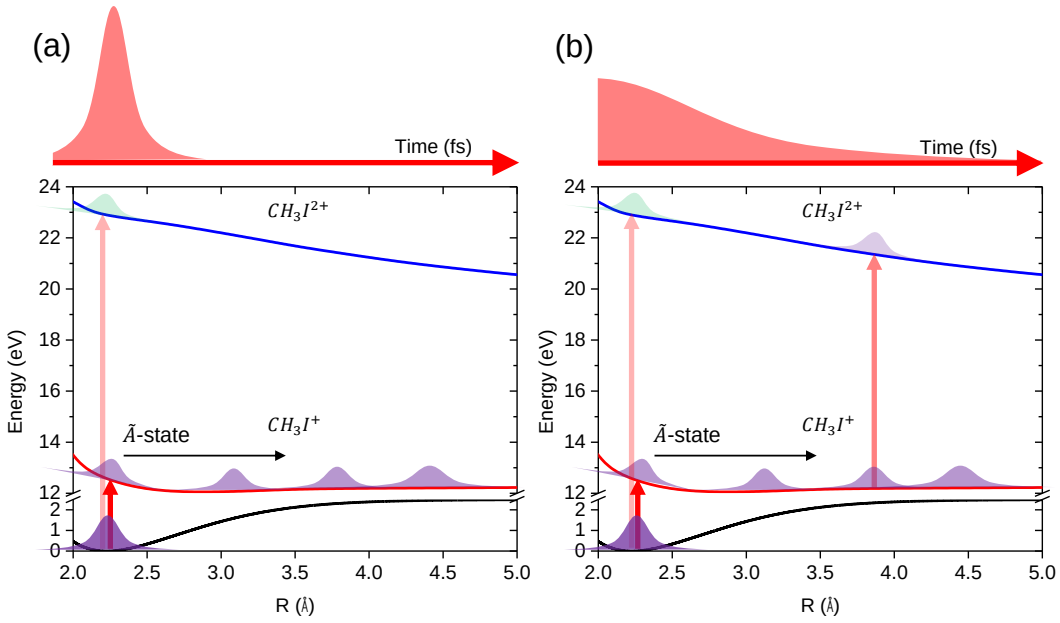

Fig. 5.14: (a) and (b) show a schematic of the dissociative wavepacket dynamics over $\widetilde{A}$-state along the C-I axis. In the case shown on the left, the short pulse prevents any coupling at later times, while in the case shown on the right, the extended pulse permits one photon orbital coupling at 3.9Å

most probable and it is shown here with the bright red arrow. Now, the evolution of the intermediate state $\widetilde{A}$ being populated following the ionization event of being populated at 2.14 Å. It takes about 70 fs for the C-I bond to stretch to 3.9 Å. With a 25 fs laser pulse, there is negligible laser intensity at this point. However, with longer laser pulses, the two orbitals could be resonantly coupled. In the coupled state, spatial localization of electrons can increase the ionization probability and depend on the geometrical overlap, the symmetry of the orbitals, and the orientation with respect to the laser polarization direction. With longer pulses, both the coupling and the subsequent ionization are likely to be enhanced. Then, the ionization probability of the cation in response to a single cycle laser pulse of wavelength 800 nm ($\hbar\omega = 1.55$ eV), at the bond-length r can be considered to be of the form :

$$P(r) \sim \exp\left[\frac{\Delta E(r)}{\Delta E(r) - \hbar\omega}\right]^2 \tag{5.1}$$

peaking around $r_c = 3.9$ Å. Here $\Delta E(r) = (E_{2e} - E_{3a_1})$ is the energy difference between the HOMO and HOMO-1 orbital. The contribution to the multiple ionization signal for

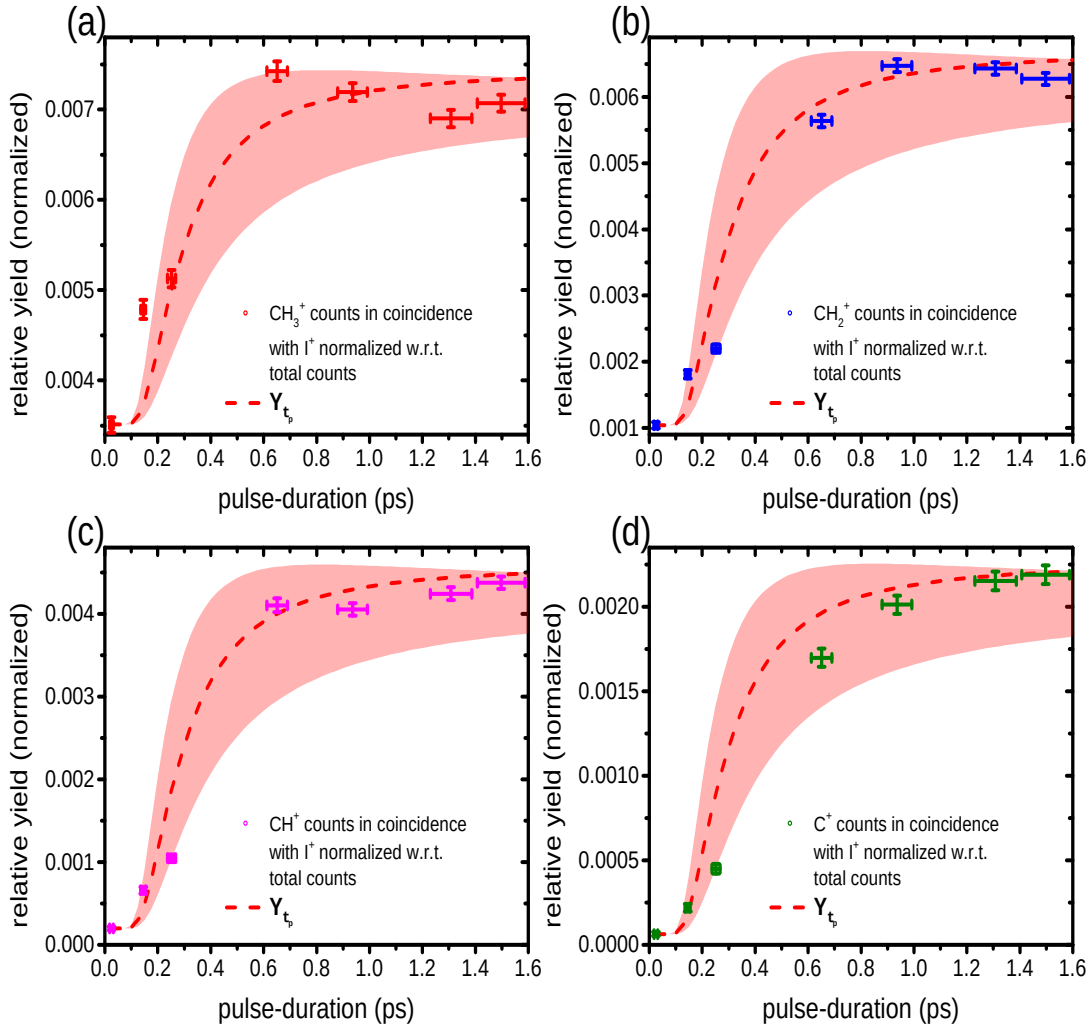

Fig. 5.15: The relative yield of de-hydrogenated methyl ionic fragments (a) CH_3^+, (b) CH_2^+, (c) CH^+, (d) C^+ in coincidence with the I^+ ions with respect to the total ion yield as a function of pulse duration. The calculated ionization probability as a function of pulse duration, based on a semi-classical model accounting for enhanced ionization due to a resonant coupling at an inter-nuclear separation of $\sim$3.9 Å, is shown as a red solid line. The shaded region shows the range of values of the ionization probability corresponding to different single ionization instants within $\pm$ 10% of the laser peak.

a multi-cycle laser pulse of duration τ_p would therefore be proportional to

$$Y_{\tau_p} = \int_{t_0}^{\infty} [I_{\tau_p}(t) \times P'(t)]\, dt$$

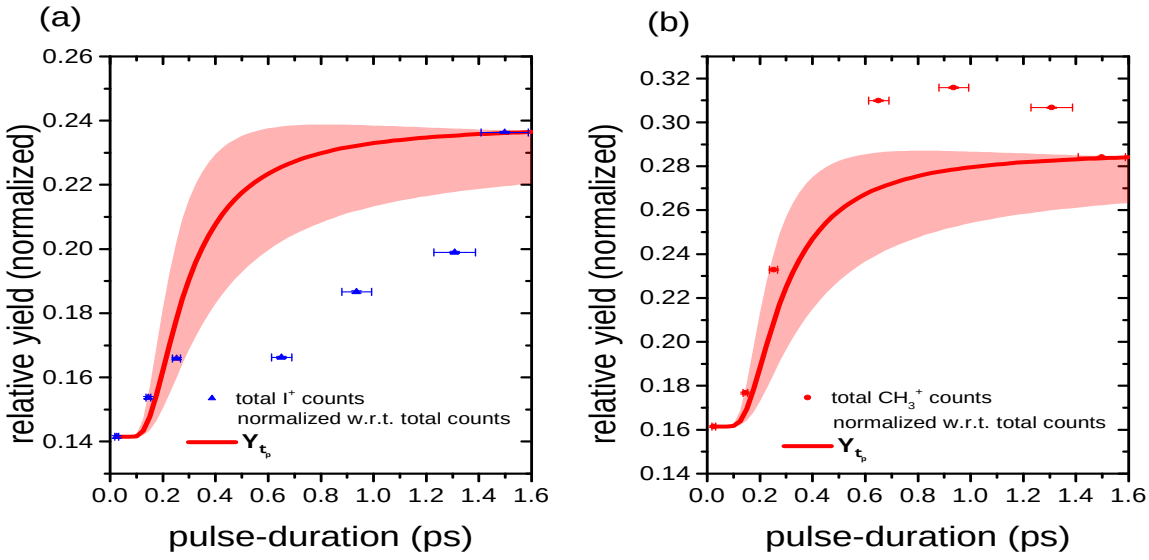

Fig. 5.16: The relative yield of the total I^+ and CH_n^+ ionic fragments with respect to the total ion yield as a function of pulse duration. The calculated ionization probability as a function of pulse duration, based on a semi-classical model accounting for enhanced ionization due photo induced multi-orbital coupling is shown as a red solid line. The shaded region shows the range of values of the ionization probability corresponding to different single ionization instants within $\pm$ 10% of the laser peak.

(5.2)

$I_{\tau_p}(t)$ is the cycle-averaged envelope of the laser intensity. The ionization probability at any time t, $P'(t)$ is arrived at by computing the classical bond separation r at t using the PEC for the $\widetilde{A}$ state and thereby $P(r)$. For smaller values of τ_p, Y_{τ_p} would be small, as $I_{\tau_p}(t_c)$ is small at the peak of probability function, r_c. With increasing τ_p, the integrated yield would increase rapidly as the field at $r = r_c$ increases. However, with fixed peak intensity, beyond a certain τ_p, the increase in yield will be marginal, as the increased laser field beyond $r = r_c$ has negligible contribution to Y_{τ_p}. Calculated values of Y_{τ_p} are shown in red in Figure-5.15 and compared with the experimental yield of the energetic coincident ions for the CH_n^++I^+ islands. Here the experimental data are normalized to total counts in the ToF spectrum, while the Y_{τ_p} is scaled to match the extreme values of the normalized data. The solid red curve represents calculations considering the initia-

tion of the wavepacket motion, t_0, that is the single ionization event, occurs nominally at the peak of the laser pulse. The shaded band shows the variation in calculated yield resulting from a $\pm 10\%$ fluctuation in the instant of ionization around the laser peak. The model calculations have also been compared with the total counts for CH_3^+ and I^+ ions (Figure-5.4 (upper panel)) and the correspondence (shown here in Figure-5.16) is poor. This is not surprising as the total counts also contain ions from the dissociation from the single charged species.

5.6 Discussion

Multi-orbital ionization imposes stringent conditions on the angular distribution of the fragment ions. The observed angular distribution of the CE channels at the shortest laser pulse of 25 fs shows a nearly isotropic distribution, which is expected if the main contribution for the ionized electron is the outermost HOMO ($2e$) orbital. The velocity distributions in Figure-5.9 (left panel) of CH_3^+ for different pulse durations show the two CE channels broaden and shift towards the lower energy for pulses >650 fs and the angular distribution becomes increasingly anisotropic. It follows that the involvement of HOMO-1 ($3a$) orbital increases for larger pulse durations. The $3a$ orbital distributed close to the inter-nuclear axis will be easily ionized if the laser polarization axis is parallel to the C-I bond, and hence, the large anisotropy in the observed CE ion distribution. From the angular distribution, we can attest that the dominant contribution at longer pulses to CE appears to be due to ionization from the $\widetilde{A}$ state, with the $3a$ orbital being increasingly involved at larger inter-nuclear separations.

The (1,2) channel arises from the CE of the tri-cationic state of the Methyl Iodide. At these low-to-moderate intensities, direct ionization to the tri-cationic state would be highly improbable. Sequential, enhanced ionization due to a stretch in the C-I bond is, therefore, a plausible explanation. We propose that a similar up-shifting of orbital energy in the intermediate $\widetilde{A}$ enhances the ionization probability and is responsible for the formation of the tri-cationic state. Figure-5.8 shows the I^{2+} ions arising from CE at a pulse duration of $\sim$ 150 fs with a broad energy distribution peaked at $\sim$0.82 eV and the

angular distribution strongly peaked along the laser polarization axis. This anisotropic angular distribution suggests dominant HOMO-1 ($3a$) contribution to the ionization. However, the HOMO-1 contains only one electron in the $\widetilde{A}$ state configuration. It is possible that the second electron is contributed by the HOMO or HOMO-2 orbital, but the highly anisotropic angular distribution observed makes it unlikely. On the other hand, in the presence of the laser field, especially when the $2e$ and $3a$ orbitals are resonantly coupled when $r \approx r_c$, inter-orbital electron transfer $3a \leftarrow 2e$, can occur(42; 125). So subsequently, both the electrons in the $3a$ orbital can be removed, more easily for molecular ions aligned parallel to the laser polarization axis than for other orientations, leading to the strongly anisotropic angular distribution.

The de-hydrogenated methyl ionic fragments also show similar enhancement with pulse duration increase as shown in Figure-5.4 (bottom panel). As pointed out earlier, the kinetic energy distributions suggest step-wise dissociation from the parent CH_3^+ ions by releasing neutral H-atoms at each dissociation step. The increasing anisotropy in the angular distribution of the precursor methyl ion points to the increasing involvement of the $3a$ orbital, aligned to the laser polarization axis, in the formation of the dicationic charge state of the CH_3I. The aligned molecule gets distorted from its tetrahedral structure due to the external electric field to that of the extreme turning point of an umbrella-mode vibration, that the three hydrogen atoms come closer together in this mode(126; 127). Such umbrella-mode vibration could initiate the step-wise dissociation and as the contribution of the pre-aligned molecules increases significantly in the Coulomb explosion with increasing pulse duration, so would the sequential dissociation of the methyl ionic fragments. A close correspondence of the C^+ yield with the model calculations (see Figure-5.15d) also supports our speculation. The formation of atomic fragments at such low laser intensities in sub-ps laser pulses is significant and merits an involved analysis, which cannot be captured by the classical and phenomenological approach here. The possible role of intermediate electronic states also needs to be investigated. Quantum calculations, involving the rich dynamics of transient species with varying geometries are essential to the understanding and out of the scope of this paper(128).

A discussion on the role of wavelength dispersion in the laser pulse (chirp) is pertinent here. We have noted that the yield of the fragmentation products and their mean energies both for dissociation and CE is independent of the sign of the chirp. This is to be contrasted with experimental and theoretical results(129; 130), wherein the role of chirp is distinguished by the difference in yields and changes in the mean energy of the products as a function of the sign of the chirp. For example, the central wavelength of the laser is 800 nm, and a bandwidth of 50 nm corresponds to photons in the energy range of 1.55 ± 0.05 eV. For dissociation channels, with transitions induced by one photon, the change in the kinetic energy release with the dispersed wavelength will cause a change in KER by ± 0.05 eV. However, no such shift for the dissociation energies is seen here, possibly merged in the thermal energy spread (± 0.025 eV) of the effusive molecular target. A significant shift ($\sim$ 1 eV) in the energies of the ions is only visible for the CE channels. The effective bandwidth due to multi-photon ($n = 15$) absorption to the dication states is $\pm$ 0.73 eV. Hence, only the ground, $2E + A_1$, and two excited states of CH_3I^{2+}, $E + A_2$ and A_1, are accessible within the bandwidth. With increasing dispersion, no new upper electronic levels will be accessible, which could have accounted for a possible change in ionization probability. Furthermore, with a positively chirped laser pulse, high-frequency components arrive after the peak of the laser pulse. So, the di-cation and tri-cations would form with higher excess energy than that due to the central wavelength photons. Consequently, with increasing positive chirp, the energy of the fragments would increase. Conversely, a negative chirp would see a drop in the fragment ion energy. Neither of these possibilities is supported by our data, and we are justified in neglecting the role of dispersion in our interpretation.

The fair correspondence of the model calculations with the yield of the high-energy fragments needs to be qualified with some caveats. The classical model assumes ionization occurs near the peak of the laser pulse, within $\pm$ 10% of the laser peak. The assumption holds true for shorter pulses, but may not be valid for longer pulses. Experimentally, however, our observation is that, by keeping the peak intensity the same, the yield of the parent molecular ion CH_3I^+ does not change with increasing pulse duration. Furthermore, as is seen from the velocity map images, there are subtle changes in the yields of the various dissociation channels, but no new channels are observed, even

with increased intensity. So, in this intensity range and in the NIR wavelength regime, it may be reasonable to assume that the low lying bound electronic states are populated non-adiabatically at the shortest pulse duration, 25 fs, are the same as those observed for larger pulse duration.

The model, ascribing the ionization probability to a form as chosen above is as yet without a sound theoretical basis. A critical inter-nuclear distance at, or beyond which there is an enhanced ionization probability, has been associated with many molecules. In associating the critical distance to a laser-induced orbital coupling at $r_c = 3.9$ Å we refer to other theoretical studies to guess the form of the ionization probability(121). Conventionally, the experimental estimate of the critical distance is obtained by considering r_c as the distance of two point charges separated before the explosion and to equate the measured CE through $r_c(\text{Å}) = 14.4 \times (p \cdot q)/KER(eV)$. This yields a range of $r_c =$ 3.6-4.2 Å from our measurements and from previous studies(110; 111). The choice of r_c therefore does not disagree with these observations. Nevertheless, it must be stated that a pump-probe experiment with carefully chosen intensities should be considered definitive to extract the critical distance.

We also point out that the model estimate for the yields at lower pulse durations deviates from the experimental results, which could be due to various reasons. Primarily, we have neglected the role of direct ionization, which is seen to have a non-trivial contribution for the CH_n^++I^+ yields, at low pulse durations. There could also be errors in the PEC due to the fixed geometry assumption taken for the Methyl group leading to erroneous calculations. The choice of the intermediate $\widetilde{A}$ state is justified by considering previous studies and keeping in mind the timescale of the dynamics. For example, in the repulsive state, $\widetilde{B}$ the time evolution of the wavepacket is as expected much faster, dissociating within $\sim$100 fs. In any case, the classical model serves only as an empirical guide to support our hypothesis is better and Time-Domain-Schrodinger-Equation solutions are essential to confirm the pathway assignment to the KER observed. Furthermore, if we strictly consider the symmetries of the orbitals involved, laser-induced dipole coupling between the orbitals parallel to the laser polarization direction is improbable. A Time-Domain-Density-Functional-Theory approach may hence be neces-

sary to tackle the issue.

5.7 Summary

CH_3I, interacting with moderate intensity laser pulses (5×10^{12} W/cm^2, 25 fs-1500 fs) is mainly singly ionized with a significant fraction of these ions further dissociating in the laser field. But even at these low energy densities, di-cationic and even tri-cationic states can be formed with longer duration laser pulses (>150 fs). Our investigations, through ion imaging of the fragments, aided with a simple classical 1-D model suggest that a considerable contribution to this is through delayed sequential ionization in an intermediate state, $\widetilde{A}$ in the mono-cation. With increased C-I bond-separation, triggered at the formation of the ion, the inner $3a$ orbital upshifts in energy. If sufficient laser intensity exists, a resonant coupling is possible, even favoring pumping of the electron: $3a \leftarrow 2e$. Thus, longer laser pulses can further populate repulsive states of the CH_3I^{2+} and CH_3I^{3+} ions(131). A well-studied molecular system such as CH_3I is a source of rich and varied dynamical processes. Observations of some of these dynamics, reported here need to be investigated in detail, both experimentally and theoretically in future work.

CHAPTER 6

SUMMARY AND FUTURE OUTLOOK

6.1 Summary of The Present Work

In the presence of intense, ultrashort laser pulse molecules go through dissociation followed by ionization, and this process proceeds via several photon-coupled transient electronic states. During this fragmentation process, the molecular system exhibits various dynamical behaviour in the presence of the laser field. The dynamical processes happening during the dissociation of a molecular system can be investigated by detecting electrons or ionic fragments arising from the interaction of molecules with the laser field. In this thesis work mainly ion detection technique is used to understand the dynamical behaviour of molecules in the presence of a laser field. For this purpose, simultaneous measurement of velocity and angular distribution of the ionic fragments are required, and it can be achieved by the Velocity Map Imaging technique developed by Eppink and Parker in 1998(23). Using a Velocity Map Imaging Spectrometer, the entire 3-D momentum distribution of the ionic fragments is mapped on a 2-D planar detector, which detects the time of flight and position information of the ionic fragments on the detector. This type of ion imaging spectrometer contains special ion lens optics, which, for a given setting, projects fragment ions of a particular species to the same radius on a planer detector. The complete 3-D information can be recovered by choosing events that have a near-zero velocity component parallel to the spectrometer axis in the post-experiment processing. The time-sliced 2-D velocity images contain concentric circular rings and each of them corresponds to different kinematics. The distribution of intensity along the ring gives the angular distribution wrt the laser polarization and the angle-integrated radial distribution gives the kinetic energy distribution.

To investigate the post-ionization dynamical processes happening over the excited electronic states, two different molecular systems, O_2(106) and CH_3I(131) have been

chosen to highlight two different aspects of the transient electronic processes in the dissociation dynamics. The dissociative ionization of Oxygen molecule in the intense ($\sim$ 10-100 TW/cm^2), ultrashort ($\sim$ 25 fs) 800 nm laser pulse shows that the angular distribution shows stronger peaking along with the laser polarization, as the laser intensity is increased. It indicates the alignment of O_2^+ ion is caused by the rotational kick experienced after the ionization due to the remnant of the laser pulse as a consequence of the induced dipole moment in the O_2^+ ion. However, a counterintuitive scenario is observed in the presence of $\sim$ 35 fs laser pulses of 400 nm. The observed angular distribution of the ionic fragments emerging from O_2^+ in the presence 400 nm pulses does not change for the comparable intensity range employed for 800 nm laser pulses. This striking difference suggests an anomalous hindering of alignment of the O_2^+ ion in the presence of 400 nm laser pulses. For both cases, the possible dissociation pathways are assigned based on the measured kinetic energy distribution and the available potential energy curves of the molecular Oxygen ion. Using a simple semi-classical model of dynamic alignment including the static polarizability of the participating excited electronic states, both the behaviour under 800 nm as well as 400 nm are reproduced. The difference in the observations can be explained as being due to the transient negative polarizability associated with an intermediate state of the proposed pathways mentioned for the interaction with 400 nm laser pulses. Based on the quantum chemistry calculation, we find that the structural electronic correlation in the presence of an external electric field is responsible for this behaviour. These results are a fascinating illustration of electron correlation unfolding through the rotational dynamics during dissociation of molecular O_2^+ ion.

The above-mentioned dissociation dynamics observed in molecular Oxygen ion happens within 25 fs, and time-resolved investigations become difficult with a laser pulse duration greater than the dissociation time-scale. However, the dissociation time-scale gets longer for heavier molecules, and the dynamical properties can be easily resolved with a $\sim$ 25 fs laser pulse. Time evolution of dissociation is generally studied by time-resolved studies like the pump-probe experiment, where a single pulse (pump) ionizes and populates over one of the excited states, which is under study, and then a second pulse (probe) is applied after the first pulse with some time delay to probe

the dynamics over this excited state. However, similar information can be obtained by stretching a single pulse over a wide range from femtosecond to picosecond regime systematically by keeping a constant peak intensity. For this purpose, a much heavier, prototype molecular system CH_3I has been chosen. In moderately intense ($\sim$ 5 TW/cm^2) laser field CH_3I goes through ionization and eventually dissociates into ionic fragments. For the shortest pulse duration ($\sim$ 25 fs), mostly the monocationic CH_3I are formed, however, a remarkable observation is that, when longer laser pulses (> 150 fs) are introduced, higher charged states (charge state $\geq$ 2) of CH_3I are noticed even at this low-intensity regime. The fragmented ion yield from higher charge states of CH_3I shows a monotonic increase and saturation as a function of pulse duration, which could occur through some intermediate electronic state via enhanced ionization mechanism. The possible intermediate electronic state has been identified based on the measured kinetic energy and the angular distribution of the ionic fragments as a function of pulse duration with the support of a simple 1-D classical model of wavepacket propagation. Based on this wave-packet propagation model and the orbital energy calculation, ionization probability has been calculated as a function of pulse duration, which agrees with our observation. These results suggest an enhanced ionization occurs as a consequence of rearrangement of the energies of the molecular orbitals following bond-stretching of the C-I bond.

The dissociation dynamics of the molecular ions may get strongly coupled with many electronic processes in the presence of an intense laser field; such couplings manifest themselves in the form of structural electron correlation, photo-induced potential energy curve crossings, geometric rearrangement of the molecular orbitals, etc. Some of these photon-induced dynamic processes are observed for the first time for two different molecular systems and have been explained with a fair understanding of the underlying mechanisms. However, there is a need to investigate these further in a more systematic manner, both experimentally and theoretically.

6.2 Future Outlook

Molecules interacting with moderately intense laser field 10–100 TW/cm^2 of NIR wavelength could be populated over several electronic states just after the ionization due to the availability of several electronic states in a narrow energy window. The vibrational wavepackets created over these electronic states will eventually dissociate into several ionic fragments and these ionic fragments carry away total kinetic energy release of a similar energy range. For this reason, the unique identification of dissociation pathways of a molecular ion based on only the kinetic energy distribution is a great challenge. However, unique identification of the dissociation channels could be possible by using a controlled two-colour pump-probe technique. The wavelength of the pump pulse could be varied to populate the molecule over a specific electronic state under observation via resonance-enhanced multiphoton ionization(REMPI)(35; 113; 132). This specific electronic state could be further probed by a NIR pulse and the dissociation channel could be uniquely traced. Likewise, for O_2^+, the $1^4\Sigma_g$ state having negative dipole polarizability, could be populated by the pump pulse of a suitable wavelength through single photon ionization. The dynamics of the molecular system over this $1^4\Sigma_g$ state could be further probed by NIR pulses. Also, tailor-made pulses could be introduced as a probe pulse to control the dynamics(133).

Moreover, the time scale associated with the nuclear motion of a small diatomic molecular system lies below $\leq$25 fs, and several dynamic phenomena like structural re-arrangement, proton migration occur in this short time scale. To probe the dynamics the probe time should be much smaller than $\sim$25 fs. Using gas-filled hollow-core fiber the pulses can be compressed to few-cycle pulses of $\sim$5 fs(134; 135), which could be used to do time-resolved experiments to understand various ultrafast dynamic processes(136).

On the other hand, we have seen several low-energy fragments in both of our experiments, but they are not well resolved. Small modifications in the ion optics like adding an extra einzel lens could magnify the velocity maps up to $\sim$ 20 times, which could resolve the low energy structures efficiently(86). A well-resolved velocity map images

for these low energy fragments could help to understand the molecular origin.

REFERENCES

[1] Michele A. Brooks, T. Scott Lawrence, 1,2-Shifts of Hydrogen Atoms in Aryl Radicals, Journal of the American Chemical Society, **121**, (23), 5444–5449, (1999)

[2] P M W French, The generation of ultrashort laser pulses, Reports on Progress in Physics, **58**, 2, 169–262, (1995)

[3] Ahmed H. Zewail, Femtochemistry. Past, present, and future, Pure and Applied Chemistry, **72**, 2219, (2000)

[4] Ahmed H. Zewail, Femtochemistry: Atomic-Scale Dynamics of the Chemical Bond Using Ultrafast Lasers (Nobel Lecture), Angewandte Chemie International Edition, **39**, 2586, (2000)

[5] Max Planck, Ueber das Gesetz der Energieverteilung im Normalspectrum, Annalen der Physik, **309**, 3, 553-563, (1901)

[6] Albert Einstein, Annalen der Physik, **17**, 132, (1905)

[7] G Mainfray and G Manus, Multiphoton ionization of atoms, Reports on Progress in Physics, **54**, 10, 1333–1372, (1991)

[8] Vladimir S Popov, Tunnel and multiphoton ionization of atoms and ions in a strong laser field (Keldysh theory), Physics-Uspekhi, **47**, 9, 855–885, (2004)

[9] N B Delone and Vladimir P Krainov, Tunneling and barrier-suppression ionization of atoms and ions in a laser radiation field, Physics-Uspekhi, **41**, 5, 469–485, (1998)

[10] P. H. Bucksbaum, A. Zavriyev, H. G. Muller, and D. W. Schumacher,Softening of the H_2^+ molecular bond in intense laser fields, Phys. Rev. Lett.,**64**, 16, 1883–1886,(1990)

[11] L. J. Frasinski, J. H. Posthumus, J. Plumridge, K. Codling, P.F. Taday, and A. J. Langley, Manipulation of Bond Hardening in H_2^+ by Chirping of Intense Femtosecond Laser Pulses, Phys. Rev. Lett., **83**, 18, 3625–3628 (1999)

[12] D M P Holland and D A Shaw and S Coriani and M Stener and P Decleva, A study of the valence shell electronic states of pyridazine by photoabsorption spectroscopy and time-dependent density functional theory calculations, Journal of Physics B: Atomic, Molecular and Optical Physics, **46**, 17, 175103, (2013)

[13] Badry D.Bursulaya, and Jonggu Jeon, and Chia-Ning Yang, and Hyung J. Kim, On the Photoabsorption Spectroscopy of Water, The Journal of Physical Chemistry A, **104**, 1, 45-52, (2000)

[14] Dar'ya Davydova, Alejandro de la Cadena, Denis Akimov, and Benjamin Dietzek, Transient absorption microscopy: advances in chemical imaging of photoinduced dynamics, Laser & Photonics Reviews, **10**, 1, 62–81, (2016)

[15] Christian Bressler and Majed Chergui, Ultrafast X-ray Absorption Spectroscopy, Chemical Reviews, **104**, 4, 1781–1812, (2004)

[16] Daniel M Neumark, Time-Resolved Photoelectron Spectroscopy of Molecules and Clusters, Annual Review of Physical Chemistry, **52**, 255, (2001)

[17] Albert Stolow, Arthur E. Bragg, and Daniel M. Neumark, Femtosecond Time-Resolved Photoelectron Spectroscopy, Chemical Reviews, **104**, 1719, (2004)

[18] Cosmin I. Blaga, Junliang Xu, Anthony D. DiChiara, Emily Sistrunk, Kaikai Zhang, Pierre Agostini, Terry A. Miller, Louis F. DiMauro & C. D. Lin, Imaging ultrafast molecular dynamics with laser-induced electron diffraction, Nature, **483**, 194—197, (2012)

[19] Evangelos T. Karamatskos, Gildas Goldsztejn, Sebastian Raabe, Philipp Stammer, Terry Mullins, Andrea Trabattoni, Rasmus R. Johansen, Henrik Stapelfeldt, Sebastian Trippe, Marc J. J. Vrakking, Jochen Küpper, and Arnaud Rouzée, Atomic-resolution imaging of carbonyl sulfide by laser-induced electron diffraction, J. Chem. Phys., **150**, 244301, (2019)

[20] C. D. Lin and Junliang Xu, Imaging ultrafast dynamics of molecules with laser-induced electron diffraction, Phys. Chem. Chem. Phys., **14**, 13133-13145, (2012)

[21] Arthur G. Suits, Invited Review Article: Photofragment imaging, Review of Scientific Instruments, **89**, 111101, (2018)

[22] Imaging of Molecular Dynamics: Technology and Applications, Edited by Benjamin Whitakar (2003)

[23] André T. J. B. Eppink and David H. Parker, Velocity map imaging of ions and electrons using electrostatic lenses: Application in photoelectron and photofragment ion imaging of molecular oxygen, Review of Scientific Instruments, **68**, 3477, (1997)

[24] R Ali, V V Frohne, CL Cocke, M Stockli, S Cheng, ML Raphaelian, Q-value measurements in charge-transfer collisions of highly charged ions with atoms by recoil longitudinal momentum spectroscopy, Phys Rev Lett., **69**, 17, 2491-2494, (1992)

[25] J Ullrich and R Moshammer and A Dorn and R D rner and L Ph H Schmidt and H Schmidt-B cking, Recoil-ion and electron momentum spectroscopy: reaction-microscopes, Reports on Progress in Physics, **66**, 9, 1463–1545, (2003)

[26] R. Dörner *et. al*,Recoil Ion Momentum Spectroscopy Momentum Space Images of Atomic Reactions, New Directions in Atomic Physics, Springer US, 33–45, (1999)

[27] R. Dörner and V. Mergel and O. Jagutzki and L. Spielberger and J. Ullrich and R. Moshammer and H. Schmidt-Böcking, Cold Target Recoil Ion Momentum Spectroscopy: a 'momentum microscope' to view atomic collision dynamics, Physics Reports, **330**, 2, 95-192, (2000)

[28] P Downie and D Litchfield and R Parsons and D J Reynolds and I Powis, High-resolution position-sensing resistive anode microchannel plate detector systems suitable for megahertz count-rates, Measurement Science and Technology, **4**, 11, 1293–1296, (1993)

[29] DETECTOR MANUALS: MCP Detector with Delay-Line Anode, RoentDek Handels GmbH

[30] Zixuan Wang, Cheng Huang and Jianhui Wu, A Review of CMOS Time-to-Digital Converter, Journal of Circuits, Systems and Computers, **23**, 7, 1430001, (2014)

[31] DETECTOR MANUALS: TDC8HP, RoentDek Handels GmbH

[32] James Janesick and Gloria Putnam, Developments and Applications of High-Performance CCD and CMOS Imaging Arrays, Annual Review of Nuclear and Particle Science, **52**, 263–300, (2003)

[33] C. Martin, P. Jelinsky, M. Lampton, and R. F. Malina, Wedge-and-strip anodes for centroid-finding position-sensitive photon and particle detectors, Review of Scientific Instruments, **52**, 7, 1067, (1981)

[34] David W. Chandler and Paul L. Houston, Two-dimensional imaging of state-selected photodissociation products detected by multiphoton ionization, J. Chem. Phys., **87**, 1445, (1987)

[35] D. H. Parker and André T. J. B. Eppink, Photoelectron and photofragment velocity map imaging of state-selected molecular oxygen dissociation/ionization dynamics, J. Chem. Phys., **107**, 2357, (1997)

[36] X. M. Tong, Z. X. Zhao, and C. D. Lin, Theory of molecular tunneling ionization, Phys. Rev. A, **66**, 033402, (2002)

[37] A. M. Perelomov, V. S. Popov, M. V. Terent'ev, Ionization of Atoms in an Alternating Electric Field, Soviet Physics JETP, **23**, 924, (1966)

[38] E. P. Benis, J. F. Xia, X. M. Tong, M. Faheem, M. Zamkov, B. Shan, P. Richard, and Z. Chang, Ionization suppression of Cl_2 molecules in intense laser fields, Phys. Rev. A, **70**, 025401, (2004)

[39] D. Pavi**c**ić, A. Kiess, T. W. Hänsch, and H. Figger, Intense-Laser-Field Ionization of the Hydrogen Molecular Ions $H_2{}^+$ and $D_2{}^+$ at Critical Internuclear Distances, Phys. Rev. Lett., **94**, 16, 163002 (2005)

[40] T. Zuo and A. D. Bandrauk, Charge-resonance-enhanced ionization of diatomic molecular ions by intense lasers, Phys. Rev. A, **52**, 4, R2511–R2514 (1995)

[41] A. D. Bandrauk, and J. Ruel, Charge-resonance-enhanced ionization of molecular ions in intense laser pulses: Geometric and orientation effects, Phys. Rev. A, **59**, 3, 2153–2162(1999)

[42] S. Erattupuzha, C.L. Covington, A. Russakoff, E. Lötstedt, S. Larimian, V. Hanus, S. Bubin, M. Koch, S. Gräfe, A. Baltuska, X. Xie, K. Yamanouchi, K. Varga and M. Kitzler, Enhanced ionisation of polyatomic molecules in intense laser pulses is due to energy upshift and field coupling of multiple orbitals, J. Phys. B: At. Mol. Opt. Phys., **50**, 12, 125601 (2017)

[43] M. Born and R. Oppenheimer, Annalen der Physik, **84**, 457, (1927)

[44] P. W. Atkins and R. S. Friedman, Molecular Quantum Mechanics, Vol. 3 (Oxford University Press, 1997)

[45] B.H. Bransden and C.J. Joachain, Physics of Atoms and Molecules, second edition, (2004)

[46] Thomas Brabec and Ferenc Krausz, Intense few-cycle laser fields: Frontiers of nonlinear optics, Rev. Mod. Phys., **72**, 545, (2000)

[47] P. B. Corkum and Ferenc Krausz, Attosecond science, Nature Phys., **3**, 381, (2007)

[48] L. V. Keldysh, Ionization in the field of a strong electromagnetic wave, Soviet Physics JETP, **20**, 1307, (1965)

[49] Merrick J. DeWitt and Robert J. Levis, Calculating the keldysh adiabaticity parameter for atomic and polyatomic molecules, J. Chem. Phys., **108**, 7739, (1998)

[50] F. A. Ilkov, J. E. Decker, and S. L. Chin, Ionization of atoms in the tunnelling regime with experimental evidence using Hg atoms, J. Phys. B: At. Mol. Opt. Phys., **25**, 12, 4005 (1992)

[51] H. Friedrich, Theoretical Atomic Physics, Springer, Berlin, (1998)

[52] Kirsten Schnorr, XUV Pump-Probe Experiments on Diatomic Molecules: Tracing the Dynamics of Electron Rearrangemnt and Interatomic Coulombic Decay, Springer Thesis, (2015)

[53] M. Göppert-Mayer, Annalen der Physik, **401**, 273–294, (1931)

[54] L. D. Landau and E. M. Lifshitz, Quantum Mechanics, Pergamon Press, Oxford, (1965)

[55] M. V. Ammosov, N. B. Delone, and V. P. Krainov, Tunnel ionization of complex atoms and of atomic ions in an alternating electromagnetic field, Soviet Physics JETP, **64**, 1191, (1986)

[56] Christer Z. Bisgaard and Lars Bojer Madsen, Tunneling ionization of atoms, Am. J. Phys., **72**, 249, (2004)

[57] Xi Chu, Time-dependent density-functional-theory calculation of strong-field ionization rates of H_2, Phys. Rev. A, **82**, 023407, (2010)

[58] Song-Feng Zhao, Cheng Jin, Anh-Thu Le, T. F. Jiang, and C. D. Lin, Determination of structure parameters in strong-field tunneling ionization theory of molecules, Phys. Rev. A, **81**, 033423, (2010)

[59] X. M. Tong, Z. X. Zhao, and C. D. Lin, Molecular tunnelling ionization and rescattering induced double ionization of H_2 and D_2 molecules, J. Mod. Opt., **52**, 185, (2005)

[60] Takahiro Miyazaki, Makoto Katori, and Norio Konno, Wigner formula of rotation matrices and quantum walks, Phys. Rev. A, **76**, 012332, (2007)

[61] A. D. Bandrauk and M. L. Sink, Photodissociation in intense laser fields: Predissociation analogy, J. Chem. Phys., **74**, 1110, (1981)

[62] J. H. Shirley, Solution of the Schrödinger Equation with a Hamiltonian Periodic in Time, Phys. Rev., **138**, B979, (1965)

[63] S. I. Chu, Floquet theory and complex quasivibrational energy formalism for intense field molecular photodissociation, J. Chem. Phys., **75**, 2215, (1981)

[64] Jan Posthumus, Molecules and Clusters in Intense Laser Fields, Cambridge University Press, (2001)

[65] B. Friedrich and D. Herschbach, Phys. Rev. Lett., **74**, 23, 4623, (1995), Phys. Rev. Lett., **74**, 23, 4623, (1995)

[66] B. Friedrich and D. Herschbach, Alignment enhanced spectra of molecules in intense non-resonant laser fields, Chem. Phys. Lett., **262**, 41, (1996)

[67] C. Ellert and P. B. Corkum, Disentangling molecular alignment and enhanced ionization in intense laser fields, Phys. Rev. A, **59**, 5, R3170, (1999)

[68] S. Banerjee, D. Mathur, and G. Ravindra Kumar, Propensity of molecules to spatially align in intense light fields, Phys. Rev. A, **63**, 045401, (2001)

[69] D S Murphy, J McKenna, C R Calvert, W A Bryan, E M L English, J Wood, I C E Turcu, W R Newell, I D Williams and J F McCann, Controlling dissociation processes in the D+2 molecular ion using high-intensity, ultrashort laser pulses, J. Phys. B: At. Mol. Opt. Phys., **40**, S359–S372 (2007)

[70] Zhifeng Wu, Chengyin Wu, Xianrong Liu, Yunquan Liu, Yongkai Deng, and Qihuang Gong, Multiple ionization of oxygen studied by coincident measurement, Optics Express, **18**, 10, 10395, (2010)

[71] Domagoj Pavi**c**ić, Kevin F. Lee, D. M. Rayner, P. B. Corkum, and D. M. Villeneuve, Direct Measurement of the Angular Dependence of Ionization for N_2, O_2, and CO_2 in Intense Laser Fields, Phys. Rev. Lett., **98**, 243001, (2007)

[72] X M Tong, Z X Zhao, A S Alnaser, S Voss, C L Cocke and C D Lin, Post ionization alignment of the fragmentation of molecules in an ultrashort intense laser field, J. Phys. B: At. Mol. Opt. Phys., **38**, 333–341, (2007)

[73] Wei Lai, Alan Heins, and Chunlei Guo, Molecular alignment in degenerated dissociation channels in strong laser fields, Scientific Reports, **7**, 2584, (2017)

[74] S Voss, A S Alnaser, X-M Tong, C Maharjan, P Ranitovic, B Ulrich, B Shan, Z Chang, C D Lin and C L Cocke, High resolution kinetic energy release spectra and angular distributions from double ionization of nitrogen and oxygen by short laser pulses, J. Phys. B: At. Mol. Opt. Phys., **37**, 4239, (2004)

[75] A. Zavriyev, P. H. Bucksbaum, H. G. Muller, and D. W. Schumacher, Ionization and dissociation of H_2 in intense laser fields at 1.064 μm, 532 nm, and 355 nm, Phys. Rev. A, **42**, 5500, (1990)

[76] M. Magrakvelidze, C. M. Aikens, and U. Thumm, Dissociation dynamics of diatomic molecules in intense laser fields: A scheme for the selection of relevant adiabatic potential curves, Phys. Rev. A, **86**, 023402, (2012)

[77] S. De, M. Magrakvelidze, I. A. Bocharova, D. Ray, W. Cao, I. Znakovskaya, H. Li, Z. Wang, G. Laurent, U. Thumm, M. F. Kling, I. V. Litvinyuk, I. Ben-Itzhak, and C. L. Cocke, Following dynamic nuclear wave packets in N_2, O_2, and CO with few-cycle infrared pulses, Phys. Rev. A, **84**, 043410, (2011)

[78] S. De, I. A. Bocharova, M. Magrakvelidze, D. Ray, W. Cao, B. Bergues, U. Thumm, M. F. Kling, I. V. Litvinyuk, and C. L. Cocke, Tracking nuclear wave-packet dynamics in molecular oxygen ions with few-cycle infrared laser pulses, Phys. Rev. A, **82**, 013408, (2010)

[79] I. A. Bocharova, A. S. Alnaser, U. Thumm, T. Niederhausen, D. Ray, C. L. Cocke, and I. V. Litvinyuk, Time-resolved Coulomb-explosion imaging of nuclear wave-packet dynamics induced in diatomic molecules by intense few-cycle laser pulses, Phys. Rev. A, **83**, 013417, (2011)

[80] A. S. Alnaser, B. Ulrich, X. M. Tong, I. V. Litvinyuk, C. M. Maharjan, P. Ranitovic, T. Osipov, R. Ali, S. Ghimire, Z. Chang, C. D. Lin, and C. L. Cocke, Simultaneous real-time tracking of wave packets evolving on two different potential curves in H_2^+ and D_2^+, Phys. Rev. A, **72**, 030702(R), (2005)

[81] Reza Karimi, Éric Bisson, B. Wales, Samuel Beaulieu, Mathieu Giguère, ZiJian Long, Wing-Ki Liu, Jean-Claude Kieffer, François Légaré, and Joseph Sanderson, N2O ionization and dissociation dynamics in intense femtosecond laser radiation, probed by systematic pulse length variation from 7 to 500 fs, J. Chem. Phys., **138**, 204311, (2013)

[82] Irina Bocharova, Reza Karimi, Emmanuel F. Penka, Jean-Paul Brichta, Philippe

Lassonde, Xiquan Fu, Jean-Claude Kieffer, André D. Bandrauk, Igor Litvinyuk, Joseph Sanderson, and François Légaré, Charge Resonance Enhanced Ionization of CO_2 Probed by Laser Coulomb Explosion Imaging, Phys. Rev. Lett., **107**, 063201, (2011)

[83] C. Cornaggia, J. Lavancier, D. Normand, J. Morellec, P. Agostini, J. P. Chambaret, and A. Antonetti, Multielectron dissociative ionization of diatomic molecules in an intense femtosecond laser field, Phys. Rev. A, **44**, 4499, (1991)

[84] L J Frasinski, P A Hatherly, K Codling, M Larsson, A Persson1 and C -G Wahlstrom, J. Phys. B: At. Mol. Opt. Phys., **27**, L109, (1994)

[85] W. C. Wiley, and I. H. McClaren, Time-of-Flight Mass Spectrometer with Improved Resolution, Review of Scientific Instruments, **26**, 7, 1150, (1955)

[86] H. L. Offerhaus, C. Nicole, F. Lepine, C. Bordas, F. Rosca-Pruna, M. J. J. Vrakking, A magnifying lens for velocity map imaging of electrons and ion, Review of Scientific Instruments, **72**, 8, 3245, (2001)

[87] R. Gopal, Arnab Sen, S. R. Sahu, A. S. Venkatachalam, M. Anand, and V. Sharma, Note: An ion imaging spectrometer for studying photo-induced fragmentation in small molecules, Review of Scientific Instruments, **89**, 8, 086107, (2018)

[88] A. J. R. Heck and D. W. Chandler, Imaging Techniques for the Study of Chemical Reaction Dynamics, Annu. Rev. Phys. Chem., **46**, 335, (1995)

[89] R. G. Compton and G. Hancock, Elsevier, Amsterdam, vol-1, p-307, (1993)

[90] C. Bordas, F. Paulig, H. Helm and D. L. Huestis, Photoelectron imaging spectrometry: Principle and inversion method, Review of Scientific Instruments, **67**, 2257, (1996)

[91] J. Winterhalter, D. Maier, J. Hornerkamp, V. Schyja and H. Helm, Imaging of charged atomic reaction products: Inversion by a two-dimensional regularization method, J. Chem. Phys., **110**, 11187, (1999)

[92] A. Khan, L. C. Tribedi, and D. Misra, A recoil ion momentum spectrometer for molecular and atomic fragmentation studies, Review of Scientific Instruments, **86**, 043105, (2015)

[93] D. Townsend, M. P. Minitti, and A. G. Suits, Direct current slice imaging, Review of Scientific Instruments, **74**, 2530, (2003)

[94] Mingyuan Shi, Shaochuan Huang, Wei Xi, Zuoye Liu, Hongchuan Du, Baowei Ding and Bitao Hu, Applied Physics B, **123**, 90, (2017)

[95] A. S. Alnaser, S. Voss, X. -M. Tong, C. M. Maharjan, P. Ranitovic, B. Ulrich, T. Osipov, B. Shan, Z. Chang, and C. L. Cocke, Effects Of Molecular Structure on Ion Disintegration Patterns In Ionization of O_2 and N_2 by Short Laser Pulses, Phys. Rev. Lett., **93**, 113003, (2004)

[96] Ahmed Mohammed, ACCURATE CALCULATIONS OF NONLINEAR OPTICAL PROPERTIES USING FINITE FIELD METHODS, Ph.D Thesis, (2017)

[97] M. W. Schmidt, K. K. Baldridge, J. A. Boatz, S. T. Elbert, M. S. Gordon, J. H. Jensen, S. Koseki, N. Matsunaga, K. A. Nguyen, S. Su, T. L. Windus, M. Dupuis and J. A. Montgomery, General atomic and molecular electronic structure system, Journal of Computational Chemistry, **14**, 1347-1363, (1993)

[98] P. G. Szalay, T. Müller, G. Gidofalvi, H. Lischka, and R. Shepard, Multiconfiguration Self-ConsistentField and Multireference Configuration Interaction Methods and Applications, Chem. Rev., **112**, 1, 108-181, (2012)

[99] F. Gilmore, Potential energy curves for N_2, NO, O_2 and corresponding ions, Journal of Quantitative Spectroscopy and Radiative Transfer, **5**, 2, 369-389, (1965)

[100] M.A. Buldakov and V.N. Cherepanovb, Polarizability functions of diatomic homonuclear molecules: Semiempirical approach, Journal of Computational Methods in Sciences and Engineering, **4**, 237-250, (2004)

[101] C. M. Marian, R. Marian, S. D. Peyerimhoff, B. A. Hess, R. J. Buenker, and G. Seger,Ab initio CI calculation of O2 + predissociation phenomena induced by a spin-orbit coupling mechanism, Molecular Physics, **46**, 4, 779-810, (1982)

[102] P. von den Hoff, I. Znakovskaya, S. Zherebtsov, M. F. Kling, and R. de VivieRiedle, Effects of multi orbital contributions in the angular-dependent ionization of molecules in intense few-cycle laser pulses, , Appl. Phys. B, **98**, 659, (2010)

[103] S. Petretti, Y. V. Vanne, A. Saenz, A. Castro, and P. Decleva, Alignment-Dependent Ionization of N_2, O_2 and CO_2 in Intense Laser Fields, Phys. Rev. Lett., **104**, 223001, (2010)

[104] S. Petretti, A. Magaña, A. Saenz, and P. Decleva, Wavelength- and alignment-dependent photoionization of N_2 and O_2, Phys. Rev. A, **94**, 053411, (2016)

[105] V. P. Majety and A. Scrinzi, Dynamic Exchange in the Strong Field Ionization of Molecules, Phys. Rev. Lett., **115**, 103002, (2015)

[106] L. J. Frasinski, J. Plumridge, J. H. Posthumus, K. Codling, P. F. Taday, E. J. Divall and A. J. Langley, Counterintuitive Alignment of H_2^+ in Intense Femtosecond Laser Fields, Phys. Rev. Lett., **86**, 2541, (2001)

[107] Arnab Sen, T. Sairam, S. R. Sahu, B. Bapat, R. Gopal, and V.Sharma, Hindered alignment in ultrashort, intense laser-induced fragmentation of O_2, J. Chem. Phys., **152**, 014302, (2020)

[108] X. Sun, R. L. Fu, K. Yonemitsu and K. Nasu, Photoinduced Polarization Inversion in a Polymeric Molecule, Phys. Rev. Lett., **84**, 2830, (2000)

[109] M. E. Corrales, G. Gitzinger, J. González-Vázquez, V. Loriot, R. de Nalda, and L. Bañares, Velocity map imaging and theoretical study of the coulomb explosion of CH_3I under intense femtosecond IR pulses, J. Chem. Phys., **116**, 2669, (2012)

[110] D. Zhang, S. Luo, H. Xu M. Jin, F. Liu, B. Yan, Z. Wang, H. Liu, D. Jiang, A. Eppink, W. Roeterdink, S. Stolte, and D. Ding, Dissociative ionization and Coulomb explosion of CH_3I in intense femtosecond laser fields, Eur. Phys. J. D **71**, 148, (2017)

[111] H. Liu, Z. Yang, Z. Gao, and Z. Tang, Ionization and dissociation of CH3I in intense laser field, J. Chem. Phys., **126**, 044316, (2007)

[112] Y. Wang, S. Zhang, Z. Wei, and B. Zhang, Velocity map imaging of dissociative ionization and coulomb explosion of CH_3I induced by a femtosecond laser, J. Phys. Chem. A, **112**, 3846, (2008)

[113] S. Marggi Poullain, D. V. Chicharro, J. González-Vázquez, L. Rubio-Lago, and L. Bañares, A velocity map imaging study of the photodissociation of the methyl iodide cation, Phys. Chem. Chem. Phys. **19**, 7886 (2017).

[114] Z. Wei, J. Li, S. T. See, and Z.-H. Loh, Spin–orbit state-selective C-I dissociation dynamics of the CH_3I^+X electronic state induced by intense few-cycle laser fields, J. Phys. Chem. Lett., **8**, 6067 (2017)

[115] Y. Malakar, W. L. Pearson, M. Zohrabi, B. Kaderiya, P. Kanaka, Raju F. Ziaee, S. Xue, A. T. Le, I. Ben-Itzhak, D. Rolles, and A. Rudenko, Time-resolved imaging of bound and dissociating nuclear wave packets in strong-field ionized iodomethane, Phys. Chem. Chem. Phys., **21**, 14090, (2019)

[116] M. E. Corrales, J. González-Vázquez, R. de Nalda, and L. Bañares, Coulomb explosion imaging for the visualization of a conical intersection, J. Phys. Chem. Lett., **10**, 138, (2019)

[117] A. H. Alexander, G. Basnayake, D. A. Debrah, Y. F. Lin, S. K. Lee, P. Hoerner, Q. Liao, H. Schlegel, and W. Li, Disentangling strong-field multielectron dynamics with angular streaking, J. Phys. Chem. Lett, **9**, 2539 (2018)

[118] S. G. Walt, N. Bhargava Ram, A. von Conta, O. I. Tolstikhin, L. B. Madsen, F. Jensen, and H. J. Wörner, Role of multielectron effects in the asymmetry of strong-field ionization and fragmentation of polar molecules: The methyl halide series, J. Phys. Chem. A, **119**, 11772, (2015)

[119] S. Das, P. Sharma, and R. K. Vatsa, Tracing photoionisation behavior of methyl iodide in gas phase: From isolated molecule to molecular aggregate, J. Photochem. Photobiol. C **33**, 27 (2017)

[120] K. Harumiya, H. Kono, Y. Fujimura, I. Kawata, and A. D. Bandrauk, Intense

laser-field ionization of H2 enhanced by twoelectron dynamics, Phys. Rev. A, **66**, 043403 (2002)

[121] S. Chattopadhyay and L. B. Madsen, Electron correlation effects in enhanced ionization of diatomic molecules in nearinfrared fields, Phys. Rev. A, **99**, 023424, (2019)

[122] B. Alonso, Í. J. Sola, and H. Crespo, Self-calibrating d-scan: Measuring ultrashort laser pulses on-target using an arbitrary pulse compressor, Scientific Reports, **8**, 3264 (2018)

[123] A Rudenko, K. Zrost, C. D. Schröter, V. L. B. de Jesus, B. Feuerstein, R. Moshammer, and J. Ullrich, Resonant structures in the low-energy electron continuum for single ionization of atoms in the tunneling regime, J. Phys. B: At. Mol. Opt. Phys., **37**, L407 (2004)

[124] M. Tadjeddine, J. P. Flament, and C. Teichteil, Spin-orbit calculations of the molecular states of CH_3I^+, related to photofragmentation experiments, Chem. Phys., **124**, 13, (1988)

[125] G. L. Kamta and A. D. Bandrauk, Nonsymmetric molecules driven by intense few-cycle laser pulses: Phase and orientation dependence of enhanced ionization, Phys. Rev. A, **76**, 053409, (2007)

[126] P. Graham, K. W. D. Ledingham, R. P. Singhai, M. Hankin, T. McCanny, X. Fang, C. Kosmidis, P. Tzallas, P. F. Taday, and A. J. Langley, On the fragment ion angular distributions arising from the tetrahedral molecule CH_3I, J. Phys. B: At. Mol. Opt. Phys., **34**, 4015, (2001)

[127] A. T. J. B. Eppink and D. H. Parker, Energy partitioning following photodissociation of methyl iodide in the A band: A velocity mapping study, J. Chem. Phys, **110**, 832 (1999)

[128] B. Jochim, R. Siemering, M. Zohrabi, O. Voznyuk, J. B. Mahowald, D. G. Schmitz, K. J. Betsch, Ben Berry, T. Severt, N. G. Kling, T. G. Burwitz, K. D.

Carnes, M. F. Kling, I. BenItzhak, E. Wells, and R. de Vivie-Riedle, The importance of Rydberg orbitals in dissociative ionization of small hydrocarbon molecules in intense laser fields, Scientific Reports, **7**, 4441, (2017)

[129] J. Cao, C. J. Bardeen, and K. R. Wilson, Molecular π pulses: Population inversion with positively chirped short pulses, J. Chem. Phys., **113**, 1898, (2000)

[130] J. Plenge, A. Wirsing, C. Raschpichler, M. Meyer, and E. Rühl, Chirped pulse multiphoton ionization of nitrogen: Control of selective rotational excitation in N_2^+ ($B^2\ \Sigma_u^+$), J. Chem. Phys. **130**, 244313, (2009)

[131] Arnab Sen, S. Mandal, Sanket Sen, Bhas Bapat, R. Gopal, and V. Sharma, Dissociation dynamics of multiply charged CH_3I in moderately intense laser fields, Phys. Rev. A, **103**, 043107, (2021)

[132] Y. Malakar, F. Wilhelm, D. Trabert, Kanaka Raju P., X. Li, W. L. Pearson, W. Cao, B. Kaderiya, I. Ben-Itzhak, and A. Rudenko, State-selective dissociation dynamics of an oxygen molecular ion studied with single-harmonic pump and infrared-probe pulses, Phys. Rev. A, **98**, 013418, (2018)

[133] Qiu-Nan Tong, De-Hou Fei, Zhen-Zhong Lian, Hong-Xia Qi, Sheng-Peng Zhou, Si-Zuo Luo, Zhou Chen and Zhan Hu, Coherent control of fragmentation of methyl iodide by shaped femtosecond pulse train, Chinese Physics B, **28**, 9, 093201, (2019)

[134] M. Nisoli, S. Stagira, S. De Silvestri, O. Svelto, S. Sartania, Z. Cheng, M. Lenzner, Ch. Spielmann, F. Krausz, A novel-high energy pulse compression system: generation of multigigawatt sub-5-fs pulses, Appl. Phys. B, **65**, 189-196, (1997)

[135] E. Conejero Jarque, J. San Roman, F. Silva, R. Romero, W. Holgado, M. A. Gonzalez-Galicia, B. Alonso, I. J. Sola and H. Crespo, Universal route to optimal few- to single-cycle pulse generation in hollow-core fiber compressors, Scientific Reports, **8**, 2256, (2018)

[136] Yasuo Nabekawa, Yusuke Furukawa, Tomoya Okino, A Amani Eilanlou, Eiji J. Takahashi, Kaoru Yamanouchi and Katsumi Midorikawa, Sub-10-fs control of

dissociation pathways in the hydrogen molecular ion with a few-pulse attosecond pulse train, Nature Communications, **7**, 12835, (2016)

LIST OF PUBLICATIONS

Publications Related to The Thesis

I. **Note: An ion imaging spectrometer for studying photo-induced fragmentation in small molecules**
R. Gopal, **Arnab Sen**, S. R. Sahu, A. S. Venkatachalam, M. Anand, and V. Sharma
Review of Scientific Instruments, Vol. 89, 8, 086107 (2018)

II. **Hindered alignment in ultrashort, intense laser-induced fragmentation of O_2**
Arnab Sen, T. Sairam, S. R. Sahu, B. Bapat, R. Gopal, and V. Sharma
Journal of Chemical Physics, Vol. 152, 1, 014302 (2020)

III. **Dissociation dynamics of multiply charged CH_3I in moderately intense laser fields**
Arnab Sen, S. Mandal, S. Sen, B. Bapat, R. Gopal, and V. Sharma
Physical Review A, Vol. 103, 4, 043107 (2021)

Other Publications

I. **Fragmentation dynamics of CO_2^{4+}: Contributions of different electronic states**
Sumit Srivastav, **Arnab Sen**, Deepak Sharma and B. Bapat
Physical Review A, Vol. 103, 3, 032821 (2021)

II. **Coincident angle-resolved state-selective EUV photoelectron spectroscopy of acetylene molecules: a candidate system for time-resolved dynamics**
S. Mandal, R. Gopal, S. Hemkumar, Alessandro D'Elia, **Arnab Sen**, S. Sen, R. Richter, M. Coreno, B. Bapat, M. Mudrich, V. Sharma, S. Krishnan
Faraday Discussions, Vol. 228, 242-265, (2021)

III. **Three-body break-up of doubly charged camphor molecule post C 1s ionisation**
S. Sen, S. Mandal, **Arnab Sen**, R. Gopal, Ltaief. Ben Ltaief, S. Turchini, D. Catone, N. Zema, R. Richter, M. Mudrich, S. Krishnan, and V. Sharma
Under Preperation

Presentations in Conferences

1. Poster presentation titled *Study Molecular Dissociation Dynamics using Velocity Map Imaging* at the **7th Topical Conference of the Indian Society of Atomic and Molecular Physics**, IISER-Tirupati and IIT-Tirupati, 6th January 2018 - 8th January 2018

2. Poster presentation titled *Post-Ionization Alignment Effect In Molecular Oxygen Ion* at the **13th Asian International Seminar on Atomic and Molecular Physics**, TIFR and IIT-Bombay, 3rd December 2018 - 8th December 2018

3. Oral presentation titled *Transient Negative Polarizability Freezes Rotational Motion In Ultrashort Laser Induced Fragmentation of Molecules* at the **22nd National Conference on Atomic and Molecular Physics**, IIT-Kanpur, 25th March 2019 - 28th March 2019

4. Poster presentation titled *The Dependence Of The Dissociation Dynamics of The CH_3I On The Pulse-width Of The Intense Femtosecond Laser Field* at the **Topical conference on Atomic and Molecular Collisions for Plasma Applications**, IIT-Roorkee, 3rd March 2020 - 5th March 2020